Integrated Quantum Photonics
from modular to monolithic integration

Esmaeil Zadeh, Iman

DOI
10.4233/uuid:5609f331-6473-447e-b271-bdb76823960f

Publication date
2016

Document Version
Final published version

Citation (APA)
Esmaeil Zadeh, I. (2016). *Integrated Quantum Photonics: from modular to monolithic integration*. [Dissertation (TU Delft), Delft University of Technology]. https://doi.org/10.4233/uuid:5609f331-6473-447e-b271-bdb76823960f

Important note
To cite this publication, please use the final published version (if applicable).
Please check the document version above.

Integrated Quantum Photonics

from modular to monolithic integration

Proefschrift

ter verkrijging van de graad van doctor
aan de Technische Universtiteit Delft,
op gezag van de Rector Magnificus Prof. ir. K.C.A.M. Luyben,
voorzitter van het College voor Promoties,
in het openbaar te verdedigen op vrijdag 30 september 2016 om 10:00 uur

door

Iman Esmaeil Zadeh

Master of Science in Electrical Engineering, Linköping University
geboren te Neyshaboor, Iran

Dit proefschrift is goedgekeurd door de

promotor: Prof. dr. ir. H. van der Zant,
promotor: Prof. dr. MSc. V. Zwiller, KTH Stockholm, Zweden

Samenstelling promotiecommissie:

Rector Magnificus,	Voorzitter
Prof. dr. ir. H. van der Zant,	Technische Universiteit Delft, promotor
Prof. dr. MSc. V. Zwiller,	KTH Stockholm, Zweden

Onafhankelijke leden:

Prof. Dr. J. J. Finley	Technische Universität München
Prof. Dr. A. Fiore	Technische Universiteit Eindhoven
Prof. Dr. L.D.A. Siebbeles	Technische Universiteit Delft
Dr. J-R. Gao	Technische Universiteit Delft
Prof. Dr. Y. M. Blanter	Technische Universiteit Delft, reservelid

ISBN 978-90-8593-271-0

Casimir PhD series, Delft-Leiden 2016-27

Cover design: A. Elshaari and A. Dumon

Printed by: Gildeprint Drukkerijen

An electronic version of this thesis is available at http://repository.tudelft.nl/.

Contents

Chapter 1

Introduction

Soon after quantum mechanics became globally accepted, an intense effort to exploit its peculiar effects started. Initially, the works were focused on explaining the behavior of materials and designing semiconductors for microelectronic technology but it did not take long until scientists realized quantum mechanics can have many other useful applications. Many researchers from different disciplines are actively involved in developing the quantum technologies with applications including but not limited to: quantum computation [1,2], quantum cryptography [3,4], quantum simulation [5,6], quantum sensors [7,8], and quantum imaging [9].

Many different technologies to implement these applications have been introduced, each with its own advantages and limitations. Since the beginning of this scientific race, quantum optics has been one of the front runners. With the introduction of linear optical quantum information processing (LOQIP) [10] more than a decade ago, numerous research teams have been involved in its realization and development. Thanks to advances in telecommunication, photonic circuits are already well developed, CMOS compatible, and they work well both at room and cryogenic temperatures. There have been constant improvements in the quality of single photon sources and single photon detectors every year.

Despite significant improvements in the quality of quantum optical components, the implementations of LOQIP and other quantum technologies have been limited and scalable photonic platforms are still to be realized. Quantum optical systems have often demanding requirements which become more stringent as the complexity of the application grows. In this thesis we propose new techniques and prototype novel devices to address the scalability of quantum photonic circuits.

1.1 Photonic devices for quantum technology

Photonic devices have been used in quantum information processing [11,12], quantum sensing [13,14], quantum communication [15–17], quantum imaging [18]. Most demonstrations so far have been realized with discrete devices. To establish a practical platform for the interesting applications of quantum mechanics, a scalable implementation is needed. At higher level two methodologies for scalable implementation of photonic based quantum information processing exist: modular approach and monolithic integration. In the modular approach, elements of the experiments are built and tested separately and are then connected by free space optics or optical fibers. In monolithic integration all components are integrated in one or few semiconductor chips and communications between different elements are performed through on-chip optical channels and possibly limited intra-chip optical links. In this thesis we study and demonstrate working prototypes of both schemes.

1.2 Modular implementation versus monolithic integration

Modular quantum optics is the method of choice in most labs, it provides easier debugging i.e. erroneous components can be fixed or replaced without affecting other parts of the system. Absence of cross talk and interference between different components is another advantage. The main limitations of this scheme is losses at each interconnect and bulkiness. Nevertheless, modular implementation is still very popular among scientists. This is mainly because in majority of the current research labs the size, cost, and efficiency are not the main concerns yet.

High efficiency and miniaturization are the main promises of monolithic integration. The coupling losses can be improved drastically by having sources, optical circuits, and the detectors on the same chip. The main challenges are the compatibility and complexity issues. Different technologies are used in quantum optics experiments which are difficult to integrate together. For example: it is common to use III-V quantum dots as single photon emitters, however, growing superconducting films for realizing single photon detectors on theses substrates is challenging [19].

A compatible platform for integration of single photon sources, photonic circuits, and single photon detectors is proposed and prototypes are demonstrated. In addition, fiber coupled devices for modular implementation with enhanced efficiency are presented.

1.3 Thesis overview

Chapter 2 of this thesis provides theoretical understandings and backgrounds about single photon sources, photonic circuits, and single photon detectors. More emphasis is given to sources, photonic circuits, and detectors which are suitable for integration.

Chapter 3 describes briefly the experimental aspects of this work with more focus on nanofabrication.

To establish a platform for on-chip quantum optics, sources have to be processed, integrated, and tuned. In addition, as optical excitation of multiple sources can quickly get challenging, electrically driven sources are highly desired for scaling up integrated sources. **Chapter 4** and **Chapter 5** present our preliminary results on improving the quality of electrically driven sources and on-chip energy tunning of nanowire quantum dots, respectively.

Implementing optical links and circuits requires a platform with low optical losses, high stability and compatibility with sources and detectors. **Chapter 6** presents our experimental results on stability and tuneability of SiN optical circuits as a platform for on-chip quantum optics. **Chapter 7** provides our results in integration of nanowire quantum dots with SiN optical links.

Chapter 8 presents our fiber-coupled approach for modular implementation of quantum optics experiments. We show coupling of a single photon source to a simple fiber-based photonic circuits and a fiber-coupled single photon detectors.

Bibliography

[1] Michael A. Nielsen, Freelance Writer, and Isaac L. Chuang. *Quantum Computation and Quantum Information.* Cambridge University Press, 2011.

[2] N. David. Mermin. *Quantum Computer Science, An Introduction.* Cambridge University Press, 2007.

[3] Nicolas. Gisin, Grégoire. Ribordy, Wolfgang. Tittel, and Hugo. Zbinden. Quantum cryptography. *Rev. Mod. Phys.*, 74:145–195, 2002.

[4] Valerio. Scarani, Helle. Bechmann-Pasquinucci, Nicolas. J. Cerf, Miloslav. Dušek, Norbert. Lütkenhaus, and Momtchil. Peev. The security of practical quantum key distribution. *Rev. Mod. Phys.*, 81:1301–1350, 2009.

[5] Richard P. Feynman. Simulating physics with computers. *International Journal of Theoretical Physics*, 21(6):467–488, 1982.

[6] I. M. Georgescu, S. Ashhab, and Franco. Nori. Quantum simulation. *Rev. Mod. Phys.*, 86:153–185, 2014.

[7] J. J . Bollinger, Wayne. M. Itano, D. J. Wineland, and D. J. Heinzen. Optimal frequency measurements with maximally correlated states. *Phys. Rev. A*, 54:R4649–R4652, 1996.

[8] M. Auzinsh, D. Budker, D. F. Kimball, S. M. Rochester, J. E. Stalnaker, A. O. Sushkov, and V. V. Yashchuk. Can a quantum nondemolition measurement improve the sensitivity of an atomic magnetometer? *Phys. Rev. Lett.*, 93:173002, 2004.

[9] L. A. Lugiato, A. Gatti, and E. Brambilla. Quantum imaging. *Journal of Optics B: Quantum and Semiclassical Optics*, 4(3):S176, 2002.

[10] E. Knill, R. Laflamme, and G. J. Milburn. A scheme for efficient quantum computation with linear optics. *Nature*, 409:46–52, 2001.

[11] J. L. O'Brien, G. J. Pryde, A. G. White, T. C. Ralph, and D. Branning. Demonstration of an all-optical quantum controlled-not gate. *Nature*, 426(5):264–267, 2003.

[12] Jacques. Carolan, Christopher. Harrold, Chris. Sparrow, Enrique. Martín-López, Nicholas. J. Russell, Joshua W. Silverstone, Peter J. Shadbolt, Nobuyuki. Matsuda, Manabu. Oguma, Mikitaka. Itoh, Graham D. Marshall, Mark G. Thompson, Jonathan C. F. Matthews, Toshikazu. Hashimoto, Jeremy L. O'Brien, and Anthony. Laing. Universal linear optics. *Science*, 349:711–716, 2015.

[13] Boris. M. Chernobrod and Gennady. P. Berman. Spin microscope based on optically detected magnetic resonance. *Journal of Applied Physics*, 97(1), 2005.

[14] J. M. Taylor, P. Cappellaro, L. Childress, L. Jiang, D. Budker, P. R. Hemmer, A. Yacoby, R. Walsworth, and M. D. Lukin. High-sensitivity diamond magnetometer with nanoscale resolution. *Nat. Phys.*, 4(10):810–816, 2008.

[15] L.-M. Duan, M. D. Lukin, J. I. Cirac, and P. Zoller. Long-distance quantum communication with atomic ensembles and linear optics. *Nature*, 414(6862):413–418, 2001.

[16] Zhen-Sheng. Yuan, Xiao-Hui. Bao, Chao-Yang. Lu, Jun. Zhang, Cheng-Zhi. Peng, and Jian-Wei. Pan. Entangled photons and quantum communication. *Physics Reports*, 497(1):1–40, 2010.

[17] Giuseppe. Vallone, Davide. Bacco, Daniele. Dequal, Simone. Gaiarin, Vincenza. Luceri, Giuseppe. Bianco, and Paolo. Villoresi. Experimental satellite quantum communications. *Phys. Rev. Lett.*, 115:040502, 2015.

[18] Gabriela Barreto. Lemos, Victoria. Borish, Garrett. D. Cole, Sven. Ramelow, Radek. Lapkiewicz, and Anton. Zeilinger. Quantum imaging with undetected photons. *Nature*, 512(7515):409–412, 2014.

[19] G. Reithmaier, J. Senf, S. Lichtmannecker, T. Reichert, F. Flassig, A. Voss, R. Gross, and J. J. Finley. Optimisation of nbn thin films on gaas substrates for in-situ single photon detection in structured photonic devices. *J. Appl. Phys.*, 113:143507, 2013.

Chapter 2

Background and Theory

As discussed in Chapter. 1, for integrated quantum optics three major elements are needed: single photon sources, single photon detectors, and integrated photonic circuits. In this chapter, all these components will be discussed and theoretical backgrounds are provided.

We first start by studying single-photon sources with emphasis on the quantum dots. We then provide an overview on the theory of waveguides and ring resonators as important components of integrated photonic circuits. Finally, superconducting nanowire single-photon detectors are studied as the main technology for on-chip single photon detection.

2.1 Single photon generation

To implement quantum photonic algorithms, single photons are required. Single photons can be generated using different technologies such as parametric down conversion[1], quantum dots (QD)[2,3], color centers[4], single atoms and ions[5,6] and single molecules[7,8]. Here we discuss two commonly used techniques which have also been developed for on-chip implementations; namely parametric down conversion and QDs.

A pump laser with controlled phase and intensity can be injected into a non-linear crystal to split photons into pairs as shown in Fig. 2.1. These pairs follow the energy and momentum conservation laws i.e. the combined energies and momenta is equal to the energy and momentum of the original photon and crystal lattice. The generated pairs can be used separately in single-photon experiments and also, as the photons in each pair (when prepared correctly) are phase matched and have correlated polarizations, the pair can be used in experiments requiring entangled photons. If the polarizations of the two photons are identical, the correlation is called type I and in case they anti-correlate it is referred as

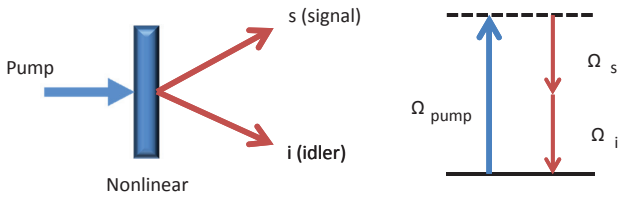

Figure 2.1 | Spontaneous Parametric Down Conversion, a non-linear crystal is pumped with a laser, generating two photon (signal and idler). Energy and momentum are conserved. Under right conditions, the signal and idler can be entangled.

type II.

Another commonly used class of emitters are quantum dots. Quantum dots can be a small section of a material embedded in a different substrate or they can be made from the same material but with different crystallography[9]. If the size of quantum dot is sufficiently smaller than Bohr radius, carriers are confined. In this case, the carrier confinement can be approximated with a particle in a box:

$$E_{confinement} = \frac{\hbar^2\pi^2}{2R^2}\left(\frac{1}{m_e^*} + \frac{1}{m_h^*}\right) \tag{2.1}$$

where $E_{confinement}$ is the total confinement energy for both electrons and holes, $\hbar$ is the reduced Plank constant, R is the radius of the quantum dot and finally, m_e^* and m_h^* are the effective masses of electrons and holes respectively[10]. Due to small size of QDs, coulomb interactions cannot be neglected. Taking into account this force, the energy levels of QD can be written in the form of:

$$E_g^{QD} = E_g^{bulk} + \frac{\hbar^2\pi^2}{2R^2}\left(\frac{1}{m_e^*} + \frac{1}{m_h^*}\right) - \frac{e^2}{4\pi\epsilon R^2} \tag{2.2}$$

in Eq. 2.2 , E_g^{QD} is the energy difference between the lowest level in conduction band and highest occupied band (valence band) in the QD, E_g^{bulk} is the same energy difference but for the bulk material, e is the electron charge and ϵ is the material dielectric constant. Fig. 2.2(a) represents the energy levels in a QD: as shown in the figure, higher levels can also exist. In analogy with atomic spectroscopy the levels are named s,p,d etc. In III-V semiconductors (relevant to this thesis) electrons are in s-like conduction band with zero angular momentum and holes exist in p-like valance band with angular momentum of $\hbar$. So including the spin, electrons have total angular momentum $J = L + S = \frac{1}{2}\hbar$ and for holes in valance band this

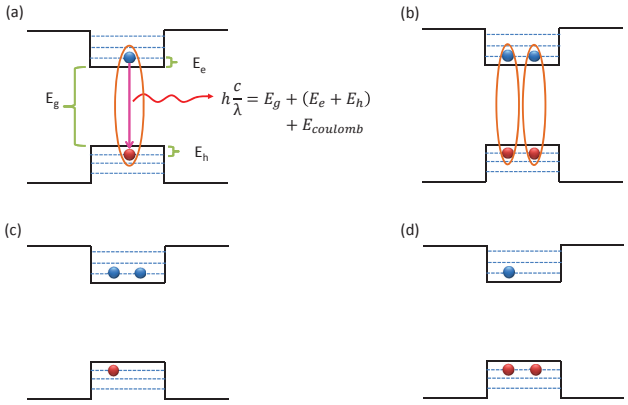

Figure 2.2 | Energy levels in quantum dots, more than a pair of electron-hole can be trapped., (a) Energy levels in exciton (X) (b) biexciton (XX) (c) negatively charged exciton (X-), and (d) positively charged exciton (X+)

is $J = \frac{3}{2}\hbar$. We neglect the split-off bands[10], so the holes fall in two categories depending on the projection of the momentum along z: $J_z = \pm\frac{3}{2}\hbar$ (heavy holes) and $J_z = \pm\frac{1}{2}\hbar$ (light holes). In normal conditions for the QDs used in this thesis, the ground state for holes is that of a heavy hole.

More than one pair of electron-hole can exist in a QD. If two excitons coexist, the so called biexciton is formed, Fig. 2.2(b). An extra electron or hole can be trapped in a QD, together with an exciton resulting in negatively charged (Fig. 2.2(c) or positively charged (Fig. 2.2(d) excitons.

QDs can be grown in different shapes and with different techniques. All QDs relevant to this thesis are either self-assembled quantum dots grown by molecular beam epitaxy or QDs embedded in nanowires grown by metal-organic chemical vapor deposition[11,12].

Since III-V QDs have high refractive index contrast with air (2-2.5 about the emission wavelength of normal QDs), it is challenging to extract single photons with high efficiency. In normal self-assembled QDs most of the emitted photons are reflected back towards the high index substrate at the semiconductor air interface. To enhance the extraction efficiency, QDs have been grown in planar cavities and etched into miro-pillars[3,13]. Integration of the emitters in cavities can also enhance the emission rate through Purcell effect[14].

Extraction efficiency can alternatively be enhanced by embedding QDs in bottom-up grown nanowires with optimized geometry[15]. Fig. 2.3 compares emission intensity profile (the electric field intensity) for a self-assembled QD with that of a nanowire QD. It is clear that nanowire improves the photon extraction efficiency significantly.

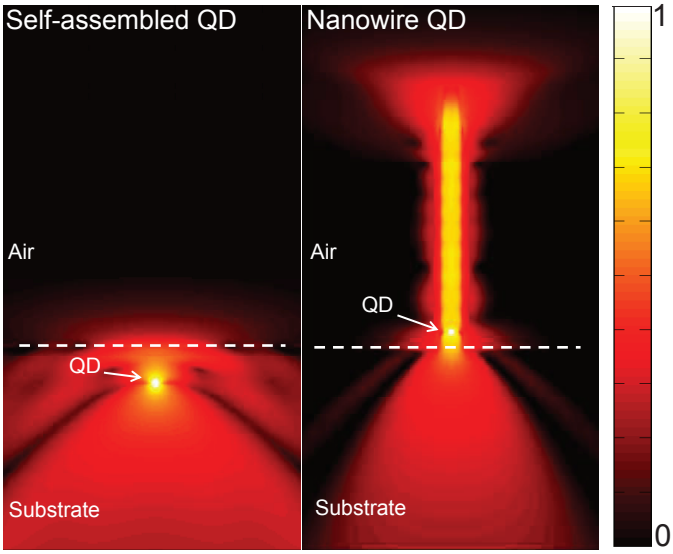

Figure 2.3 | Comparison between the electric field emission profile of a self-assembled QD and a nanowire QD, photon extraction efficiency is much higher for the nanowire QD.

2.2 On-chip photonic circuits

Scalable on-Chip photonic circuits are indispensable elements in all integrated quantum optical devices. They typically involve dielectric waveguides, Mach-Zehnders (phase shifter),beam splitters, couplers and filters. Here we briefly study waveguides and ring resonators which can be used, among other applications, as optical links and filters respectively.

2.2.1 Dielectric waveguides

Dielectric waveguides are structures which can guide electromagnetic waves from UV to mid-infrared wavelengths. In these devices light is typically trapped in a material with higher index of refraction than its surrounding (there are exceptions like slot waveguides but they are outside of the scope of this study). The waveguide can trap light in one or two axis, these are shown in Fig. 2.4(a) and b respectively. In both cases a material with refractive index of n_2 is sandwiched between two materials with lower refractive indices of n_1 and n_3. The propagation direction is z and light is assumed to be confined in the x direction for the case of Fig. 2.4(a) and in both x and y directions for the case of Fig. 2.4(b).

The electromagnetic waves in waveguides travel in distinct modes. The modes are defined

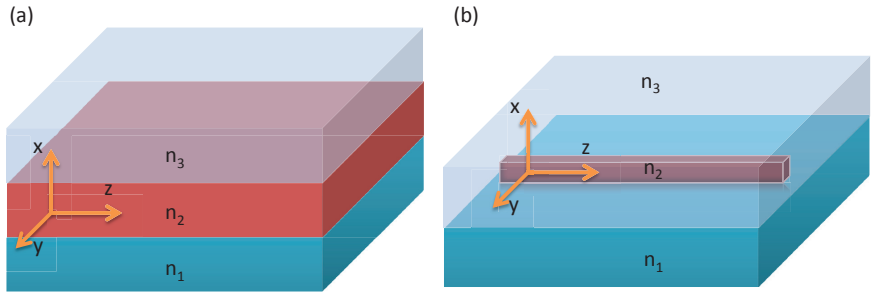

Figure 2.4 |Dielectric waveguide (a) Planar waveguide, light is confined in x direction (b) Rectangular waveguide, light is confined in both x and y directions.

as spatial distribution of optical energy which doesn't change over time. Here we follow [16] in solving for waveguide modes. We begin with the structure shown in Fig. 2.4(a) and derive the relations and then give the equations for the case of Fig. 2.4(b) without proof. To start, we assume all layers are infinite in y and z directions and semi-infinite in x direction.

An optical mode is a solution to Maxwell's wave equation:

$$\nabla^2 E(r,t) = \left[\frac{n^2(r)}{c^2}\right] \frac{\partial^2 E(r,t)}{\partial t^2} \tag{2.3}$$

Where $E(r,t)$ is the electric field of position r and time t, $n(r)$ is the refractive index of the material at position r, and c is the speed of light in vacuum. For the case of a monochromatic wave the solution has the form of:

$$E(r,t) = E(r)e^{i\omega t} \tag{2.4}$$

here ω is the angular frequency.

By substituting Eq. 2.4 in Eq. 2.3 and by assuming a plane wave propagation in z direction (so $E(r) = E(x,y)e^{(-i\beta z)}$, β is called propagation constant), we obtain:

$$\frac{\partial^2 E(x,y)}{\partial x^2} + \frac{\partial^2 E(x,y)}{\partial y^2} + [k^2 n^2(r) - \beta^2]E(x,y) = 0 \tag{2.5}$$

where $k = \frac{\omega}{c}$. Now the space can be divided in three regions (for the three layers with different refractive indexes):

$$
\begin{aligned}
R1 \quad & \frac{\partial^2 E(x,y)}{\partial x^2} + \frac{\partial^2 E(x,y)}{\partial y^2} + [k^2 n_1^2 - \beta^2] E(x,y) = 0, \\
R2 \quad & \frac{\partial^2 E(x,y)}{\partial x^2} + \frac{\partial^2 E(x,y)}{\partial y^2} + [k^2 n_2^2 - \beta^2] E(x,y) = 0, \\
R3 \quad & \frac{\partial^2 E(x,y)}{\partial x^2} + \frac{\partial^2 E(x,y)}{\partial y^2} + [k^2 n_3^2 - \beta^2] E(x,y) = 0
\end{aligned}
\tag{2.6}
$$

Depending on the sign of the term $(k^2 n_i^2 - \beta^2, i = 1, 2, 3)$ the solutions to each of Eq. 2.6 are either sinusoidal or exponential functions of x. By the boundary conditions, i.e. $E(x, y)$ and $\frac{\partial E(x,y)}{\partial x}$ have to be continuous at the interfaces between layers, not all solutions are allowed. Those solutions include non-physical waves which have non-zero distribution in infinite space. Moreover, there are modes which are mathematically and physically accepted but are not interesting in practice. These are the modes which can occur for example when substrate (n_1) has higher refractive index than the guiding layer (n_2). These modes quickly leak into the substrate and are lost, they are called leaky modes. This can be the case even when the substrate has lower refractive index in structures like Fig. 2.4(b), this time because of finite waveguide dimension in y direction.

Each of the equality in Eq. 2.6 can be solved for Transversed Electric modes (TE) and Transversed Magnetic modes (TM) by reducing the equation for E_y and E_x respectively. In the case of TE modes, E_x and E_z are zero (this would be E_y and E_z for TM modes). Here we do not solve these equations formally and refer to [16] for more detailed solutions and instead briefly study another qualitative approach for understanding of the guiding in dielectric waveguides.

The description of wave propagation mentioned before is called the physical optics approach. The so-called ray-optic approach is an alternative way with less comprehensive description. In this method, propagating light in the z-direction is transmitted in a zig-zag manner undergoing total internal reflection at boundaries of the waveguide. The plane waves in each mode are considered to travel with the same phase velocity but having different angles of reflection leading to different z component of the phase velocity. This is shown in Fig. 2.5(a) where two modes, say the TE_0 and TE_1, are drawn. The x-y plane is the constant phase plane. The rays are propagated in the waveguide layer with refractive index $n_2 > n_3 > n_1$.

The electric and magnetic fields of the plane waves can be added vectorially giving the **E** and **H** distribution of modes involving all the plane waves. The connection between the ray optics method and the physical optic approach for example for the TE mode in the region 2 can be seen by considering a solution to Eq. 2.6 with the form:

$$E_y(x, z) \propto sin(hx + \gamma) \tag{2.7}$$

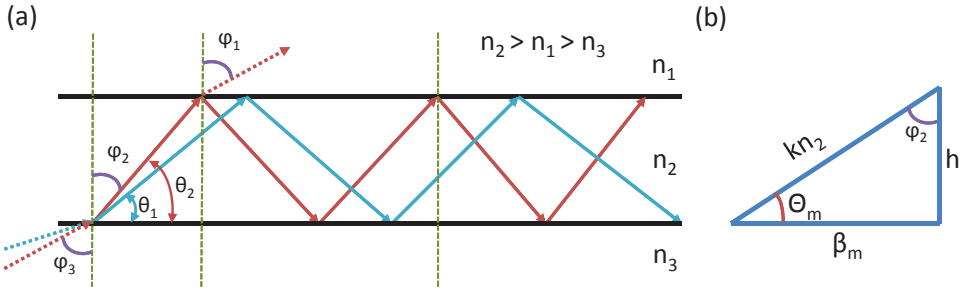

Figure 2.5 |Ray optics approach, a) Propagating plane waves undergo total internal reflection at both interfaces $n_3 - n_2$ and $n_3 - n_2$. (b) Relation between propagation constants in x and z direction and the wave vector of the propagating mode.

Where h and γ are dependent on waveguide structure. By substituting Eq. 2.7 in Eq. 2.6 the following equation is obtained:

$$\beta^2 + h^2 = K^2 n_2^2 \tag{2.8}$$

It can be seen that β, h, and kn_2 are all propagation constants with the dimension of inverse length. A wave with z propagation constant of β_m and x propagation constant of h can be represented by a plane wave with an angle of $\Theta_m = \tan^{-1}(\frac{h}{\beta_m})$ as shown in Fig. 2.5(b).

In order for the light to be guided through the layer n_2, the total internal reflection relations have to be satisfied:

$$\begin{aligned} \phi_2 &\geq sin^{-1}(\frac{n_1}{n_2}), \\ \phi_2 &\geq sin^{-1}(\frac{n_3}{n_2}) \end{aligned} \tag{2.9}$$

As $sin(\phi) = \frac{\beta}{kn_2}$ the conditions in Eq. 2.9 can also be written based on propagation vector/constants. Moreover, as the light is propagating, the total phase change for a point on a wavefront on a round trip from $n_2 - n_3$ to $n_2 - n_1$ and back to $n_2 - n_3$ interfaces must be multiple of 2π. From this, it follows that:

$$2kn_2 t\ cos(\theta_m) - 2\phi_{23} - 2\phi_{21} = 2m\pi \tag{2.10}$$

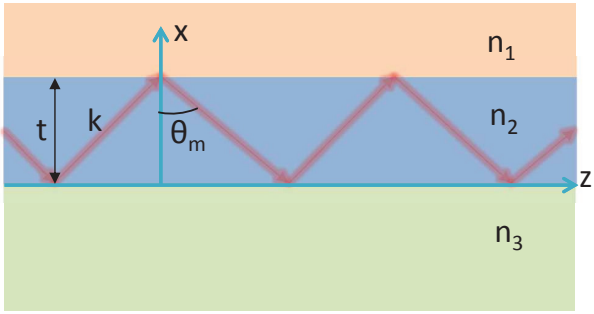

Figure 2.6 |A propagating wave and the phase relation, the total accumulated phase in a round trip must be a multiple of 2π.

As shown in Fig. 2.6, m, t, and the $2\phi_{23}/2\phi_{21}$ in Eq. 2.10 are the mode number, the thickness of the n_2 layer and the phase shift due to total internal reflection from the $2-3/2-1$ interface, respectively.

The light velocity parallel to the waveguide is $\nu = c(k/\beta)$. Now an effective index of refraction for the guided mode can be defined as:

$$n_{eff} = \frac{c}{\nu} = \frac{\beta}{k} \tag{2.11}$$

The effective index defined in Eq. 2.11 can be used to calculate the change in the wavenumber caused by the waveguide. Hence, by calculating the effective index based on the mode number, the material refractive index, and the wavelength one can quantify the light propagation in the waveguides.

2.2.2 Ring resonators

Ring resonators are indispensable elements of integrated optics. They have been used in spectral filtering [17,18], optical switching [19,20], modulators [21,22], and generation of slow and fast light [23,24]. For our applications in integration of single-quantum emitters with on-chip optical circuits and single-photon detectors, we are mostly interested in the filtering possibilities in ring resonators. Therefore, we only briefly study the spectral properties of the ring resonators.

The simplest form of a ring resonator is shown in Fig. 2.7. It consists of a looped optical path and an optical access for coupling. When the round trip phase shift in the ring equals an integer multiple of 2π, the field from the ring and the input field interfere constructively, satisfying the resonance condition for the cavity. The resonance condition can be described by [25,26]:

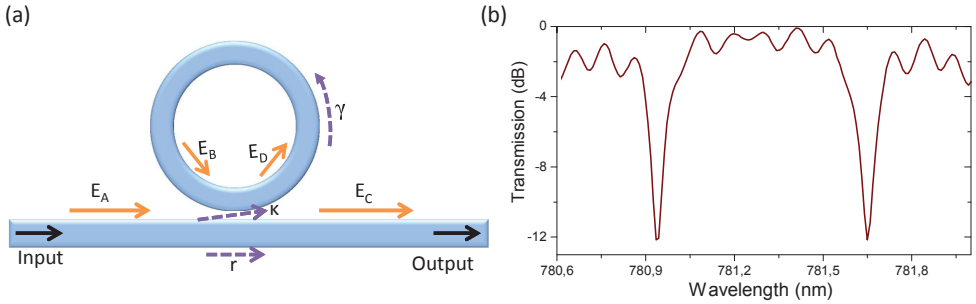

Figure 2.7 |Ring resonator, a) Schematic of a single-port ring resonator. Photons in resonance with the ring are removed from the feed-line. (b) TM mode transmission spectrum of a fabricated SiN ring resonator

$$L \cdot n_{eff}(\lambda_0) = M \cdot \lambda_0 \tag{2.12}$$

in Eq. 2.12 $L = 2\pi R$ is the length of the ring (R is the radius), n_{eff} is the effective index of the ring and M is an integer. It is clear from Eq. 2.12 that the resonance condition can be satisfied for many M values. The distance between two adjacent resonance frequencies is called Free Spectral Range (FSR) and can be calculated using:

$$FSR = \frac{\lambda^2}{n_g L} \tag{2.13}$$

Where n_g is the group index and is defined as:

$$n_g(\lambda) = n_{eff}(\lambda) - \lambda \frac{dn_{eff}(\lambda)}{d\lambda} \tag{2.14}$$

Fig. 2.7(a) illustrates a single-port ring resonator. In Fig. 2.7(a) E_A, E_C are the input field and the output field, respectively. The parameter κ is the coupling between the ring and the port and γ represents the propagation loss inside the ring.

The transmission spectrum of the ring depends mainly on the loss in a round-trip defined by field attenuation $e^{-\gamma}$ and the waveguide-ring coupling κ. The input-output relation can be defined in the form of matrix equation as[25,26]:

$$\begin{bmatrix} E_C \\ E_D \end{bmatrix} = \begin{bmatrix} t & i\kappa \\ i\kappa & t \end{bmatrix} \cdot \begin{bmatrix} E_A \\ E_B \end{bmatrix} \tag{2.15}$$

where $t = \sqrt{1-\kappa^2}$, additionally, E_B and E_D can be related as:

$$E_B = E_D \cdot e^{-\gamma + i\phi(\lambda)} \tag{2.16}$$

Where $\phi(\lambda) = n_{eff}(\lambda) \cdot \frac{2\pi}{\lambda} \cdot L$. By solving Eq. 2.15, one can obtain the the relation for the transmission of the ring[25,26]:

$$T = \left|\frac{E_C}{E_A}\right|^2 = 1 - \frac{(1 - e^{-2\gamma})(1 - t^2)}{(1 - t \cdot e^{-\gamma})^2 + 4t \cdot e^{-\gamma} sin^2\left[\phi(\lambda)/2\right]} \tag{2.17}$$

At resonance $sin^2\left[\phi(\lambda)/2\right]$ = 0 therefore:

$$T_{resonance} = \left[\frac{t - e^{-\gamma}}{1 - t \cdot e^{-\gamma}}\right]^2 \tag{2.18}$$

if $t = e^{-\gamma}$ the relation Eq. 2.18 goes to zero. This condition is called critical coupling. For most filtering applications it is desirable to design the ring to perform in the critical coupling regime. Another important parameter is the linewidth of a resonance (in wavelength or frequency). Instead of mentioning the width directly, often the quality factor is used. Quality factor (Q) is defined as the ratio between the center wavelength (or frequency) and the width of the resonance : $Q = \frac{\lambda_0}{\Delta\lambda}$. For an uncoupled ring resonator the quality factor is called the intrinsic quality factor and depends on the losses in the ring. For a coupled ring resonator the coupling works as another loss mechanism. In the critical coupling regime where the coupling and ring losses are equal the quality factor has half of its value:

$$\begin{aligned} interinsic \quad Q_i &= \frac{2\pi^2 n_g R}{\lambda_0 \gamma}, \\ critically\ coupled \quad Q &= \frac{\pi^2 n_g R}{\lambda_0 \gamma} \end{aligned} \tag{2.19}$$

The photon lifetime in the ring is directly related to Q as: $\tau_p = \frac{Q\lambda_0}{2\pi c}$. The single side-coupled ring resonator that has been discussed so far acts as a notch filter. Often it is desired to use ring resonators to select specific spectral parts and redirect the photons of those frequencies to a different optical channel. For these applications add-drop ring resonators are used.

Fig. 2.8(a) shows the schematic of an add-drop ring resonator. In add-drop configuration, the ring is side-coupled to two waveguides, through(add) port and drop port. The through port is directly connected to the output but the coupling between input and the drop port is only by means of the ring.

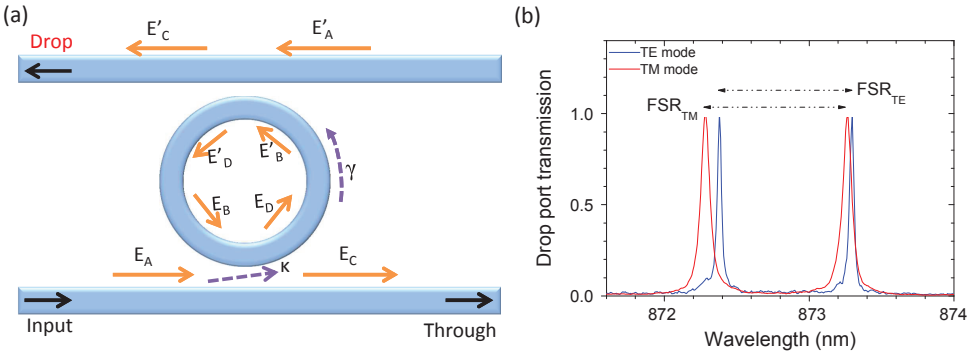

Figure 2.8 |Add-Drop ring resonator (a) Schematic of an add-drop ring resonator (b) Drop port spectra for both TE and TM modes in a fabricated SiN add-drop ring resonator. Different modes have different quality factors and free spectral ranges.

Using the same approach that we used to calculate the fields for a single side-coupled ring resonator, it can be shown that the transmission spectra of the through and drop ports are:

$$\begin{aligned} T_{through} &= \frac{(t_1 - t_2 \cdot e^{-\gamma})^2 + 4t_1 t_2 \cdot e^{-\gamma} sin^2\left[\phi(\lambda)/2\right]}{(1 - t_1 t_2 \cdot e^{-\gamma})^2 + 4t_1 t_2 \cdot e^{-\gamma} sin^2\left[\phi(\lambda)/2\right]}, \\ T_{Drop} &= \frac{e^{-2\gamma} \cdot \kappa_1^2 \cdot \kappa_2^2}{(1 - t_1 t_2 \cdot e^{-\gamma})^2 + 4t_1 t_2 \cdot e^{-\gamma} sin^2\left[\phi(\lambda)/2\right]} \end{aligned} \tag{2.20}$$

For critical coupling at the through port, it follows that $t_1 = t_2 e^{-\gamma}$. The mentioned condition means that the coupling from the through port to the ring must be equal to the round-trip loss in the ring plus the coupling of the ring to the drop port. In a symmetric add-drop ring resonator, only for the case of negligible ring loss it is possible to have both ports critically coupled. Fig. 2.8(b) shows the drop port transmission spectra for both TE and TM modes. Due to different TE and TM effective refractive indexes, the modes have different quality factors and free spectral ranges.

2.3 Single photon Detection

A vital element for all quantum optics experiments are single-photon detectors. Whether the experiment is to prove the non-classical nature of light [27,28] or using the measurement induced non-linearity for quantum computation [29,30], single-photon detectors are indispensable part of the setup.

Different technologies have been used to realize single-photon detectors. Here we briefly introduce three common techniques used for single-photon detection. We then discuss about Superconducting Nanowire Single Photon Detector(SNSPD) as our main choice for integrated quantum optics.

- Photo-multiplier tube: This relatively old technology is one of the last applications of vacuum tubes still in use today. These detectors are constructed in a vacuum glass housing incorporating: a coated thin film of conducting layer on the inside of an entry window acting as the photocathode, several dynodes, and an anode. Incident photons hit the photocathode and create low energy primary electrons due to photoelectric effect. These electrons are then focused and directed toward the electron multiplier, where in every stage more electrons are created by the process of secondary electrons. At the last stage a large number of electrons are available sufficient to produce an easily detectable pulse. Although photo-multiplier tube are still used in different applications from astronomy to blood analysis devices, their use as single-photon detector is limited due to their lower sensitivity and higher dark noise (non-zero current without presence of any incident photon) comparing to other techniques.

- single-photon avalanche diode (SPAD): This solid state detector operation is based on impact ionization. A semiconductor photodiode is reversed biased well above the breakdown voltage, an incident photon creates one or more electron-hole pairs. These electrons are accelerated with a large electric field to knock out additional carriers from the valence band and promote them to the conduction band. The newly created electrons in turn generate more electrons and soon after the absorption of the photon an avalanche current is formed, which is easily detectable. SPADs are widely used in quantum optics experiments in visible and near-infrared range for their combination of efficiency, price, and relatively low noise and jitter. However, their use in the mid-infrared and in applications requiring high time resolution is limited. The efficiency in the mid-infrared is limited by the bandgap of the semiconductor while the time response is mainly dictated by the rc constant associated with the p-n junction and the contacts.

- Superconducting Nanowire Single Photon Detector (SNSPD): The working principle of these relatively new type of detectors is based on the collapse of the superconducting state by absorbing a single photon in a superconducting nanowire biased close to its critical current. The exact detection mechanism is still under debate but a single photon incident on the detector can break Cooper pairs and this will either generate growing region with reduce superconductivity[31] or crossing of a vortex[32]. As a result, a belt of resistive region is formed along the wire which grows due to Joule heating i.e. the power dissipated because of current passing through the resistor. The resistive region can grow up to several kilo ohms[33] The sudden change in the resistance of the wire diverts the current from the nanowire into readout circuits resulting in a voltage pulse, typically a few hundred microvolts. These pulses are then amplified

and used to register the detection events. The reduced current through the nanowire causes reduction in heat dissipation and it can cool down to its superconducting state again, making the device ready for another subsequent detection event. SNSPDs are the detector of choice in many modern applications because of their combination of unparalleled speed, low noise and jitter and high efficiency specially in the near and mid infrared. As this detector is also well suited for integration, we will discuss it in more details in the following sections.

2.3.1 Superconducting single-photon detector

Because SNSPDs offer unparalleled features and since they are the suitable technology for integration, we briefly discuss the main concepts connected to their performance.

Efficiency and speed

As discussed, the detection mechanism in SNSPDs is through suppression of the superconducting state in part of a nanowire. The detection efficiency of SNSPDs depends on many parameters but they can be divided in two major categories: the internal efficiency and the external (absorption) efficiency. The internal efficiency is the probability of generation of a detection pulse after a photon is absorbed by the SNSPD. Upon absorption of a photon by the detector the superconducting state in part of the nanowire is disturbed. The probability that this disturbance produces a resistive region across the width of the wire depends on the energy of the photon, bias current, the wire geometry, and the film properties. The internal detection probability for a single photon can be determined by[34]:

$$\eta_{det} = e^{\frac{-E(I)}{\hbar\omega}} \tag{2.21}$$

in Eq. 2.21 $E(I)$ is an energy scale which depends on bias current relative to critical current of that nanowire region. Since SNSPDs are series structures, as a result the critical current of each device is dictated by the region with the lowest critical current. So any constriction in the nanowire or inhomogeneity in the film would affect the internal efficiency.

External efficiency, the second major contributor to the system detection efficiency (overall efficiency), is explained by the coupling and absorption probabilities; meaning how many photons out of all incident ones are coupled to (coupling efficiency) and absorbed by (absorption efficiency) the detector.

To couple most of the light in the active area of the detector, stand-alone SNSPDs are made in the form of a meander covering an area of about 100-200 μm^2. An example of such device is shown in Fig. 2.9(a). The typical filling factor is 50% i.e. the width of the wire is similar to the spacing between them. The area of the device is set by the coupling scheme. It is often desired to use an optical fiber to couple light to a detector.

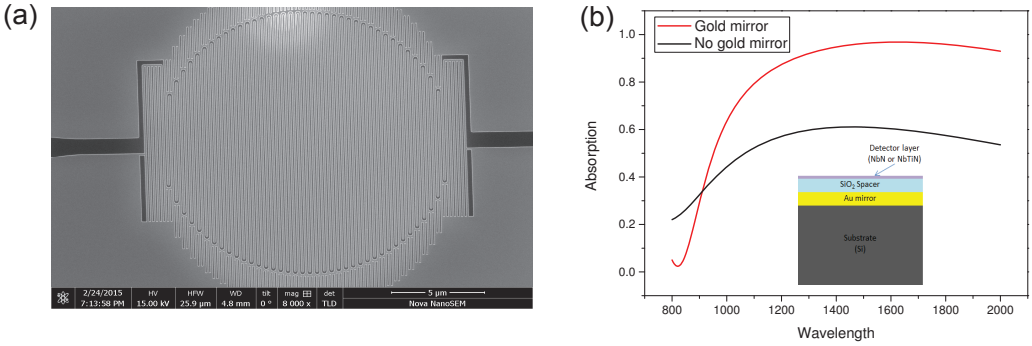

Figure 2.9 |Absorption efficiency in SNSPDs, (a) SEM photo of a fabricated SNSPD. (b) Absorption efficiency as a function of wavelength for an SNPSD with and without gold mirror. The mirror enhances the absorption efficiency significantly.

Incident light toward the detector can be transmitted, reflected or absorbed. The ratio of absorption to the total incident light is called absorption efficiency. As a first order approximation the absorption efficiency can be calculated by the transfer matrix method. This analytical approach is used to calculate the transmission and reflection through a multilayer stack of materials via assigning a matrix to each layer of the stack[35,36]. These matrices can then be multiplied and applied to the incident beam. By rewriting the input-output relation one can easily extract the reflection and transmission for the whole stack.

We use transfer matrix method to simulate the absorption in an SNSPD fabricated on oxidized silicon with and without a mirror between the silicon substrate and the silicon oxide layer. Fig. 2.9(b) represents the simulation results and the inset illustrates the optical layers which was used in the simulation. The thickness of the layers are 6 nm (NbTiN), 267 nm (SiO_2), 100 nm (Au). for the sake of simplicity, a constant refractive index was used throughout the wavelength range of the simulation (the simulation result with real values, acquired from ellipsometry measurements, are similar for this range). As shown in the figure the stack with the gold mirror has significantly higher absorption.

The time behaviour of an SNSPD upon absorption of a photon can be modelled with a set of coupled differential equations[37]. A 1D heat equation can be used to approximate the time dependent thermal behaviour of SNSPDs. This equation has two parts, the passive part which contributes to the heat propagation and the active part which is responsible for heat generation after the formation of a resistive region across the nanowire. The active part of the heat equation is coupled to the electrical circuit through current and resistance. The resistance calculated from the heat equation is fed into a circuit equation and from there the current is calculated and returned into the heat equation. This is illustrated in Fig. 2.10 and formulated in Eq. 2.22 .

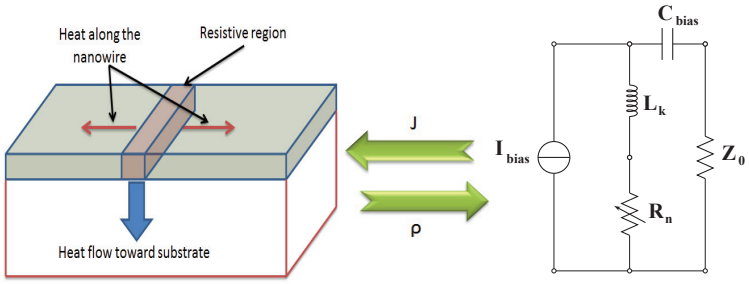

Figure 2.10 |SNSPD electrothermal model, After absorption of a photon, the electrical and thermal evolution of the SNSPD are linked through J and ρ.

$$\begin{aligned} \frac{\partial cT}{\partial t} &= J^2\rho + \kappa\frac{\partial^2 T}{\partial x^2} - \frac{\alpha}{d}(T - T_{sub}) \\ I_{bias} - I &= C_{bias}\left(\frac{\partial L_k I}{\partial t^2} + \frac{d(IR_n)}{dt} + Z_0\frac{dI}{dt}\right) \end{aligned} \tag{2.22}$$

where for the thermal part of Eq. 2.22, c is the specific heat per unit volume for the detector material, T is an array containing the temperature values for all segments of SNSPD, J is the current density, ρ is the electrical resistivity and it has a non-zero value when the segment is not superconducting, κ is the thermal conductivity of the SNSPD, α is the thermal conduction at the boundary of the film with substrate, d is the thickness of the nanowire and finally, T_{sub} is the substrate temperature. As for the electrical part, I_{bias} is the bias current, I is the current passing through the device, C_{bias} is the coupling capacitor (usually used in a bias-T circuit) between the readout circuitry and the detector, L_k is the kinetic inductance of the nanowire and R_n and Z_0 are the total detector resistance and readout impedance respectively.

Dark count and jitter

Dark counts in SNSPDs are the detection pulses generated when the device is not illuminated, they are undesired false counts which can corrupt the measurement. The origin of dark count is not well known but it is often ascribed to the crossing of vortices along the width of the nanowire[38].

Dark counts are temperature and current dependent. This relation has the form of[39]:

$$R_{dk} \propto R_0 e^{\frac{I_b}{I_c}} \tag{2.23}$$

Figure 2.11 |SNSPD evanescent coupling. An SNSPD is placed in the evanescent field of a waveguide. The light can be absorbed quickly making the size of the required detector.

here R_{dk} represents the dark count rate, I_b is the bias current and I_c is the critical current of SNSPD. R_0 in Eq. 2.23 is a temperature dependent factor.

Another important performance parameter for SNSPD is their associated timing jitter. This is defined as the uncertainty in arrival time of a detection pulse with respect to an incoming pulse of light. The jitter has two parts:

- The fundamental jitter: based on the physics of the events which takes place after absorption of a photon in a segment of a detector. These mechanisms are associated with different relaxation times for electron and phonons in the superconductor. The value for these characteristic times are shown to be material, current and wavelength dependent[31].

- The External jitter: due to the readout circuitry designed to register the detection events. It can be understood by considering that the readout circuit, in a general form, consists of an amplifier and a discriminator; any noise in the input of the amplifier is amplified and fed into the discriminator causing uncertainty in the trigger time.

On-chip single-photon detector

As discussed, a major contributor to the detection efficiency of SNSPDs is the absorption efficiency. Cavity enhanced absorption for out of plane coupling to the detector has been realized[40]. Another way to increase the efficiency is through evanescent coupling. This method is of special interest for us as it allows for integration. In this approach the light which is confined in an optical waveguide is slowly coupled to the detector through evanescent field. Fig. 2.11 visualizes the evanescent coupling where an SNSPD is placed on top of a dielectric waveguide. This method of coupling allows for very high absorption efficiency[41], low dark count[42] and integration with complex photonic circuits[43].

Bibliography

[1] T.B. Pittman, B.C. Jacobs, and J.D. Franson. Heralding single photons from pulsed parametric down-conversion. *Optics Communications*, 246(4–6):545–550, 2005.

[2] P. Michler, A. Kiraz, C. Becher, W. V. Schoenfeld, P. M. Petroff, Lidong. Zhang, E. Hu, and A. Imamoglu. A quantum dot single-photon turnstile device. *Science*, 290(5500):2282–2285, 2000.

[3] Matthew. Pelton, Charles. Santori, Jelena. Vučković, Bingyang. Zhang, Glenn. S. Solomon, Jocelyn. Plant, and Yoshihisa. Yamamoto. Efficient source of single photons: A single quantum dot in a micropost microcavity. *Phys. Rev. Lett.*, 89:233602, 2002.

[4] F. Jelezko and J. Wrachtrup. Single defect centres in diamond: A review. *physica status solidi (a)*, 203(13):3207–3225, 2006.

[5] J. McKeever, A. Boca, A. D. Boozer, R. Miller, J. R. Buck, A. Kuzmich, and H. J. Kimble. Deterministic generation of single photons from one atom trapped in a cavity. *Science*, 303(5666):1992–1994, 2004.

[6] M. Keller, B. Lange, K. Hayasaka, W. Lange, and H. Walther. Continuous generation of single photons with controlled waveform in an ion-trap cavity system. *Nature*, 431:1075–1078, 2004.

[7] Christian. Brunel, Brahim. Lounis, Philippe. Tamarat, and Michel. Orrit. Triggered source of single photons based on controlled single molecule fluorescence. *Phys. Rev. Lett.*, 83:2722–2725, 1999.

[8] Ville. Ahtee, Robert. Lettow, Robert. Pfab, Alois. Renn, Erkki. Ikonen, Stephan. Götzinger, and Vahid. Sandoghdar. Molecules as sources for indistinguishable single photons. *Journal of Modern Optics*, 56(2-3):161–166, 2009.

[9] Bernhard. Loitsch, Julia. Winnerl, Gianluca. Grimaldi, Jakob. Wierzbowski, Daniel. Rudolph, Stefanie. Morkötter, Markus. Döblinger, Gerhard. Abstreiter, Gregor. Koblmüller, and Jonathan J. Finley. Crystal phase quantum dots in the ultrathin core of gaas–algaas core–shell nanowires. *Nano Letters*, 15(11):7544–7551, 2015.

[10] Oliver. Gywat, Hubert. J. Krenner, and Jesse. Berezovsky. Theory of confined states in quantum dots. In *Spins in Optically Active Quantum Dots*, chapter 3, pages 39–66. Wiley-VCH Verlag GmbH & Co. KGaA, 2010.

[11] Dan. Dalacu, Khaled. Mnaymneh, Jean. Lapointe, Xiaohua. Wu, Philip. J. Poole, Gabriele. Bulgarini, Val. Zwiller, and Michael. E. Reimer. Ultraclean emission from inasp quantum dots in defect-free wurtzite inp nanowires. *Nano Lett.*, 12:5919–5923, 2012.

[12] Ethan. D. Minot, Freek. Kelkensberg, Maarten. van Kouwen, Jorden. A. van Dam, Leo. P. Kouwenhoven, Valery. Zwiller, Magnus. T. Borgström, Olaf. Wunnicke, Marcel. A. Verheijen, and Erik. P. A. M. Bakkers. Single quantum dot nanowire leds. *Nano Letters*, 7(2):367–371, 2007.

[13] Yong. Ma, Peter. E. Kremer, and D. Brian. Gerardot. Efficient photon extraction from a quantum dot in a broad-band planar cavity antenna. *Journal of Applied Physics*, 115(2), 2014.

[14] Jelena. Vučković, David. Fattal, Charles. Santori, Glenn. S. Solomon, and Yoshihisa. Yamamoto. Enhanced single-photon emission from a quantum dot in a micropost microcavity. *Applied Physics Letters*, 82(21):3596–3598, 2003.

[15] Michael. E. Reimer, Gabriele. Bulgarini, Nika. Akopian, Moira. Hocevar, Maaike. B. Bavinck, Marcel. A. Verheijen, Erik. P.A.M. Bakkers, Leo P. Kouwenhoven, and V. Zwiller. Bright single-photon sources in bottom-up tailored nanowires. *Nat. Commun.*, 3:737, 2012.

[16] Robert. G. Hunsperger. *Integrated Optics*, pages 17–52. Springer New York, 2009.

[17] Fengnian. Xia, Mike. Rooks, Lidija. Sekaric, and Yurii. Vlasov. Ultra-compact high order ring resonator filters using submicron silicon photonic wires for on-chip optical interconnects. *Opt. Express*, 15(19):11934–11941, 2007.

[18] Nicholas C. Harris, Davide. Grassani, Angelica. Simbula, Mihir. Pant, Matteo. Galli, Tom. Baehr-Jones, Michael. Hochberg, Dirk. Englund, Daniele. Bajoni, and Christophe. Galland. Integrated source of spectrally filtered correlated photons for large-scale quantum photonic systems. *Phys. Rev. X*, 4:041047, 2014.

[19] William S. Fegadolli, German Vargas, Xuan Wang, Felipe Valini, Luis A. M. Barea, José E. B. Oliveira, Newton Frateschi, Axel Scherer, Vilson R. Almeida, and Roberto R. Panepucci. Reconfigurable silicon thermo-optical ring resonator switch based on vernier effect control. *Opt. Express*, 20(13):14722–14733, 2012.

[20] Y. Henry Wen, Onur. Kuzucu, Taige. Hou, Michal. Lipson, and Alexander. L. Gaeta. All-optical switching of a single resonance in silicon ring resonators. *Opt. Lett.*, 36(8):1413–1415, 2011.

[21] Takeshi. Baba, Suguru. Akiyama, Masahiko. Imai, Naoki. Hirayama, Hiroyuki. Takahashi, Yoshiji. Noguchi, Tsuyoshi. Horikawa, and Tatsuya. Usuki. 50-gb/s ring-resonator-based silicon modulator. *Opt. Express*, 21(10):11869–11876, 2013.

[22] B. Bortnik, Yu-Chueh. Hung, Hidehisa. Tazawa, Byoung-Joon. Seo, Jingdong. Luo, Alex. K.-Y. Jen, William. H. Steier, and Harold. R. Fetterman. Electrooptic polymer ring resonator modulation up to 165 ghz. *Selected Topics in Quantum Electronics, IEEE Journal of*, 13(1):104–110, 2007.

[23] Ali. W. Elshaari, Abdelsalam. Aboketaf, and Stefan. F. Preble. Controlled storage of light in silicon cavities. *Opt. Express*, 18(3):3014–3022, 2010.

[24] Sasikanth. Manipatruni, Po. Dong, Qianfan. Xu, and Michal. Lipson. Tunable superluminal propagation on a silicon microchip. *Opt. Lett.*, 33(24):2928–2930, 2008.

[25] Qianfan. Xu. *controlling the flow of light on chip with microringresonator based silicon photonic devices*. PhD thesis, Cornell University, United States, 2007.

[26] Freddy. S. Tan. *Integrated optical filters based on microring resonators*. PhD thesis, University of Twente, The Netherlands, 2004.

[27] P. Grangier, G. Roger, and A. Aspect. Experimental evidence for a photon anticorrelation effect on a beam splitter: a new light on single-photon interferences. *Europhysics Letters*, pages 173–179, 1986.

[28] C. K. Hong, Z. Y. Ou, and L. Mandel. Measurement of subpicosecond time intervals between two photons by interference. *Phys. Rev. Lett.*, 59:2044–2046, 1987.

[29] Robert. Raussendorf, Daniel. E. Browne, and Hans. J. Briegel. Measurement-based quantum computation on cluster states. *Phys. Rev. A*, 68:022312, 2003.

[30] Robert. Raussendorf and Tzu-Chieh. Wei. Quantum computation by local measurement. *Annual Review of Condensed Matter Physics*, 3(1):239–261, 2012.

[31] Francesco. Marsili, Martin. J. Stevens, Alexander. Kozorezov, Varun. B. Verma, Colin. Lambert, Jeffrey. A. Stern, Robert. Horansky, Shellee. D. Dyer, Matthew. D. Shaw, Richard. P. Mirin, and Sae. Woo. Nam. Hotspot dynamics in current carrying wsi superconducting nanowires. In *CLEO: 2014*, page FM4B.7, 2014.

[32] J. J. Renema, R. Gaudio, Q. Wang, Z. Zhou, A. Gaggero, F. Mattioli, R. Leoni, D. Sahin, M. J. A. de Dood, A. Fiore, and M. P. van Exter. Experimental test of theories of the detection mechanism in a nanowire superconducting single photon detector. *Phys. Rev. Lett.*, 112:117604, 2014.

[33] Joel. K.W. Yang, A. J. Kerman, E. A. Dauler, V. Anant, K. M. Rosfjord, and K. K. Berggren. Modeling the electrical and thermal response of superconducting nanowire single-photon detectors. *Applied Superconductivity, IEEE Transactions on*, 17(2):581–585, 2007.

[34] Reinier. W. Heeres and Valery. Zwiller. Superconducting detector dynamics studied by quantum pump-probe spectroscopy. *Applied Physics Letters*, 101(11), 2012.

[35] Malvin. Carl. Teich Bahaa. E. A. Saleh. *Fundamentals of Photonics, 2nd Edition*. John Wiley & Sons, Inc., 2007.

[36] M. G. Tanner, C. M. Natarajan, V. K. Pottapenjara, J. A. O'Connor, R. J. Warburton, R. H. Hadfield, B. Baek, S. Nam, S. N. Dorenbos, E. Bermúdez. Ureña, T. Zijlstra, T. M. Klapwijk, and V. Zwiller. Enhanced telecom wavelength single-photon detection with nbtin superconducting nanowires on oxidized silicon. *Applied Physics Letters*, 96(22), 2010.

[37] Andrew. J. Kerman, Joel. K. W. Yang, Richard. J. Molnar, Eric. A. Dauler, and Karl. K.Berggren. Electrothermal feedback in superconducting nanowire single-photon detectors. *Phys. Rev. B*, 79:100509, 2009.

[38] L. N. Bulaevskii, Matthias. J. Graf, and V. G. Kogan. Vortex-assisted photon counts and their magnetic field dependence in single-photon superconducting detectors. *Phys. Rev. B*, 85:014505, 2012.

[39] Sander. Nugraha. DORENBOS. *Integrated optical filters based on microring resonators*. PhD thesis, Delft University of Technology, The Netherlands, 2011.

[40] F. Marsili, V. B. Verma, J. A. Stern, S. Harrington, A. E. Lita, T. Gerrits, I. Vayshenker, B. Baek, M. D. Shaw, R. P. Mirin, and S. W. Nam. Detecting single infrared photons with 93% system efficiency. *Nat. Photon.*, 7(3):210–214, 2013.

[41] W. H. P. Pernice, C. Schuck, O. Minaeva, M. Li, G. N. Goltsman, A. V. Sergienko, and H. X. Tang. High-speed and high-efficiency travelling wave single-photon detectors embedded in nanophotonic circuits. *Nat. Commun.*, 3:1325, 2012.

[42] Carsten. Schuck, Wolfram. H. P. Pernice, and Hong. X. Tang. Waveguide integrated low noise nbtin nanowire single-photon detectors with milli-hz dark count rate. *Scientific Reports*, 3:1893, 2013.

[43] Mohsen. K. Akhlaghi, Ellen. Schelew, and Jeff. F. Young. Waveguide integrated superconducting single-photon detectors implemented as near-perfect absorbers of coherent radiation. *Nat. Commun.*, 6, 2015.

Chapter 3

Fabrication and Measurement Setups

This chapter covers experimental aspects of this thesis. For this work, we fabricate and characterize a variety of nano-photonic chips. All nanofabrications were carried out in the Van Leeuwenhoek Laboratory (VLL) and all optical and electrical measurements were conducted in the optics lab of the Kavli institute of nanoscience in Delft.

3.1 Introduction

We process, fabricate, and integrate single photon sources, optical circuits and single photon detectors. The nanofabrications include (but not limited to), e-beam lithography, metal evaporation and lift-off, sputtered deposition, plasma enhanced chemical vapor deposition (PECVD), reactive ion etching (RIE), and deep reactive ion etching (DRIE). Additionally, complementary processes such as nano-positioning of the nanowire QDs and wire bondings were done in the general facilities of Quantum Transport (QT) division of the Kavli institute of Delft.

3.2 Nano Fabrication in VLL

All nanofabrications relevant to this thesis were carried out in VLL clean room in Kavli institute of nanoscience in Delft. The VLL clean room offers:

- High-resolution electron beam lithography
- Optical lithography

- Focused ion beam
- Mask fabrication for optical lithography
- Physical vapour deposition (evaporation, sputtering)
- Chemical vapour deposition (LPCVD, PECVD, ALD)
- Dry etching
- Wet processing
- Thermal processing
- High resolution inspection

3.2.1 Processing single photon emitters

The single photon sources used in this thesis are provided by several other labs. We then process these sources in VLL and measure them in the optics lab. The processes includes: nanomanipulation (pick and place), metalization (contacting), fiber coupling, and incorporation in photonic circuits. Fig. 3.1 provides examples of processed single photon sources.

3.2.2 Fabrication of photonic circuits

Our photonic circuits were fully fabricated in VLL. The fabrication of photonic circuits starts by first thermally oxidizing bare silicon chips. We usually form an oxide layer with a thickness of 2-3 μm on top of the silicon chips. This oxide layer serves as a low refractive index buffer layer between the waveguide and the high index silicon substrate. Since most of the dielectric waveguides have lower index of refraction than silicon, the buffer layer is necessary to ensure confinement in the waveguide.

Fig. 3.2 demonstrates the fabrication flow of photonic circuits; it is worth mentioning that the order of the optional step of metalization and waveguide layer deposition can be interchanged. Table. 3.1 provides the fabrication details for the steps mentioned in Fig. 3.2.

Fig. 3.3 shows examples of fabricated devices. When heaters and electronic structures are required, we use e-beam markers to position the photonic and electronic structures accordingly with a precision better than 15 nm.

3.2.3 Fabrication of superconducting nanowire single photon detectors

We fabricate superconducting nanowire single photon detectors in VLL on thin (6-8 nm) films of NbTiN. The films are grown, either in VLL or in outside foundries, using DC magnetron

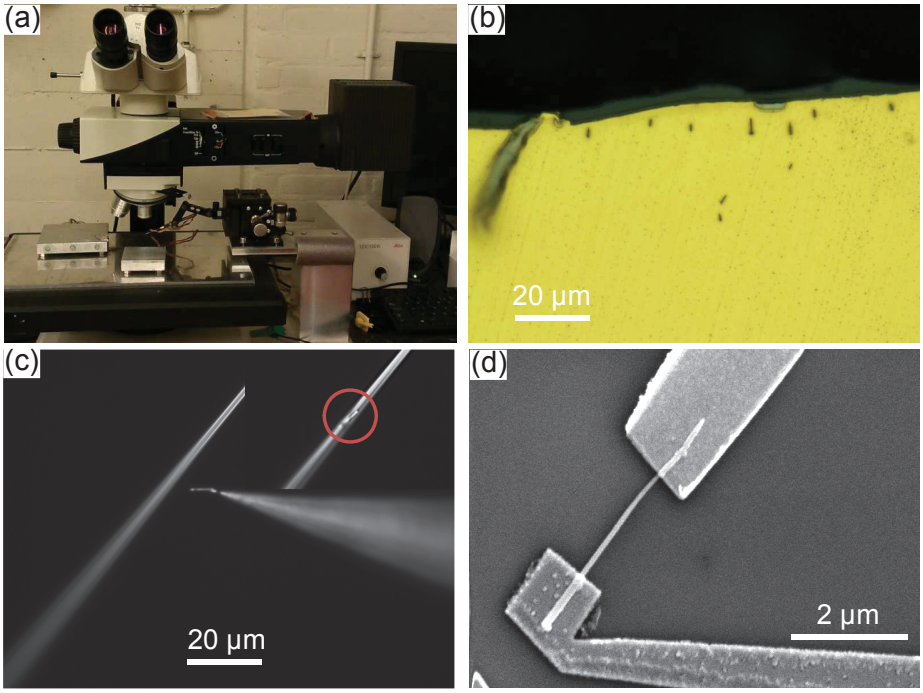

Figure 3.1 | Processing single photon sources, (a) Photo of a nanomanipulator used to transfer nanowires from the as-grown chip to the new substrates. (b) nanowires deposited and aligned to the edge of a piezo electric (PMN-PT) chip. (c) The nanomanipulator tip carrying a nanowire is approaching a tapered optical fiber. The inset shows the nanowire after transfer on the tapered optical fiber. (d) SEM picture of a transferred and contacted p-n junction nanowire.

Table 3.1 |Fabrication details of photonic circuits.

Metalization step(s)		
Resist	Developer	Evaporation
Bilayers PMMA 495K-A6 and PMMA 950K-A2	MIBK:IPA 1:3	Ti/ Au or Cr/Au *
PECVD details		
Material	Gases	RF source
SiN_x	$SiH_4 + NH_3$ **	13 MHz
Waveguide layer patterning		
Resist	Developer	RIE Etchants
PMMA 950K-A4	MIBK:IPA 1:3	CHF_3 *and* Ar ***

* We deposit Cr/Au (5/50 nm) for markers and Ti/Au (80-100/0-5 nm) for heaters.
(these steps can be merged to a single step by adding 5 nm more gold)
** the gas ratio is 1, similar to[1] .
*** The gas concentrations are $CHF_3 = 50\ SCCM$ *and* $Ar = 25\ SCCM$
the RF power and process pressure are set at 50 W and 0.0092 mbar, respectively.

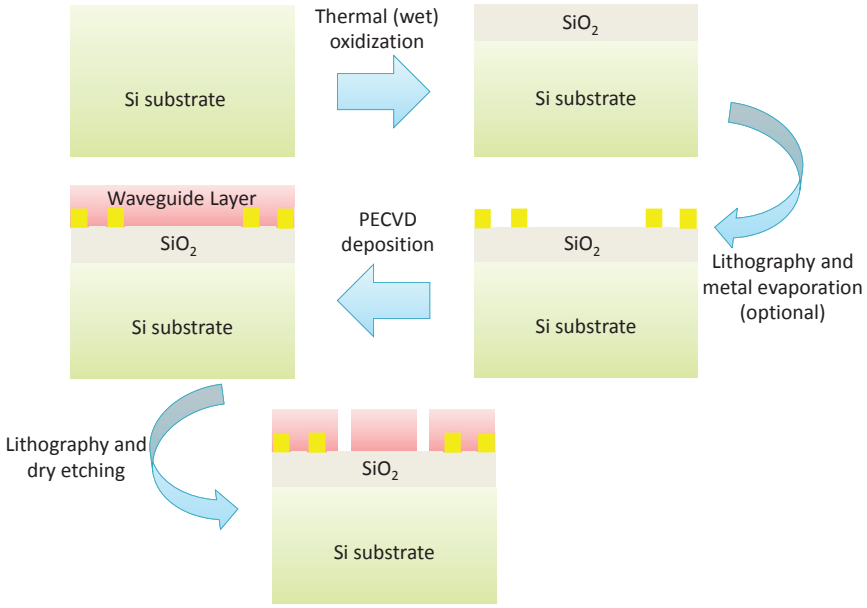

Figure 3.2 | Photonic circuits fabrication flow, the process starts by thermal oxidation of silicon wafers. If necessary, markers and heaters are formed by e-beam lithography and lift-off. Waveguide layer is then added using PECVD. Finally, the waveguides are formed using e-beam lithography and reactive ion etching.

sputtering. The fabrication starts by forming the metal contacts. We use e-beam lithography followed by evaporation of Cr/Au (5 nm/50 nm) and lift-off in acetone. After this step, the chip is spin coated with HSQ (XR1541):MIBK 1:1 and exposed with e-beam. Following the e-beam exposure, the resist is developed and the pattern is transferred to the superconducting layer with reactive ion etching. Table. 3.2 and Fig. 3.4 present the fabrication details and examples of fabricated devices, respectively.

Fiber coupling by deep etching of substrate is another step that can be added after fabrication of SNSPDs. Fiber coupling is required if the devices are to be used as standalone elements of a quantum optical circuit (instead of being integrated on the same chip as the photonic circuits and quantum emitters). As deep etching is also important in other processes as well, for example fiber coupling of single photon sources, we discuss it in a separate Section 3.4.

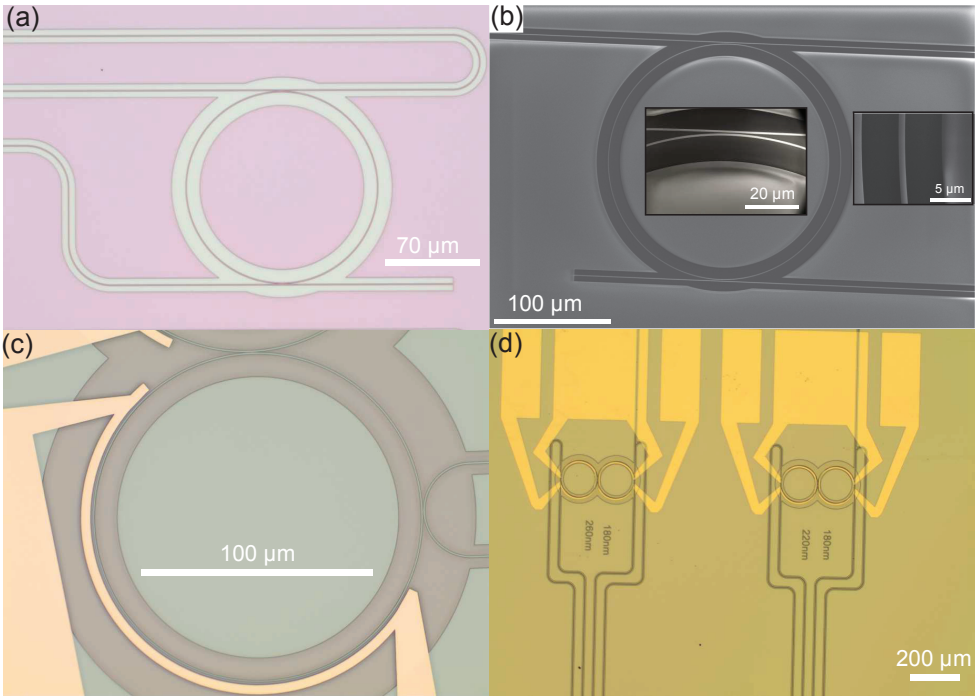

Figure 3.3 | Photonic circuits fabrication examples, (a) A ring resonator formed after exposure of PMMA 950K A4 and development with MIBK:IPA. (b) SEM image of a ring resonator after etching with CHF_3/Ar. Insets show magnified images of the same ring resonator. (c) A double ring CROW resonator with side heaters. (d) CROW resonators with top heaters. In this case the heater and the photonic layer are separated by $3\,\mu m$ of PECVD SiO_2

.

Table 3.2 |Fabrication details of SNSPDs.

Metalization step(s)		
Resist	Developer	Evaporation
Bilayers PMMA 495K-A6 and PMMA 950K-A2	MIBK:IPA 1:3	Cr/Au
Patterning of superconducting detector		
Resist	Developer	RIE Etchants
HSQ (XR1541):MIBK 1:1	TMAH, MF322, H_2O	SF_6 *and* O_2 *

* The gas concentrations are $SF_6 = 13.5\,SCCM$ *and* $O_2 = 5\,SCCM$
the RF power and process pressure used are 50 W and $\sim$0.005 mbar, respectively.

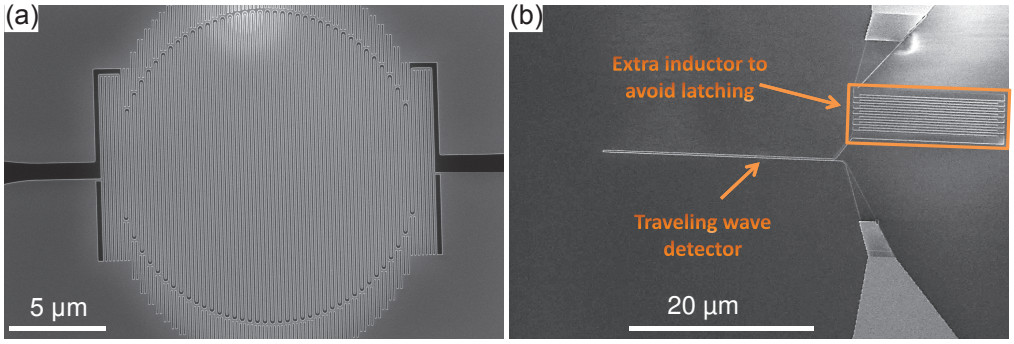

Figure 3.4 | SNSPD fabrication examples, (a) An SNSPD fabricated for coupling to a single mode fiber. (b) Fabricated superconducting traveling wave detector for integration with a photonic waveguide. The extra meandering region serves as extra inductor to avoid latching of the detector.

3.3 Integrated hybrid systems

To achieve a scalable quantum photonic platform, it is required to interface all discussed different technologies. We fabricate devices combining all mentioned elements. Fig. 3.5 represents examples of fabricated hybrid devices.

3.4 Deep etching and source/detector fiber coupling

We use Bosch technique[2] for deep etching of silicon substrates, it is possible to achieve highly anisotropic etch profile useful for fiber coupling of detectors and sources. In addition, by changing the etching parameters, isotropic etch is also available. Combination of directional and isotropic etch can be used to fabricate free-standing membranes.

Bosch etching is a two steps process: short isotropic etch (using SF_6 for silicon) followed by a passivation step (C_4F_8 in our process); these steps are repeated many times until the etching is completed. Our deep etching recipe is shown in Fig. 3.6(a); it consists of a three layers mask similar to[3]. Each mask is used to selectively etch the lower layer. For deep etching of silicon we use single layer of AZ9216 or multiple layers of AZ5214 as mask. The photoresist has a selectively of greater than 300 against silicon. Fig. 3.6(b),(c), and (d) provide some examples of devices made by directional and isotropic deep etch.

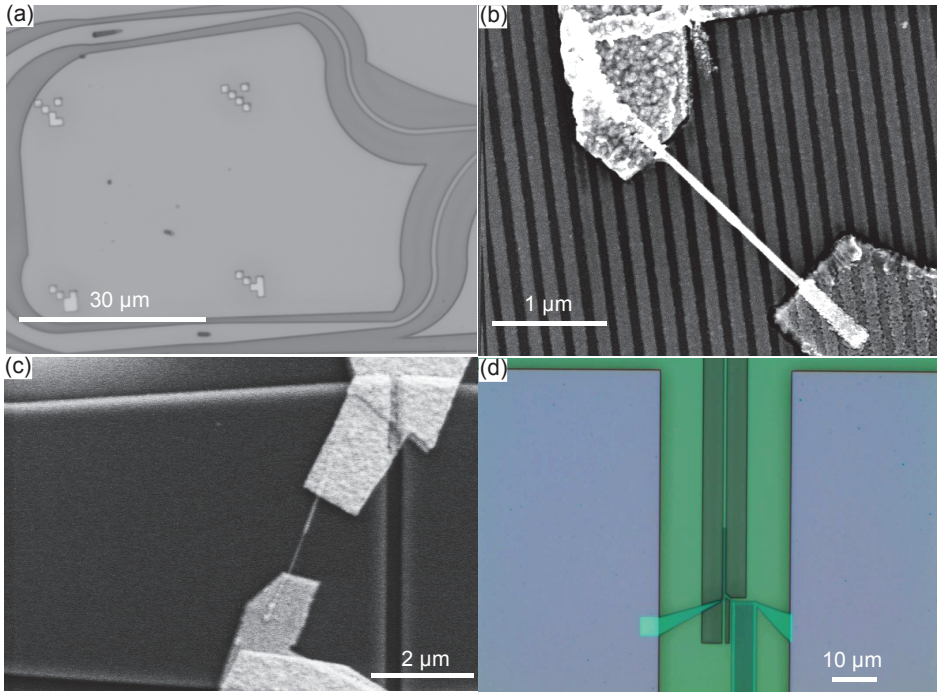

Figure 3.5 | Examples of hybrid integrated devices.(a) Nanowire QDs positioned and incorporated into silicon nitride waveguides. (b) Contacted semiconducting nanowires with a p-n junction on top of an SNSPD, separated by a thin insulating layer.(c) Contacted p-n junction nanowire on a photonic channel. (d) A travelling wave SNSPD fabricated under a silicon nitride waveguide.

3.5 Experimental setup

After nanofabrication is completed, the devices are prepared in the optics lab for measurements. Most of our measurements with nanowires and waveguides are done in a continuous flow cryostat. The only exceptions are the experiments where SNSPDs are involved or the sample (either detector or source) is fiber coupled. For those cases we either use a bath cryostat or directly immerse the sample into a He dewar.

Dedicated electronics, which are fully developed at the Kavli institute Delft, are used to sweep current through semiconducting sources and superconducting detectors. For microheaters, thanks to high athermal properties of silicon nitride (Chapter 6) regular power supplies are stable enough as the tuning knobs.

Fig. 3.7(a) provides the schematic of the QDs and waveguides measurement setup. Shown

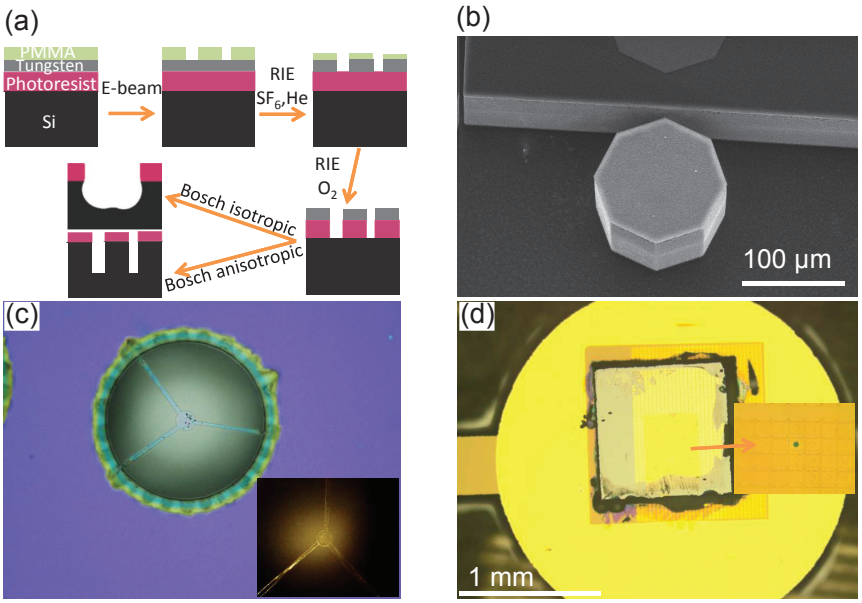

Figure 3.6 | Deep reactive ion etching, (a) Process flow for deep etching of silicon. We use a three layers mask and e-beam lithography followed by two steps reactive ion etching. The process is completed by Bosch etching. Bosch etching can be isotropic or directional (anisotropic). (b) An example of directional Bosch etching. (c) Shown is a 200 nm thick glass membrane formed by combination of isotropic and directional Bosch etching. (d) A GaAs chip with self assembled QDs is glued into a half-way etched pocket in a silicon sample formed by directional Bosch etching. Another Bosch etching step (complete etching to the other side of the silicon piece) is used to form the keyhole shape with a selected QD at its center. Now the selected QD can be mounted in FC-sleeve and be coupled to an optical fiber.

in the picture, the "U" configuration, is the more general form of the setup. This configuration is very versatile when it comes to characterizing ring resonators. It is clear that the setup can also be operated in the more conventional μPL configuration i.e. straight line excitation and collection. The combined top/side imaging provides an easy way for evaluating the coupling to the waveguide devices as well as providing the possibility to excite in plane or out of plane if needed.

Fig. 3.7(b) shows the actual setup; excitation, collection and imaging paths are highlighted in the image. Fig. 3.7(c) is a zoomed photo of the two imaging stages with two insets showing snapshots of the side and top objective images captured while characterizing a ring resonator.

As mentioned before, we fabricate fiber coupled detectors and sources. Fig. 3.7(d) shows

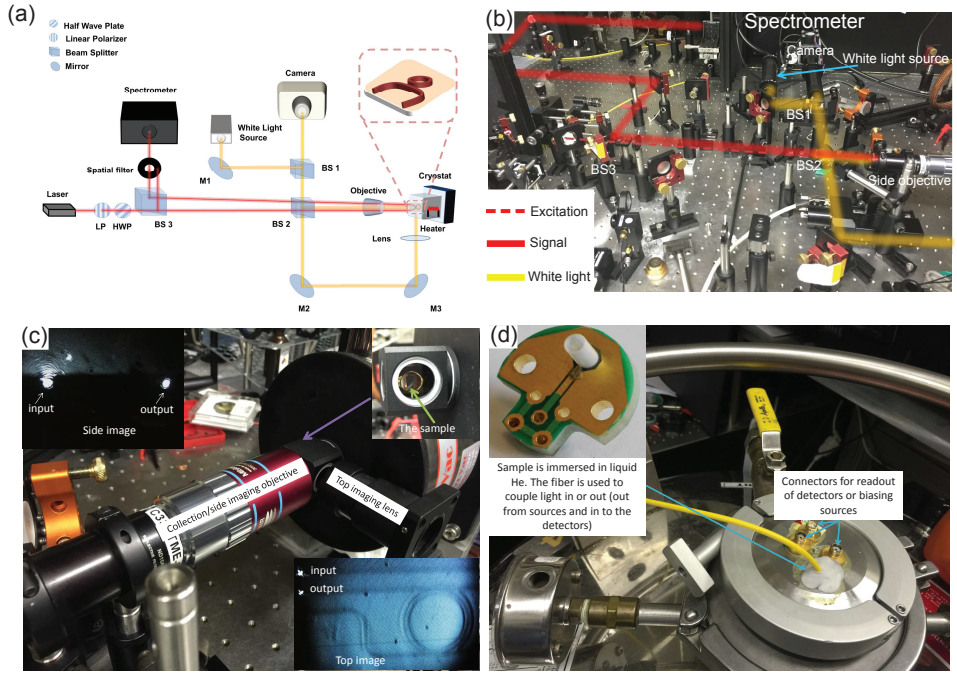

Figure 3.7 | Some of experimental setups which were used in this these. (a) Schematic of the QDs and waveguides measurement setup in "U" configuration. The samples can be accessed both in-plane and out-of-plane. (b) The actual setup used for the measurements of QDs and waveguides. The paths are highlighted in the pictures. (c) A zoomed photo of the two objectives used for top/side accesses. The top left and bottom right insets are two snapshots of side and top images, respectively. The top right inset is a magnified image of the sample mount. (d) A fiber coupled device immersed in liquid helium. The fiber provides optical access to the device while the SMA connectors are required for biasing and readout of sources/detectors. Inset shows one of our fiber coupled sources.

a fiber coupled device immersed in liquid helium. The fiber provides optical access to the device while the SMA connectors are required for biasing and readout of sources/detectors.

Bibliography

[1] A. Gorin, A. Jaouad, E. Grondin, V. Aimez, and P. Charette. Fabrication of silicon nitride waveguides for visible-light using pecvd: a study of the effect of plasma frequency on optical properties. *Opt. Express*, 16(18):13509–13516, 2008.

[2] Franz. Laermer and Andrea. Schilp. Method of anisotropically etching silicon. United States Patent 5501893, 1996.

[3] S.N. Dorenbos, R.W. Heeres, E.F.C Driessen, and V. Zwiller. Efficient and robust fiber coupling of superconducting single photon detectors. *arXiv:1109.5809*, 2011.

Chapter 4

<100> InP Nanowires p-n junction: High Yield Growth and Optoelectronic Characterization

A. Cavalli, J. Wang, I. Esmaeil Zadeh, M. A. Verheijen, D. Wolf, M. E. Reimer, M. Soini, S.R. Plissard, V. Zwiller, J. E.M. Haverkort and E. P. A. M. Bakkers [1]

Semiconductor nanowires are nanoscale structures holding promise in many fields such as optoelectronics, thermoelectrics, and quantum computing. Nanowires are usually grown vertically on (111)-oriented substrates, while (100) is the standard in semiconductor technology. The ability to grow and to control impurity doping of <100> nanowires is crucial for integration. Here, we discuss doping of single-crystalline <100> nanowires, and the structural and optoelectronic properties of p-n junctions based on <100> InP nanowires. We describe a novel approach to achieve low resistance electrical contacts to nanowires via a gradual interface based on p-doped InAsP. As a first demonstration in optoelectronic devices we realize a single nanowire light emitting diode in a <100>-oriented InP nanowire p-n junction. To obtain high vertical yield, necessary for future applications, we investigate the effect of the introduction of dopants on the nanowire growth.

4.1 Introduction

III-V nanowires (NW) have been shown to provide an ideal platform for the development of nanoscale devices and applications, for example for quantum computing, energy conversion, and LEDs[1–6]. Nanowires can be grown in a diverse range of crystalline directions on a

[1]The results in this chapter have been published in Nano Letters 2016 16 (5), 3071-3077

wide assortment of substrates with different crystal orientations[7,8]. The most common NW growth direction is <111>[9–11]; however, in the electronics industry, the (100) crystal orientation is the technology standard. <100> NWs would thus be the best match for present semiconductor fabrication and processing, allowing straightforward integration[12]. A lot of effort has been put in controlling crystal phases in <111> NWs, which remains challenging[13–15]. Undoped <100> InP NWs, in contrast, always exhibit the pure zincblende (ZB) crystalline structure[16–20]. Up to now, however, devices based on defect-free <100> nanowires have not been demonstrated due to the fact that intentional impurity doping of single-crystal <100> NWs has not been realized yet. Impurity doping of semiconductors is essential for the functionality of optoelectronic devices[21,22]. In a recent investigation, Au-catalyzed undoped <100> InP NW arrays with high vertical yield, was obtained by catalyst engineering[23]. In this report, we study the structural and optoelectronic properties of InP <100> NW-based p-n junctions, and investigate the effect of the introduction of dopants during nanowire growth.

We use (100) InP substrates for nanowire growth. Au droplets act as the catalysts for the vapor-liquid-solid (VLS)[24] growth process, while diethyl-zinc (DEZn) and hydrogen sulfide (H_2S) are used as p- and n- dopant precursors during NW growth. The growth was performed using a Zn-doped substrate. We introduced the DEZn after 1 min of growth and continued for 8 min. Subsequently, we switched off the p-dopant and introduced H_2S, growing for 13 min. In order to check the possible effect of dopants on the crystalline quality of the NW[25–27], we studied p-n junctions based on <100> InP wires by transmission electron microscopy (TEM). Wires grown in the <111> direction usually show twin planes, and addition of dopants can completely switch the crystal structure from cubic (for Zn) to hexagonal (for S). In contrast, the NW shown in Fig. 4.1(a) has a pure crystal structure without planar defects and flat 100 side facets. In fact, these <100> InP wires have at most only a few stacking faults per nanowire, always close to the NW base. These defects are stacking faults of 111 planes. A single stacking fault will introduce a kink in the growth direction of the wire. A pair of stacking faults, as observed most frequently, will leave the growth direction unaltered. These defects are introduced during nucleation when the catalyst particle is still evolving towards its equilibrium shape, as has also been discussed in a previous work[23]. Most of the wires and, importantly, also the region of the p-n junction is completely free of defects. The High-Resolution TEM (HRTEM) image in Fig. 4.1(b) demonstrates the zincblende crystalline structure and confirms the <100> growth direction. Fig. 4.1(c) and Fig. 4.1(d) showes HR-TEM image from the highlighted segments of panel (a), demonstrating the pure zincblende crystalline structure of the NW both for p- and n-doped <100> InP nanowires. Scale-bars are 5nm. In <100> nanowires, growth proceeds by nucleation of 100 rather than 111 layers, as in <111> grown nanowires, where the position of the p-n junction is easily recognized by a transition of the crystal phase from zincblende to wurtzite[28]. A change in stacking sequence from cubic (ABC) to hexagonal would imply the introduction of a WZ layer at an angle of 71° with the original growth direction, making this crystal phase transition unlikely. As a result, in <100> NW growth, the crystal structure is defect-free ZB for both p- and n- doping.

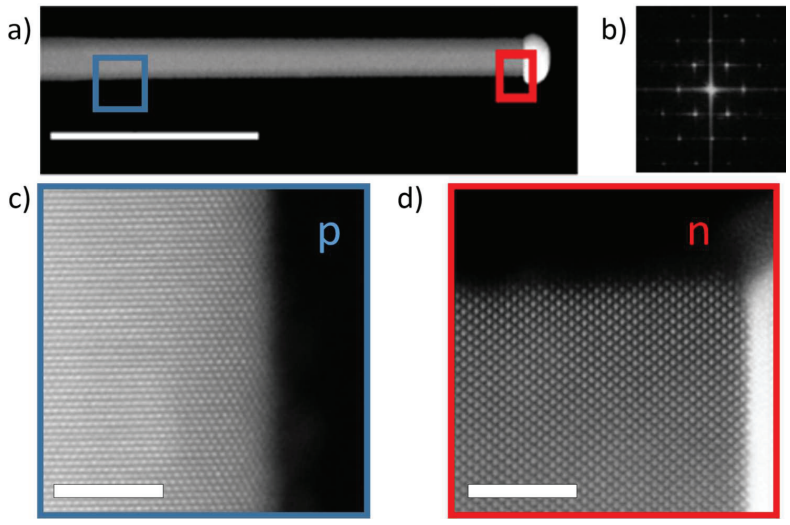

Figure 4.1 | Structural analysis of a <100> p-n junction NW, (a) HAADF TEM image showing an overview image of a p-n doped <100> InP NW. Scale-bar is 500nm. (b) Corresponding FFT image of the NW in panel (a). (c-d) HR-TEM image from the highlighted segments of panel (a), demonstrating the pure zincblende crystalline structure of the NW both for p- and n-doped <100> InP nanowires. Scale-bars are 5nm.

4.2 Measurements and results

After structural characterization, we addressed the electronic properties of doped <100> NWs. To characterize the electrical properties, nanowires were dispersed on a Si/SiO_2 (280 nm) substrate, and four metal contacts were deposited on single nanowires by electron beam lithography (EBL) and metal evaporation. The layers thicknesses are 110 nm Ti/10 nm Au for n-doped nanowires, 1 nm Ti/40 nm Zn/60 nm Au for p-doped nanowires.

In order to remove the native oxide, nanowire surfaces were etched using a buffered hydrogen fluoride (BHF) solution before metal evaporation. Annealing did not improve the performance of the test devices, thus no annealing has been performed. Nanowires were tested in a probe station by sweeping the voltage and measuring the current to obtain I-V curves.

The resistance of n-doped NWs, obtained by 4-point measurements with Ti/Au metal contacts, is in the range of a few $k\Omega$. This behavior is expected, as Ti/Au contacts have been extensively used for characterization of n-doped InP NWs[29]. In the case of p-doped NWs we used Ti/Zn/Au contacts, which resulted in non-linear I-V curves. The resistance was measured in the linear region of the I-V curve to be several tens of $M\Omega$ (typically 50 $M\Omega$).

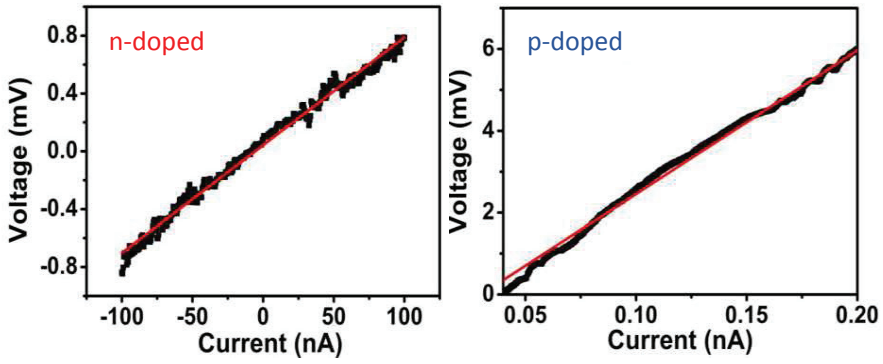

Figure 4.2 | Four point characterization of single n- and p- doped nanowires.

Examples of the resistance measurements are shown in Fig. 4.2. We attribute this high resistance to the formation of Schottky contacts at the metal-semiconductor nanowire interface, resulting in a potential barrier, which gives rise to the poor electrical contact. Obtaining a low resistive electric contact directly to a single p-doped InP NW has previously proven to be a very challenging task[30,31]. In most cases Zn-based metallization is necessary[32,33], making processing unsuitable for most cleanrooms based on III-V materials or silicon. Furthermore, annealing is often required[34], adding complexity to the structure and to the processing.

In order to avoid these drawbacks, we developed a contact area that consists of an axial extension of the p-doped InP with p-doped $InAs_xP_{1-x}$, where the As content is increased gradually in a continuous linear progression. Ohmic contacts can be established on p-doped InAs[35]. Fig. 4.2(a) represents a TEM image of <100> nanowire with gradual interface on top, with arrow depicting growth direction, scale-bar is 1µm. In the top segment of the nanowires (Fig. 4.2(b)), we measured, by Energy Dispersive X-Ray spectroscopy (EDS), a fraction of As in the NW increasing from 0 up to 0.56 ± 0.06 shown in Fig. 4.2(c), in good accordance to the molar flows used. We evaluated the crystalline structure of the NW by TEM measurements. The growth direction switches from <100> to <111> during the transition from InP to InAsP. The <111> growth direction can be expected to be favored for InAsP NWs unless a careful optimization of growth parameters is accomplished. Here, the InAsP segment is used only as a contact segment, and not as an active part of the nanowire devices. Due to the challenges in growing a gradual interface on both the bottom and top of a p-doped NW, thus, we evaluated the performance of the gradual interface only in p-n junctions by measuring I-V characteristics. We grew the NWs in an n-InP / p-InP / p-InAsP growth sequence. To remove InP non-catalyzed vapor-solid growth, which results in growth of low material quality on the nanowire side facets[36], we introduced during growth in-situ HCl with a molar fraction of 1.8×10^{-5}. No HCl, though, was used during the InAsP growth, resulting in a shell that had to be removed after growth.

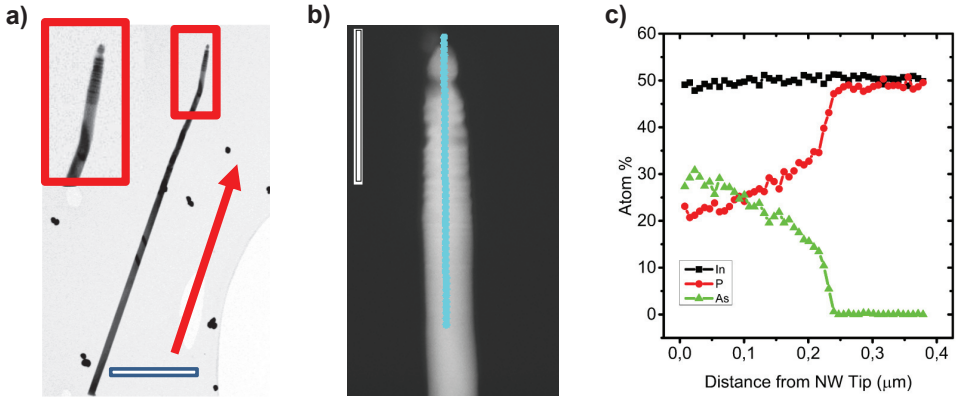

Figure 4.3 | Analysis of the p-doped region with gradual interface,(a) TEM image of <100> nanowire with gradual interface on top, with arrow depicting growth direction. Scale-bar is 1μm. Inset is a zoom-in of the red highlighted region, on which EDX is performed. (b) HAADF TEM image of the region highlighted in panel (a), with line-scan highlighted. Scale-bar is 200nm. (c) EDX line-scan performed parallel to the nanowire growth axis, showing the gradual increase in As content closer to the nanowire tip.

For the electrical measurements we fabricated the metal contacts by two separate steps of electron beam lithography and metal evaporation. A typical measurement is shown in Fig. 4.4(a). No saturation of the current was observed at the our range of voltages and currents (up to 15 V and 2.5 μA, which results in a current density in the order of $10^4\ A/cm2$). The compliance level of the equipment is 0.02 nA, resulting in a flat current below the threshold voltage. The rectification ratio (measured in the range of $\pm 5\ V$) is typically 10^2. We estimated a total series resistance in the device of $1\ M\Omega$, which is an improvement of 2 orders of magnitude compared to previous devices.

We tested the optoelectronic properties of the NW light emitting diode by electroluminescence, measuring the emission spectrum as a function of the injection current. A waterfall plot of typical electroluminescence (EL) spectra as a function of injection current from a single NW is presented in Fig. 4.4(b). Two prominent peaks (at 1.38 eV and at 1.33 eV) with different characteristics can be identified, Fig. 4.4(c). The peak at higher energy, assigned to the InP nanowire band gap, increases in intensity and blue-shifts with larger current. We attribute this behavior to state filling of higher energy states with increased injection current. The energy position peak at 1.33 eV does not change with current, indicating an impurity-related emission, which saturates at high injection current, Fig. 4.4(d). In comparison with p-n junctions based on <111> InP NWs without gradual interface[29,37], measured at similar injection currents, the nanowires presented in this work show an order of magnitude stronger peak intensity and narrower peak line-width (a factor of 2). The quantum efficiency at low temperatures is estimated to be 0.1%, further indicating an improvement with respect

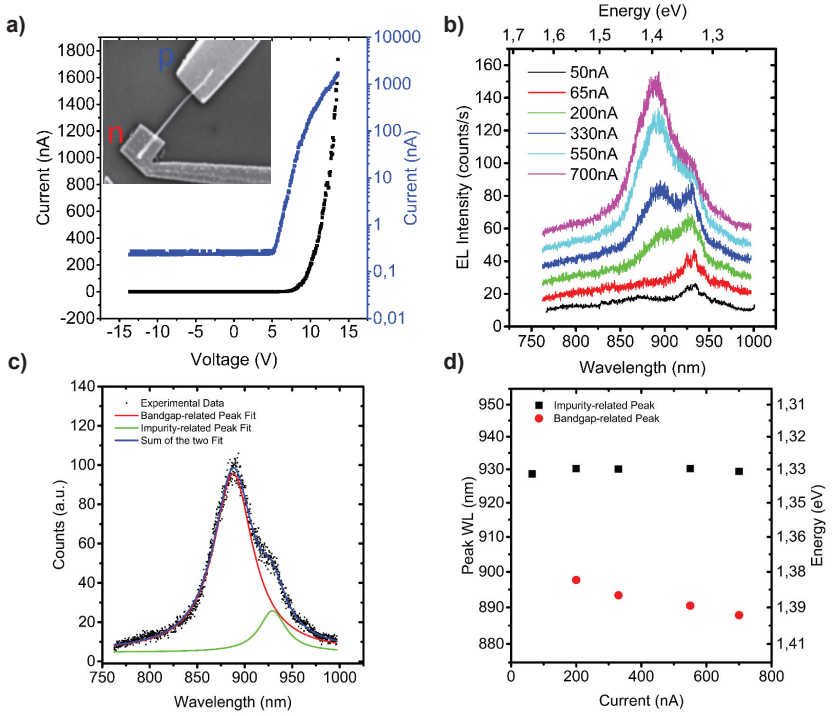

Figure 4.4 | Optoelectronic characterization of p-n junctions based on <100> InP NW with gradual interface., (a) Scheme of the geometry of n-InP / p-InP / p-InAsP <100> NW with gradual interface. (b) I-V characterization at 4K of single <100> InP NW p-n junction with the previously described geometry, with current showed in linear and logarithmic scale. Inset: SEM image of device used for NW optoelectronic characterization. (c) Electroluminescence (EL) of single <100> InP NW p-n junction with gradual interface at 4K as a function of injection current. EL spectra are offset for clarity. (d) Electroluminescence spectrum and the two Lorentzian components, related to the different peaks, used to fit. (e) Dependence on injected current of the center peak wavelength for each peak.

to previously reported devices[29].

4.3 conclusion

Low resistive contact to p-doped InP has been realized by developing a novel p-InP/p-InAsP gradual interface in NW. We have demonstrated the first p-n junction based on <100>-oriented nanowires and tested its optoelectronic properties in a single nanowire device.

<100> nanowires show great potential for next-generation applications integrated with the current semiconductor technology.

Bibliography

[1] X. Duan and Y. Huang; Y. Cui; J. Wang ; C. M. Lieber. Indium phosphide nanowires as building blocks for nanoscale electronic and optoelectronic devices. *Nature*, 409:66—-69, 2001.

[2] V. Mourik, K. Zuo, S. M. Frolov, S. R. Plissard, E. P. a. M. Bakkers, and L. P. Kouwenhoven. Signatures of majorana fermions in hybrid superconductor-semiconductor nanowire devices. *Science*, 336:1003—-1007, 2012.

[3] A. I. Hochbaum and P. Yang. Semiconductor nanowires for energy conversion. *Chem. Rev.*, 110:527––546, 2010.

[4] Y. J. Doh, J. a. van Dam, A. L. Roest ; E. P. a M. Bakkers, L. P. Kouwenhoven, and S. De Franceschi. Tunable supercurrent through semiconductor nanowires. *Science*, 309:272—-275, 2005.

[5] B. Tian, X. Zheng, T. J. Kempa, Y. Fang, N. Yu, G. Yu, J. Huang, and C. M. Lieber. Coaxial silicon nanowires as solar cells and nanoelectronic power sources. *Nature*, 449:885—-889, 2007.

[6] X. Duan, Y. Huang, R. Agarwal, and C. M. Lieber. Single-nanowire electrically driven lasers. *Nature*, 421:241—-245, 2003.

[7] S. a. Fortuna and X. Li. Metal-catalyzed semiconductor nanowires: A review on the control of growth directions. *Semicond. Sci. Technol*, 25:024005, 2010.

[8] A. Stekolnikov, J. Furthmüller, and F. Bechstedt. Absolute surface energies of group-iv semiconductors: Dependence on orientation and reconstruction. *Phys. Rev. B*, 65:115318, 2002.

[9] W. Seifert, M. Borgström, K. Deppert, K. A. Dick, J. Johansson, M. W. Larsson, T. Mårtensson, N. Skold, C. P. T. Svensson, B. A. Wacaser, and et al. Growth of one-dimensional nanostructures in movpe. *J. Cryst. Growth*, 272:211—-220, 2004.

[10] S. Assali, I. Zardo, S. Plissard, D. Kriegner, M. A. Verheijen, G. Bauer, A. Meijerink, A. Belabbes, F. Bechstedt, J. E. M. Haverkort, and et al. Direct band gap wurtzite gallium phosphide nanowires. *Nano Lett.*, 13:1559—-1563, 2013.

[11] K. Tomioka, M. Yoshimura, and T. Fukui. A iii–v nanowire channel on silicon for high-performance vertical transistors. *Nature*, 488:189–192, 2012.

[12] M. Borg, H. Schmid, K. E. Moselund, G. Signorello, L. Gignac, J. Bruley, C. Breslin, P. Das Kanungo, P. Werner, and H. Riel. Vertical iii-v nanowire device integration on si(100). *Nano Lett.*, 14:1914––1920, 2014.

[13] D. Dalacu, K. Mnaymneh, J. Lapointe, X. Wu, P. J. Poole, G. Bulgarini, V. Zwiller, and M. E. Reimer. Ultraclean emission from inasp quantum dots in defect-free wurtzite inp nanowires. *Nano Lett.*, 12:5919—-5923, 2012.

[14] Q. Gao, D. Saxena, F. Wang, L. Fu, S. Mokkapati, Y. Guo, L. Li, J. Wong-Leung, P. Caroff, H. H. Tan, and et al. Selective-area epitaxy of pure wurtzite inp nanowires: High quantum efficiency and room-temperature lasing. *Nano Lett.*, 14:5206—-5211, 2014.

[15] S. Lehmann, J. Wallentin, D. Jacobsson, K. Deppert, and K. A. Dick. A general approach for sharp crystal phase switching in inas, gaas, inp, and gap nanowires using only group v flow. *Nano Lett.*, 13:4099—-4105, 2013.

[16] M. T. Björk, B. J. Ohlsson, T. Sass, A. I. Persson, C. Thelander, M. H. Magnusson, K. Deppert, and L. Wallenberg, L. R.; Samuelson. One-dimensional heterostructures in semiconductor nanowhiskers. *Appl. Phys. Lett.*, 80:1058––1060, 2002.

[17] U. Krishnamachari, M. Borgstrom, B. J. Ohlsson, N. Panev, L. Samuelson, W. Seifert, M. W. Larsson, and L. R. Wallenberg. Defect-free inp nanowires grown in [001] direction on inp (001). *Appl. Phys. Lett.*, 85:2077—-2079, 2004.

[18] Z. A. Li, C. Möller, V. Migunov, M. Spasova, M. Farle, A. Lysov, C. Gutsche, I. Regolin, W. Prost, F. J. Tegude, and et al. Planar-defect characteristics and cross-sections of <001>, <111>, and <112> inas nanowires. *J. Appl. Phys.*, 109:114320, 2011.

[19] J. Wang, S. Plissard, M. Hocevar, T. T. T. Vu, T. Zehender, G. G. W. Immink, M. A. Verheijen, J. Haverkort, and E. P. A. M. Bakkers. Position-controlled [100] inp nanowire arrays. *Appl. Phys. Lett.*, 100:053107, 2012.

[20] H. A. Fonseka, P. Caroff, J. Wong-Leung, A. S. Ameruddin, H. H. Tan, and C. Jagadish. Nanowires grown on inp (100): Growth directions, facets, crystal structures, and relative yield control. *ACS Nano*, 8:6945—-6954, 2014.

[21] M. T. Borgström, J. Wallentin, M. Heurlin, S. Fält, P. Wickert, J. Leene, M. H. Magnusson, K. Deppert, and L. Samuelson. Nanowires with promise for photovoltaics. *IEEE J. Sel. Top. Quantum Electron*, 17:1050––1061, 2011.

[22] J. Wallentin and M. T. Borgström. Doping of semiconductor nanowires. *J. Mater. Res.*, 26:2142—-2156, 2011.

[23] J. Wang, S. R. Plissard, M. a. Verheijen, L. F. Feiner, A. Cavalli, and E. P. a M. Bakkers. Reversible switching of inp nanowire growth direction by catalyst engineering. *Nano Lett.*, 13:3802–3806, 2013.

[24] R. S. Wagner and W. C. Ellis. Vapor-liquid-solid mechanism of single crystal growth. *Appl. Phys. Lett.*, 4:89––90, 1964.

[25] R. E. Algra, M. A. Verheijen, M. T. Borgström, L.-F. Feiner, G. Immink, W. J. P. van Enckevort, E. Vlieg, and E. P. A. M. Bakkers. Twinning superlattices in indium phosphide nanowires. *Nature*, 456:369—-372, 2008.

[26] M. T. Borgström, E. Norberg, P. Wickert, H. A. Nilsson, J. Trägårdh, K. A. Dick, G. Statkute, P. Ramvall, K. Deppert, and L. Samuelson. Precursor evaluation for in situ inp nanowire doping. *Nanotechnology*, 19:445602, 2008.

[27] J. Wallentin, Ek. M. Mergenthaler, L. R. Wallenberg, L. Samuelson, K. Deppert, M. E. Pistol, and M. T. Borgström. Probing the wurtzite conduction band structure using state filling in highly doped inp nanowires. *Nano Lett.*, 11:2286—-2290, 2011.

[28] Y. Cui, J. Wang, S. R. Plissard, A. Cavalli, T. T. T. Vu, R. P. J. Van Veldhoven, L. Gao, M. Trainor, M. a. Verheijen, and J. E. M. Haverkort; et al. Efficiency enhancement of inp nanowire solar cells by surface cleaning. *Nano Lett.*, 13:4113–4117, 2013.

[29] E. D. Minot, F. Kelkensberg, M. Van Kouwen, J. A. Van Dam, L. P. Kouwenhoven, V. Zwiller, M. T. Borgström, O. Wunnicke, M. A. Verheijen, and E. P. A. M. Bakkers. Single quantum dot nanowire leds. *Nano Lett.*, 7:367––371, 2007.

[30] J. H. Perkins, M. F. O. O'Keefe, R. E. Miles, and C. M. Snowden. Pt and zn based ohmic contacts to p-type inp. pages 190––193, 1994.

[31] S. Hwang, J. Shim, and Y. Eo. Ohmic contacts of pd/zn/pt(or pd)/au materials to p-type inp. pages 260—-262, 2005.

[32] K. Tabatabaie-Alavi, A.N.M.M. Choudhury, N.J. Gabriel, and C.G. Fonstad. Low resistance ohmic contact, November 8 1983. US Patent 4,414,076.

[33] S. Nakahara, P. K. Gallagher, E. C. Felder, and R. B. Lawry. Interaction between zinc metallization and indium phosphide. *Solid. State. Electron.*, 27:557—-564, 1984.

[34] Kefeng. Zhang, Hengjing. Tang, Xiaoli. Wu, Jintong. Xu, Xue. Li, and Haimei. Gong. Improved au/zn/au ohmic contacts for p-type inp. volume 6621, pages 662118–662118–7, 2007.

[35] E. M. Lysczek, J. A. Robinson, and S. E. Mohney. Ohmic contacts to p-type inas. *Mater. Sci. Eng. B*, 134:44—-48, 2006.

[36] M. T. Borgström, J. Wallentin, J. Trägårdh, P. Ramvall, M. Ek, L. R. Wallenberg, L. Samuelson, and K. Deppert. In situ etching for total control over axial and radial nanowire growth. *Nano Res.*, 3:1–7, 2010.

[37] M. E. Reimer, M. P. van Kouwen, M. Barkelid, M. Hocevar, M. H. M. van Weert, R. E. Algra, E. P. A. M. Bakkers, M. T. Bjork, H. Schmid, H. Riel, and et al. Single photon emission and detection at the nanoscale utilizing semiconductor nanowires. *J. Nanophotonics*, 5:11, 2010.

Chapter 5

Controlling the exciton energy of a nanowire quantum dot by strain fields

Y. Chen, I. Esmaeil Zadeh, K. D. Jöns, J. Zhang, M. E. Reimer, D. Dalacu, P. J. Poole, F. Ding, V. Zwiller, and O. G. Schmidt [1]

In this chapter, we present an experimental route to engineer the exciton energies of single quantum dots in nanowires. By integrating the nanowires onto a piezoelectric crystal, we controllably apply strain fields to the nanowire quantum dots. Consequently, the exciton energy of a single quantum dot in the nanowire is shifted by ~ 3 meV without degrading its optical intensity and single-photon purity. Second-order autocorrelation measurements are performed at different strain fields on the same nanowire quantum dot. The suppressed multi-photon events at zero time delay clearly verify that the quantum nature of single-photon emission is well preserved under external strain fields. The work presented here could facilitate on-chip optical quantum information processing with nanowire based single photon emitters.

5.1 Introduction

Quantum optical information processing has imposed several key requirements on a good single-photon emitter. First, the emitter should generate single-photons with high brightness and long coherence time. Second, the emitted photons from one source, and much more preferred from independent sources, should be indistinguishable [1–5]. Semiconductor quantum dots (QDs) embedded in bottom-up grown nanowires have the potential to fulfill these prerequisites [6,7]. For the first requirement, these wires benefit from the recently developed two step growth process combining selective-area and vapor-liquid-solid epitaxy

[1] The results in this chapter have been published in Applied Physics Letters, 108,182103 (2016)

techniques. A single QD can be ideally embedded into the nanowire, which overcomes previous random approaches of fabricating waveguides around multiple QDs[8–10]. Bright single photon sources based on similar nanowires with extraction efficiencies of up to 42% have been demonstrated[11]. A further improved extraction efficiency exceeding 90% can be achieved if the wire shape is smoothly tapered and a thin dielectric-gold mirror is integrated underneath[12]. The nanowire also features a Gaussian emission profile, which is important for fiber coupling[13–15]. The significant reduction of nearby traps also provides an ultraclean spectrum and long coherence times of up to 1.2 ns[16,17].

For the second requirement; however, the nanowire QDs suffer from inhomogeneous spectral broadening of the exciton emission from different sources due to shape, strain and composition inhomogeneity during growth[7,10]. Therefore, the single photons from different sources are distinguishable and scaling up these sources is extremely challenging[18]. Post-growth tuning is therefore essential in order to achieve indistinguishable photons from independent sources. Tuning the exciton emission from nanowire QDs will also find important applications in a hybrid system, where the QDs can be coupled to an atomic system either to counteract slow spectral diffusion in QDs or to store photons in a quantum memory[19].

To date, the methods for engineering the nanowire QD emission are limited. G. Signorello et al. clamped a freestanding nanowire by a Ti contact onto a flexible substrate[21]. By bending the nanowire, they shifted the photoluminescence (PL) signal from $GaAs - Al_{0.3}Ga_{0.7}As - GaAs$ core/shell nanowires by over 290 meV. However, on-chip implementation of such a "bending wire" setup is quite challenging, and the core/shell nanowires by their nature are not single-photon sources. P. Kremer et al. fabricated QD-containing nanowires on a piezo substrate by reactive ion etching and managed to tune the QD exciton emission over 1.2 meV by strain[22]. In addition to the fabrication challenges such as rough nanowire surfaces and shape control, the top-down fabrication approach generally has a low yield since the QD locations are not deterministically aligned during the etching. M. Reimer et al. have successfully removed the biexciton binding energy in nanowire quantum dots by a local lateral electric field. Unfortunately, in this configuration the in-plane emission is blocked by electrical contacts at both ends of the nanowire to pump away excess charges[23,24], and is therefore not desirable for on-chip quantum information processing.

5.2 Masurement setup and the experiment

In this chapter we demonstrate wavelength-tunable single photon sources from nanowire QDs by strain. The studied sample is a single InAsP QD embedded in a bottom-up grown InP nanowire waveguide. The nanowire shape can be modified during growth to control the tapering angle, diameter and length (inset in Fig. 5.1(a)). Detailed information on the growth are discussed elsewhere[13]. The tapered nanowires were picked-up from the growth substrate by a nano-manipulator and transferred subsequently onto a piezoelectric crystal

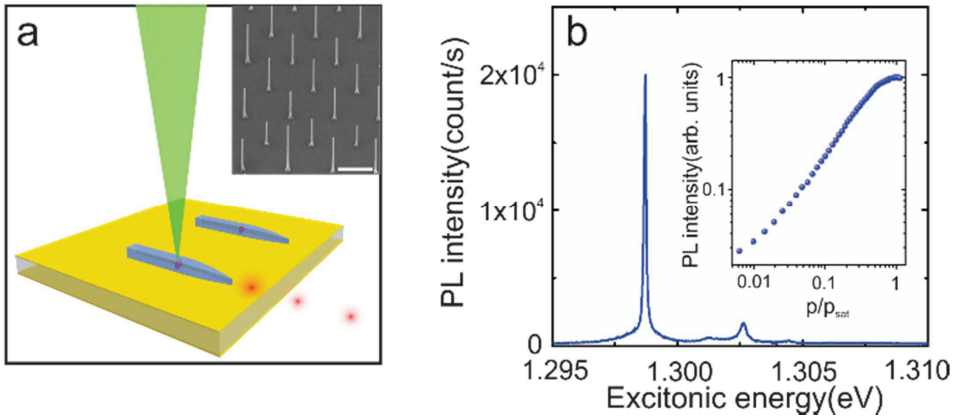

Figure 5.1 | Sketch of the strain-tunable nanowire single- photon emitter. (a) sketch of the device. The nanowire is laid in-plane on the piezo substrate. Inset the Scanning Electron Microscopy of the nanowires before the transfer. Scale bar indicates 2 um. (b) The spectrum of the nanowire quantum dot. Inset shows the dependence of the integrated peak intensity of emission line on the excitation power.

consisting of $[Pb(Mg_{1/3}Nb_{2/3})O_3]_{0.72}[PbTiO_3]_{0.28}$ (PMN-PT) (Fig. 5.1(a)). The choice of PMN-PT is due to its large in-plane strain capabilities and negligible drop of strain at low temperatures[25].

The device is mounted on the cold-finger of a continuous helium-flow cryostat and all of the optical experiments are carried out at 5 K. A continuous-wave laser at wavelength of 532 nm is focused onto the nanowire by an objective with numerical aperture of 0.42. The radiative dipole of a single nanowire QD lies in a plane perpendicular to the nanowire elongation axis, therefore the excitation and collection of the photoluminescence (PL) can be done either along the nanowire elongation axis or from the top of the nanowire (perpendicular to the axis). With both excitation/collection geometries, the peak emissions have exactly the same energies[26]. In this work we used the geometry as sketched in Fig. 5.1(a) to demonstrate the strain tuning of nanowire emissions. For on-chip integration applications, however, the in-plane emission along the axis can be used together with dielectric waveguides to obtain much higher photon flux[27].

5.3 Results

Fig. 5.1(b) shows a typical PL spectrum from a single nanowire QD. The integrated intensity of the main emission line has a linear dependence on the laser excitation power (see inset of Fig. 5.1(b)) and its fine structure splitting[28] is $\sim 5\,\mu eV$. We attribute this line to neutral

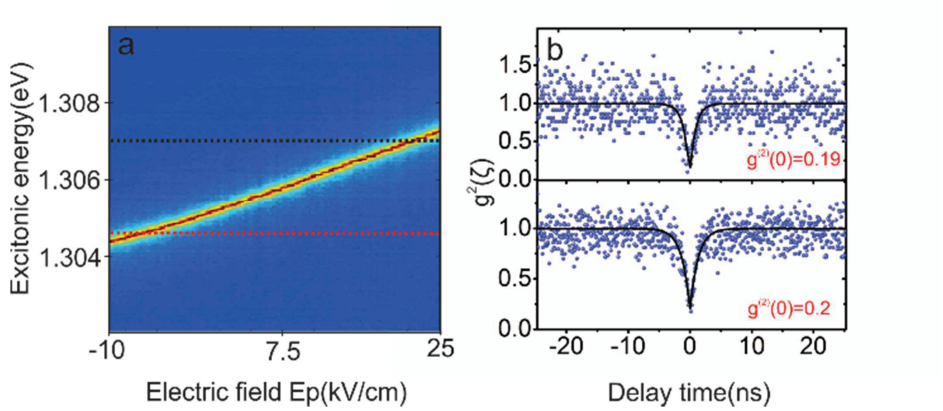

Figure 5.2 | Strain tuning behavior of the PL from nanowire quantum dots and normalized second-order autocorrelation function of the single-photon source without background subtraction. (a) PL from the sandwiched nanowire. By sweeping the voltage on piezo, the excitonic energy is linearly and reversibly shifted by around 3 meV. (b) Autocorrelation measurement of the emission from a nanowire quantum dot at two energy points indicated by the black and red dashed lines in the left figure.

exciton emission.

A bias voltage V applied to the PMN-PT results in an out-of-plane electric field Ep, leading to an in-plane strain in the nanowires that modifies the QD emission energy[25,29,30]. The PL emission spectrum is recorded while sweeping the voltage applied to the piezoelectric substrate. Fig. 5.2(a) shows the typical result for the strain tuning of a single nanowire QD. We observe a clear blue shift of the QD emission when increasing the electric field E_p, This is because for this device increasing the electric field corresponds to compressive strain and therefore increases the emission energy. Both blue and red shifts can be achieved with our device, simply by changing the polarity of the applied voltages. Two types of devices were used to study the efficiency of strain transfer. In the first type of devices the nanowires were anchored by a thin silicon nitride layer to achieve more efficient strain transfer. In the second type of devices without anchoring layers, the nanowires were transferred directly onto the PMN-PT substrate. We observed that the emission energy tuning can be achieved with the same order of magnitude in these two types of devices. We ascribe the shift in the devices without anchoring layers to the interlayer van der Waals forces between nanowires and the substrate, as being observed in 2D material heterojunctions[31]. This finding will greatly simplify the fabrication processes for future devices where in-plane single-photon emitters are needed.

To demonstrate wavelength-tunable single-photon emission from nanowire QDs, we have measured the second-order autocorrelation functions[32] $g^2(\tau)$ as E_p is varied from -10 to

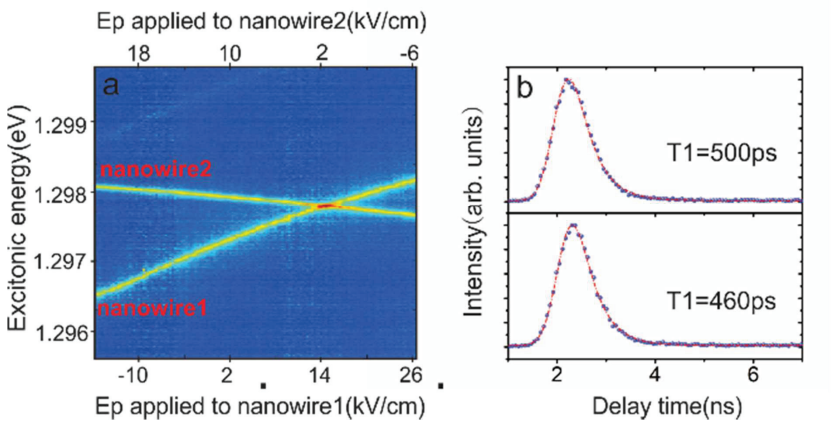

Figure 5.3 | Two nanowire quantum dots are tuned to degeneracy. (a) Emission energy from two nanowires tuned into degeneracy. (b) The lifetime of two nanowire quantum dots emission at the crossing point, with 500 ps and 460 ps, respectively. Blue dots indicates experimental data and red short dashed line is the fitting line

25 kV/cm. After spectral filtering with a spectrometer, a non-polarizing 50:50 beam splitter splits the exciton emission between two single-photon avalanche detectors. Fig. 5.2(b) shows the measured $g^2(\tau)$ for two different strain fields corresponding to dissimilar emission energies. At the exciton energy of 1.307 eV, a multiphoton emission probability of $g^2(0) = 0.19 \pm 0.08$ is obtained by fitting the experimental data. When the exciton energy is shifted by 2 meV, the $g^2(0)$ remains unchanged within experimental error, with a value of 0.20 ± 0.06 (solid line in Fig. 5.2(b), no background subtraction in both cases). The non-vanishing $g^2(0)$ is most likely due to stray light from background emission, the dark counts and limited timing resolution of our single-photon detectors.

We can also tune the QD energies from different nanowires into spectral resonance. For this purpose, we transfer two nanowire QDs onto two separate chips. The results are shown in Fig. 5.3(a). For the applied electric fields of 2 kV/cm and 14 kV/cm, the emission energies of two QDs are tuned to the same value. This strain tuning technique of the emission energy that we present opens up a scalable route to realize two-photon interference between two spatially separated nanowire single-photon sources. It is worth mentioning that the lifetime T_1 for two nanowire QDs measured at degeneracy are quite short and similar to each other (see Fig. 5.3(b)), which is advantageous for future two-photon interference experiments. When lying on the substrate, the nanowire QDs are in close proximity to the gold surface of the PMN-PT substrate. It is commonly believed that the exchange of energy between a dipole and the metal surface plasmon can provide additional decay channels, leading to a faster decay trace (lifetime)[33,34]. Compared to the lifetime of about 1.5 ns reported for similar

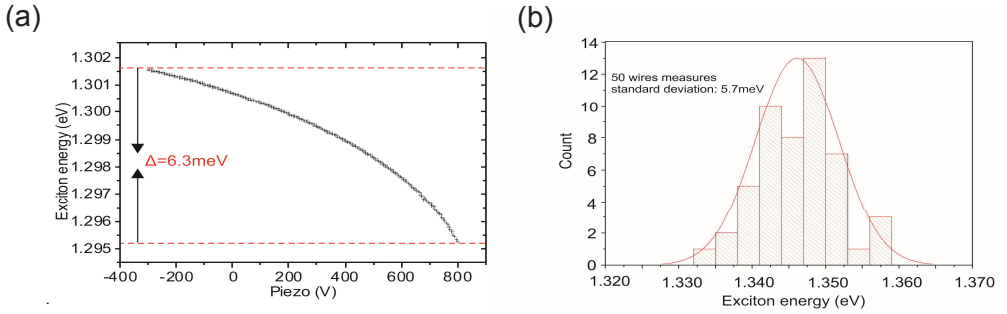

Figure 5.4 | Nanowire tuning and energy spread over the entire wafer. (a) Exciton emission energy of a single nanowire QD is shifted by 6.3 meV. (b) Inhomogeneous spectral broadening of 50 nanowire QDs from another growth run with different emission energies. The red envelope is a Gaussian fit, with a standard deviation of 5.7 meV.

nanowire QDs[17], the lifetime measured here is approximately three times shorter, which is likely due to this plasmonic enhancement[35]. On the other hand the possible plasmonic effect, if not required, can be avoided by putting a thick dielectric layer under the nanowires or by embedding the nanowire inside a dielectric waveguide.

Finally, we would like to address the question of what is the percentage of these wires that can be tuned into spectral resonance. We compare the emission tuning range of single nanowire QDs with the inhomogeneous emission broadening of 50 nanowire QDs. The strain tuning range of a single nanowire QD is shown in Fig. 5.4(a). By applying voltage from -300 V to 800 V to the PMN-PT, the exciton emission energy is shifted by 6.3 meV. The non-linear tuning behavior is most likely due to the imperfect anchoring of the nanowire. We measured 50 QDs from another growth run with different emission energies to determine the inhomogeneous spectral broadening. The distribution of their emission energies is shown in Fig. 5.4(b). The data is fitted by a Gaussian envelope. The standard deviation is 5.7 meV, which is smaller than the strain tuning range. This result suggests that we can tune almost any nanowire into spectral resonance with another one from the same wafer.

5.4 conclusion

In summary, we have demonstrated wavelength-tunable single photon sources from nanowire quantum dots by using strain engineering techniques. Due to several important advantages, the tapered nanowires grown in a bottom-up approach are ideal single-photon sources for on-chip quantum photonic applications when laid down on the substrate. With the strain tuning method presented in this work, the inhomogeneity of their emission energies can potentially be overcome. As an example, we demonstrate the spectral resonance of

two strain engineered nanowire QDs. Our strain engineering technique is also compatible with the dielectric waveguides with embedded nanowires to facilitate complex routing of indistinguishable single photons. Combined with the recently developed on-chip strain tuning platform with low operation voltages and ultra-small footprints[35], our work may facilitate important quantum optical experiments such as two-photon interference with on-chip integrated nanowire QDs[36].

Bibliography

[1] L. M. Duan, M. D. Lukin, J. I. Cirac, and P. Zoller. Long-distance quantum communication with atomic ensembles and linear optics. *Nature*, 414:413–418, 2001.

[2] Charles. Santori, David. Fattal, Jelena. Vuckovic, Glenn S. Solomon, and Yoshihisa. Yamamoto. Indistinguishable photons from a single-photon device. *Nature*, 419:594–597, 2002.

[3] J. L. O'Brien, G. J. Pryde, A. G. White, T. C. Ralph, and D. Branning. Demonstration of an all-optical quantum controlled-not gate. *Nature*, 426(6964):264–267, 2003.

[4] Edward. B. Flagg, Andreas. Muller, Sergey. V. Polyakov, Alex. Ling, Alan. Migdall, and Glenn. S. Solomon. Interference of single photons from two separate semiconductor quantum dots. *Phys. Rev. Lett.*, 104:137401, 2010.

[5] Axel. Kuhn, Markus. Hennrich, and Gerhard. Rempe. Deterministic single-photon source for distributed quantum networking. *Phys. Rev. Lett.*, 89:067901, 2002.

[6] T. Heindel, C. Schneider, M. Lermer, S. H. Kwon, T. Braun, S. Reitzenstein, S. Höfling, M. Kamp, and A. Forchel. Electrically driven quantum dot-micropillar single photon source with 34% overall efficiency. *Applied Physics Letters*, 96(1), 2010.

[7] I. Friedler, C. Sauvan, J. P. Hugonin, P. Lalanne, J. Claudon, and J. M. Gérard. Solid-state single photon sources: the nanowire antenna. *Opt. Express*, 17(4):2095–2110, 2009.

[8] Julien. Claudon, Joel. Bleuse, Nitin. Singh. Malik, Maela. Bazin, Perine. Jaffrennou, Niels. Gregersen, Christophe. Sauvan, Philippe. Lalanne, and Jean-Michel. Gerard. A highly efficient single-photon source based on a quantum dot in a photonic nanowire. *Nat. Photon.*, 4(3):174–177, 2010.

[9] A. Dousse, L. Lanco, J. Suffczyń ski, E. Semenova, A. Miard, A. Lemaître, I. Sagnes, C. Roblin, J. Bloch, and P. Senellart. Controlled light-matter coupling for a single quantum dot embedded in a pillar microcavity using far-field optical lithography. *Phys. Rev. Lett.*, 101:267404, 2008.

[10] J. Heinrich, A. Huggenberger, T. Heindel, S. Reitzenstein, S. Höfling, L. Worschech, and A. Forchel. Single photon emission from positioned gaas/algaas photonic nanowires. *Applied Physics Letters*, 96(21), 2010.

[11] Michael. E. Reimer, Gabriele. Bulgarini, Nika. Akopian, Moira. Hocevar, Maaike. Bouwes. Bavinck, Marcel. A. Verheijen, Erik. P. A. M. Bakkers, Leo. P. Kouwenhoven, and Val. Zwiller. Bright single-photon sources in bottom-up tailored nanowires. *Nat. Commun.*, 3:737, 2012.

[12] I. Friedler, P. Lalanne, J. P. Hugonin, J. Claudon, J. M. Gérard, A. Beveratos, and I. Robert-Philip. Efficient photonic mirrors for semiconductor nanowires. *Opt. Lett.*, 33(22):2635–2637, 2008.

[13] Gabriele. Bulgarini, Michael. E. Reimer, Maaike. Bouwes. Bavinck, Klaus. D. Jöns, Dan. Dalacu, Philip. J. Poole, Erik. P. A. M. Bakkers, and Val. Zwiller. Nanowire waveguides launching single photons in a gaussian mode for ideal fiber coupling. *Nano Letters*, 14(7):4102–4106, 2014.

[14] Gabriele. Bulgarini, Dan. Dalacu, Philip. J. Poole, Jean. Lapointe, Michael. E. Reimer, and Val. Zwiller. Far field emission profile of pure wurtzite inp nanowires. *Applied Physics Letters*, 105(19), 2014.

[15] Niels. Gregersen, Torben. R. Nielsen, Julien. Claudon, Jean-Michel. Gérard, and Jesper. Mørk. Controlling the emission profile of a nanowire with a conical taper. *Opt. Lett.*, 33(15):1693–1695, 2008.

[16] Dan. Dalacu, Khaled. Mnaymneh, Jean. Lapointe, Xiaohua. Wu, Philip. J. Poole, Gabriele. Bulgarini, Val. Zwiller, and Michael. E. Reimer. Ultraclean emission from inasp quantum dots in defect-free wurtzite inp nanowires. *Nano Letters*, 12(11):5919–5923, 2012.

[17] Michael. E. Reimer, Gabriele. Bulgarini, Reinier. W. Heeres, Barbara. J. Witek, Marijn. AM. Versteegh, Dan. Dalacu, Jean. Lapointe, Philip. J. Poole, and Val. Zwiller. Overcoming power broadening of the quantum dot emission in a pure wurtzite nanowire. *arXiv*, 1407(2833), 2014.

[18] Joël. Bleuse, Julien. Claudon Megan. Creasey, Nitin. S. Malik, Jean-Michel. Gérard, Ivan. Maksymov, Jean-Paul. Hugonin, and Philippe. Lalanne. Inhibition, enhancement, and control of spontaneous emission in photonic nanowires. *Phys. Rev. Lett.*, 106:103601, 2011.

[19] N. Akopian, U. Perinetti, L. Wang, A. Rastelli, O. G. Schmidt, and V. Zwiller. Tuning single gaas quantum dots in resonance with a rubidium vapor. *Applied Physics Letters*, 97(8), 2010.

[20] S. Kumar, R. Trotta, E. Zallo, J. D. Plumhof, P. Atkinson, A. Rastelli, and O. G. Schmidt. Strain-induced tuning of the emission wavelength of high quality gaas/algaas quantum dots in the spectral range of the 87rb d2 lines. *Applied Physics Letters*, 99(16), 2011.

[21] Giorgio. Signorello, Siegfried. Karg, Mikael. T. Björk, Bernd. Gotsmann, and Heike. Riel. Tuning the light emission from gaas nanowires over 290 mev with uniaxial strain. *Nano Letters*, 13(3):917–924, 2013.

[22] P. E. Kremer, A. C. Dada, P. Kumar, Y. Ma, S. Kumar, E. Clarke, and B. D. Gerardot. Strain-tunable quantum dot embedded in a nanowire antenna. *Phys. Rev. B*, 90:201408, 2014.

[23] Maarten. P. van Kouwen, Michael. E. Reimer, Anne. W. Hidma, Maarten. H. M. van Weert, Rienk. E. Algra, Erik. P. A. M. Bakkers, Leo. P. Kouwenhoven, and Val. Zwiller. Single electron charging in optically active nanowire quantum dots. *Nano Letters*, 10(5):1817–1822, 2010.

[24] Michael. E. Reimer, Maarten. P. van Kouwen, Anne. W. Hidma, Maarten. H. M. van Weert, Erik. P. A. M. Bakkers, Leo. P. Kouwenhoven, and Val. Zwiller. Electric field induced removal of the biexciton binding energy in a single quantum dot. *Nano Letters*, 11(2):645–650, 2011.

[25] F. Ding, R. Singh, J. D. Plumhof, T. Zander, V. Křápek, Y. H. Chen, M. Benyoucef, V. Zwiller, K. Dörr, G. Bester, A. Rastelli, and O. G. Schmidt. Tuning the exciton binding energies in single self-assembled $ingaas/gaas$ quantum dots by piezoelectric-induced biaxial stress. *Phys. Rev. Lett.*, 104:067405, 2010.

[26] Gabriele. Bulgarini, Michael. E. Reimer, and Val. Zwiller. Optical polarization properties of a nanowire quantum dot probed along perpendicular orientations. *Applied Physics Letters*, 101(11), 2012.

[27] Iman. Esmaeil Zadeh, Ali. W. Elshaari, Klaus. D. Jöns, Andreas. Fognini, Dan. Dalacu, Philip. J. Poole, Michael. E. Reimer, and Val. Zwiller. Deterministic integration of single photon sources in silicon based photonic circuits. *Nano Letters*, 0(0):null, 0.

[28] V. D. Kulakovskii, G. Bacher, R. Weigand, T. Kümmell, A. Forchel, E. Borovitskaya, K. Leonardi, and D. Hommel. Fine structure of biexciton emission in symmetric and asymmetric cdse/znse single quantum dots. *Phys. Rev. Lett.*, 82:1780–1783, 1999.

[29] J. D. Plumhof, V. Křápek, F. Ding, K. D. Jöns, R. Hafenbrak, P. Klenovský, A. Herklotz, K. Dörr, P.Michler, A. Rastelli, and O. G. Schmidt. Strain-induced anticrossing of bright exciton levels in single self-assembled gaas/al$_x$ga$_{1-x}$as and in$_x$ga$_{1-x}$as/gaas quantum dots. *Phys. Rev. B*, 83:121302, 2011.

[30] Stefan. Seidl, Martin. Kroner, Alexander. Högele, Khaled. Karrai, Richard. J. Warburton, Antonio. Badolato, and Pierre. M. Petroff. Effect of uniaxial stress on excitons in a self-assembled quantum dot. *Applied Physics Letters*, 88(20), 2006.

[31] Georg. S. Duesberg. Heterojunctions in 2d semiconductors: A perfect match. *Nat. Mater.*, 13(12):1075–1076, 2014.

[32] R. Hanbury. Brown and R. Q. Twiss. A test of a new type of stellar interferometer on sirius. *Nature*, 178:1046–1048, 1956.

[33] Koichi. Okamoto, Isamu. Niki, Axel. Scherer, Yukio. Narukawa, Takashi. Mukai, and Yoichi. Kawakami. Surface plasmon enhanced spontaneous emission rate of ingan/gan quantum wells probed by time-resolved photoluminescence spectroscopy. *Applied Physics Letters*, 87(7), 2005.

[34] Kwang. Jun Ahn and Andreas. Knorr. Radiative lifetime of quantum confined excitons near interfaces. *Phys. Rev. B*, 68:161307, 2003.

[35] Yan. Chen, Jiaxiang. Zhang, Michael. Zopf, Kyubong. Jung, Yang. Zhang, Robert. Keil, Fei. Ding, and Oliver. G. Schmidt. Wavelength-tunable entangled photons from silicon-integrated iii-v quantum dots. *Nat Commun*, 7, 2016. Article.

[36] Raj. B. Patel, Anthony. J. Bennett, Ian. Farrer, Christine. A. Nicoll, David. A. Ritchie, and Andrew. J. Shields. Two-photon interference of the emission from electrically tunable remote quantum dots. *Nat. Photon.*, 4:632–635, 2010.

Chapter 6

Measurement of low temperature thermo-optic coefficients of PECVD silicon nitride resonator

A. W. Elshaari, I. Esmaeil Zadeh, K. D. Jöns, and V. Zwiller [1]

In this work we measure the thermo-optic coefficients of PECVD silicon nitride and silicon oxide between 18 K and 300 K. The coefficients are measured by studying the temperature dependence of the resonance wavelengths in an integrated ring resonators. The resonators show low sensitivity to temperature variations at cryogenic temperatures, and higher sensitivity as the temperature increases. We find thermo-optic coefficients of PECVD silicon nitride and silicon oxide at room temperature to be $(dn_{SiN})/dT = (2.51 \pm 0.08) \times 10^{-5} RIU/K^o$ and $(dn_{SiO_2})/dT = (0.96 \pm 0.09) \times 10^{-5} RIU/K^o$. The presented results provide new practical guidelines in designing photonic circuits for studying low temperature optical phenomena.

6.1 Introduction

Silicon Nitride (SiN) is a CMOS-compatible material well known to the computer chip industry as a dielectric insulator [1]. In the past few years, it has been one of the main platforms for building integrated photonic circuits. Besides offering CMOS compatibility, it has the advantages of relatively large refractive index contrast with silicon oxide enabling dense and small footprint devices [2,3], it has no two-photon absorption in the telecom wavelength range due to its large bandgap [4], and it offers relatively large thermal/Kerr coefficients at

[1] The results in this chapter have been published in IEEE Photonics Journal, vol. 8, no. 3, 2016.

room temperatures[5]. These properties ,among others, enabled a wide variety of applications utilizing linear optical components with low propagation loss[6–8], high-Q resonators[7,9,10], and all-optical signal processing/amplification[11,12]. Naturally, extensive studies to determine the room-temperature thermo-optic properties of SiN have been conducted. Based on integrated waveguide-technique, the room temperature thermo-optic coefficient of SiN was previously reported[5,13,14]. Low temperature values of the thermo-optic coefficient were only reported for amorphous SiN down to 80 K using Fabry-Pèrot measurements[15]. Based on the fitted data, a numerical model was constructed, but unfortunately the model breaks-down below 50 K. While characterization at even lower temperatures is highly desired for on chip quantum photonic applications, no detailed study of the thermo-optic properties of the material at low temperatures have been performed. The quality of integrated optical components depends on the precision of the refractive index information available. Although the absolute value of the index sets the operation point of the device, any fluctuations in temperature will change the refractive index and hence change the optical properties. These fluctuations in the temperature can play a major role in limiting the accuracy of on-chip interferometric and resonant elements. In addition, when building on-chip cryogenic circuits, the available thermal budget for thermo-optic tuning should be carefully investigated. For these reason it's of prime importance to have knowledge of the thermo-optic coefficient of the constituent materials dn/dT at low temperatures. In this work, we measure the thermo-optic coefficient of SiN and SiO_2 between 18 K to 300 K based on integrated circuit approach and test the performance of a fully integrated tunable filter. Integrated optical circuits operating at cryogenic temperatures have been used for single photon detection[16,17] , coupling from on-chip emitters[18,19], entangled photon generation with nonlinear processes[20,21], and spectrograph calibration[22]. Beside faster carrier dynamics and reduced noise[23], low temperature operation is crucial for many applications such as coupling to superconducting single-photon detectors[24]. The thermo-optic coefficient plays an important role in tuning[25] and stabilization[26] of integrated optical circuits. Silicon nitride/silicon oxide based photonic circuits are promising candidate for quantum photonic circuits. Any deviation in the designed optical properties when used under high power or subjected to thermal fluctuations are of prime importance and will degrade the overall performance[27].

6.2 Fabrication

Here we characterize the thermo-optic coefficient of PECVD SiN and Silicon Oxide (SiO_2) based on studying the resonance tuning of whispering gallery mode cavity from 18 K to 300 K. The devices were fabricated on a bare silicon wafers covered with 3μm-thick thermal oxide. This layer serves as a low index barrier for total internal reflection in SiN optical channel. Then 200 nm of SiN was deposited using PECVD at $300°C$, following a similar process in previously reported work[28]. Waveguides and ring resonators are patterned with 100 KeV e-beam lithography on 950K PMMA resist. After developing the resist, features were transferred to the SiN by complete etching of the SiN layer selectively using CHF_3/Ar

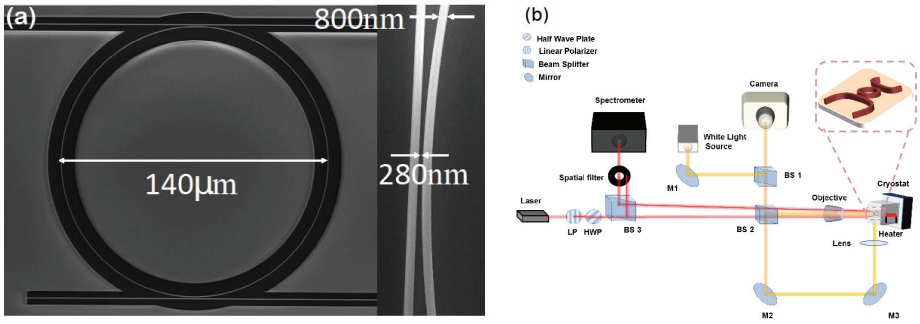

Figure 6.1 | The fabricated chip and the measurement setup. (a) SEM image of the SiN ring resonator used in the experiment. The resonator has a diameter of 140 μm with waveguide-ring gap of 280 nm. (b) 2-focii experimental setup showing the chip mounted in a continuous flow-cryostat with a local heater. More details are included in the main text.

based reactive ion etching. This was followed by a short O_2 plasma cleaning step. Finally, the chip was cladded with 2µm PECVD SiO_2 for better mode confinement of both orthogonal modes in the waveguide.

The chip design employed a U-shape structure[29] with input and output waveguide separation of 40μm. This simplifies coupling to/from the side facet of the chip and separates input and output beams spatially. Furthermore, the waveguides were terminated with inverse taper for efficient coupling and to allow only the fundamental mode to be excited[10,30]. The taper is adiabatically changed to the main waveguide width of 800 nm. The resonator is designed to have a diameter of 140 μm and gaps of 280 nm separating it from the bus waveguides. An SEM image of the fabricated device is shown in Fig. 6.1(a). For testing, the chip is cleaved at the inverse taper region along the wafer crystal direction to achieve a smooth facet for enhanced coupling.

The experimental setup is shown in Fig. 6.1b. It consists of a continuous flow cryostat equipped with a PID controlled heater. The imaging system allows viewing the top/side of the chip independently through removable beam splitter BS2 and mirror M2. The side view helps to evaluate the laser spot while exciting the waveguide. For the excitation, we use a super-continuum source equipped with acoustic optical tunable filter. Light is launched to the chip through a half-wave plate and a linear polarizer to control input-state polarization. Finally, the output beam is directed to a 750 mm spectrometer set with 1800 g/mm grating terminated with a CCD. The drop port transmission of TE and TM modes is shown in

Fig. 6.2(a). The quality factors of TM and TE modes are 12400 and 27000, respectively. For the ring-bus waveguide gap of 280 nm, TE modes are under-coupled which is indicated by the higher Q.

6.3 Masurement and results

The sample temperature is modified using the PID controlled heater, while measuring the transmission spectra of TM and TE modes. Fig. 6.2(b) shows the case of tuning different TM longitudinal resonant modes. We analyzed four resonances for each orthogonal waveguide mode between 850 nm and 880 nm as a function of temperature. The resonance-wavelength dependence with temperature is studied from 18 K to 300 K.

Since in a helium-flow cryostat the sample is cooled from the back(side), we investigated if there is any temperature gradient in the sample and deviation in the temperature from the built-in cryostat temperature sensor. For precise sample temperature measurements, we mount a temperature sensor directly on the sample holder. The inset of Fig. 6.2(c) shows finite element modeling of the temperature distribution in the waveguide region. The simulation shows homogenous temperature distribution where the optical mode is located. The relative resonance shift is extracted then averaged over all four resonances to minimize the measurement errors as shown in Fig. 6.2(c).

The resonance shifts are measured with respect to the resonant wavelength at 18 K for both orthogonal modes. To ensure high accuracy and thermal stability, all the measurements were taken after waiting for more than 30 minutes for each single point. No thermal fluctuations were observed during data acquisition. From the data we observe that the rate of change in resonance shift increases with temperature, suggesting a deviation from the simple linear dependence around room temperature[31]. The two orthogonal modes tune differently with temperature due to the different confinement factors of the TE and TM modes in the SiN. TM modes extend more into the SiO_2 cladding which has a lower thermo-optic coefficient than the SiN core. Additionally, we performed waveguide loss measurements at room temperature and at 18 K. The losses for TE and TM modes are 4 dB and 2.5 dB, respectively, with no temperature dependence. We attribute this to the dominance of the geometrical waveguide loss due to side wall roughness over the inherent material loss.

At low temperatures the actual sample temperature varies from the built-in temperature sensor of the continuous flow cryostat. In order to analyze the data and extract the thermo-optic coefficients of the core and cladding, following the approach presented in[13], we first extract the group index of each guiding mode. The group indexes of TM and TE modes are calculated from the two measured free-spectral-ranges (FSR) and length of the resonator[32]. For the TM resonance at 873.25 nm and the TE resonance at 873.3 nm, the measured FSRs are 0.98 nm and 0.92 nm, respectively. These correspond to mode group indexes of $n_{g,TM} = 1.767$ and $n_{g,TE} = 1.882$. Furthermore, we can calculate the resonance sensitivity for temperature changes by taking the derivative of the curve in Fig. 6.2(c) :

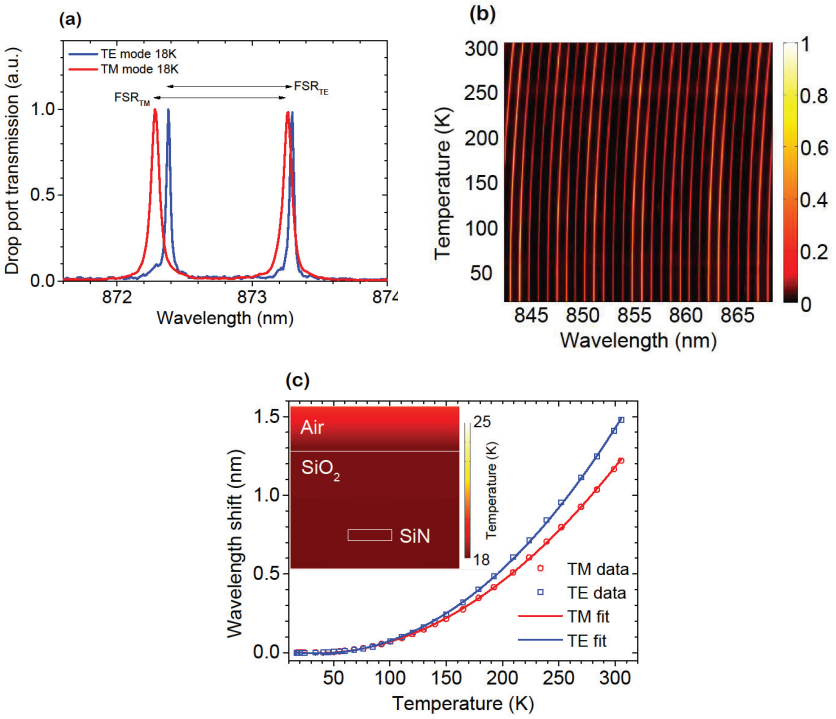

Figure 6.2 | Temperature tuning of ring resonators. (a) Drop port transmission for both TE and TM resonant modes. (b) Temperature tuning of TM resonant mode. (c) Resonance shift as a function of temperature. The shifts are measured with respect to resonant wavelengths at 18 K. The inset shows finite element method simulation for the temperature distribution at the waveguide.

$$\frac{d\lambda_{TE}}{dT}(T) = 1.033 \times 10^{-4} - 4.480 \times 10^{-6}T + 3.701 \times 10^{-7}T^2 - 6.499 \times 10^{-10}T^3 - 3.519 \times 10^{-13}T^4$$

$$\frac{d\lambda_{TM}}{dT}(T) = 2.995 \times 10^{-5} + 2.133 \times 10^{-6}T + 2.746 \times 10^{-7}T^2 - 5.525 \times 10^{-10}T^3 - 9.374 \times 10^{-14}T^4 \tag{6.1}$$

The thermo-optic coefficient of core and cladding materials are extracted by relating the

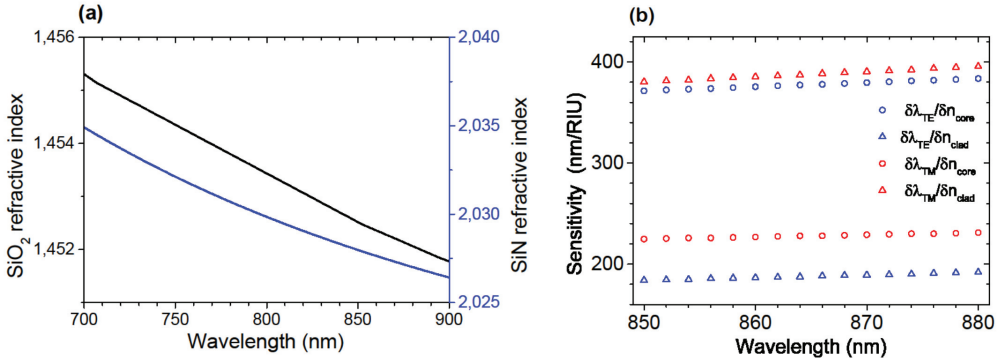

Figure 6.3 | Ellipsometry and sensitivity measurement. (a) Ellipsometry measurement of the refractive index of the core and cladding. (b) Calculated resonance sensitivity to variations in the core and cladding refractive indexes.

thermally induced resonance shifts to individual material changes[13]:

$$\begin{aligned} \frac{d\lambda_{TE}}{dT} &= \frac{\partial\lambda_{TE}}{\partial n_{core}}\frac{\partial n_{core}}{\partial T} + \frac{\partial\lambda_{TE}}{\partial n_{cladd}}\frac{\partial n_{cladd}}{\partial T} \\ \frac{d\lambda_{TM}}{dT} &= \frac{\partial\lambda_{TM}}{\partial n_{core}}\frac{\partial n_{core}}{\partial T} + \frac{\partial\lambda_{TM}}{\partial n_{cladd}}\frac{\partial n_{cladd}}{\partial T} \end{aligned} \tag{6.2}$$

To solve these coupled equations for the cladding and core temperature dependence, we initially calculate the accompanying coefficients $\partial\lambda/\partial n$. In order to model the cavities accurately we have to determine the dimensions and room temperature parameters accurately. We captured high resolution SEM images of the waveguide to model the dimensions correctly. In addition, ellipsometry measurement for the core and cladding were performed at room temperature as shown in Fig. 6.3(b). Based on the ellipsometry data, waveguide SEM images, and the measured group indexes, we use a 3-D full-vectorial mode solver to model the fabricated device and calculate the rate of change of resonance wavelength with respect to the cladding and core refractive indexes at each wavelength as shown in Fig. 6.3(c).

Using this data along with the resonance tuning in Fig. 6.2(c), we simultaneously solve equations (3) and (4). The results are shown in Fig Fig. 6.4(a) and (b). The materials thermo-optic coefficients vary by more than 1-order of magnitude between 18 K and 300 K. They approximately plateau near room temperature resulting in the linear thermo-optic effect reported in litrature. The measured values at room temperature are: $(dn_{SiN})/dT = (2.51 \pm 0.08) \times 10^{-5} RIU/K^o$ and $(dn_{SiO_2})/dT = (0.96 \pm 0.09) \times 10^{-5} RIU/K^o$.

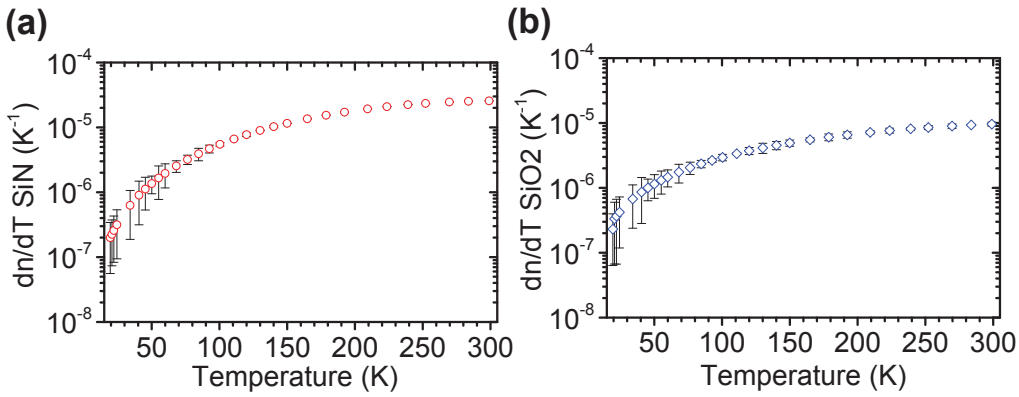

Figure 6.4 | Measurement thermo-optic coefficients of SiO_2 and SiN. (a) and (b) show thermo-optic coefficients of SiN and SiO_2, respectively, as a function of temperature.

These values show excellent agreement with recently reported work using integrated optical cavities [13] with only $\sim$2% deviation which is smaller than the measurement errors.

There are different challenges in measuring the refractive index at low temperatures. The main requirements are having good thermal stability in the system and a sensitive resonant or interferometric effect to sense minor changes in the material properties. Compared to previous integrated approaches, the measurements are performed in a continuous flow cryostat under high vacuum to yield the maximum stability. Accurate temperature extraction of the sample which is crucial to measuring the refractive index of both materials is essential. Here, two temperature measurements are performed. One with PID controlled local heater/sensor in the continuous flow cryostat, while the second is taken with a high sensitivity low temperature diode mounted directly on the sample holder.

For the tolerance values presented in Fig. 6.4(a) and Fig. 6.4(b), we performed errors propagation to include different types of errors in the measurement. First, spectrometer resolution was limited to 0.0076 nm at 1800 g/mm, putting a lower limit on the smallest measurable resonance shift. Temperature measurement error was limited by the accuracy of the voltage readings on the diode and the corresponding temperature in its response function. Finally, the fitting errors are included and propagated through all the numerical operations, which is minimized by tracking multiple resonances and averaging over them.

By fitting the measured data, we extract the temperature-dependent thermo-optic coefficients of SiN and SiO_2 for the temperature range investigated.

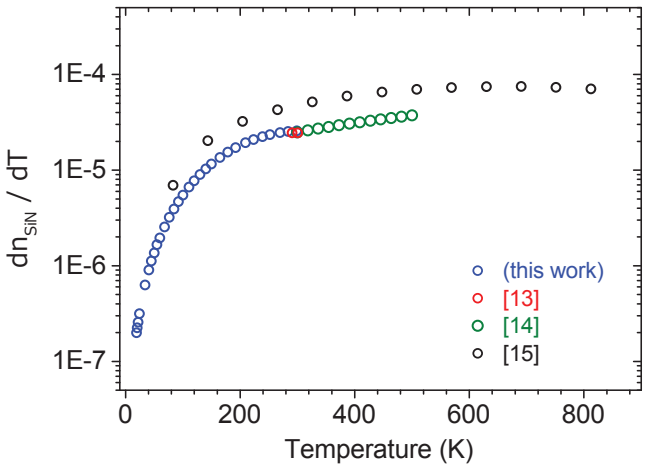

Figure 6.5 | Comparison between our measurements and the literature. Our measurements matches two previous reports.

$$\frac{dn_{SiN}}{dT}(T) = 3.211 \times 10^{-7} - 1.990 \times 10^{-8}T + 8.856 \times 10^{-10}T^2 - 1.375 \times 10^{-12}T^3 - 1.105 \times 10^{-15}T^4$$

$$\frac{dn_{SiO_2}}{dT}(T) = -1.167 \times 10^{-7} + 1.727 \times 10^{-8}T + 1.861 \times 10^{-10}T^2 - 5.781 \times 10^{-13}T^3 + 4.221 \times 10^{-16}T^4 \tag{6.3}$$

Fig. 6.5 shows reported values in literature for the thermo-optic cofficient of silicon nitride at different temperature. The presented work complements nicely the reported data in literature for the thermo-optic properties of SiN.

To stress the importance of the presented results for low temperature performance of photonic circuits, we fabricated local heaters on the ring resonators as shown in Fig. 6.6(a). The heater consists of 80 nm thick titanium resistor separated by 3 micrometers of PECVD SiO_2 from the ring. The resonance shift of the TE mode as a function of the heater voltage is shown in Fig. 6.6(b). We clearly see larger resonance tuning at room temperature compared to 18 K due to the larger thermo-optic coefficient. Furthermore, as the voltage increases the device temperature increases and the tuning becomes more efficient.

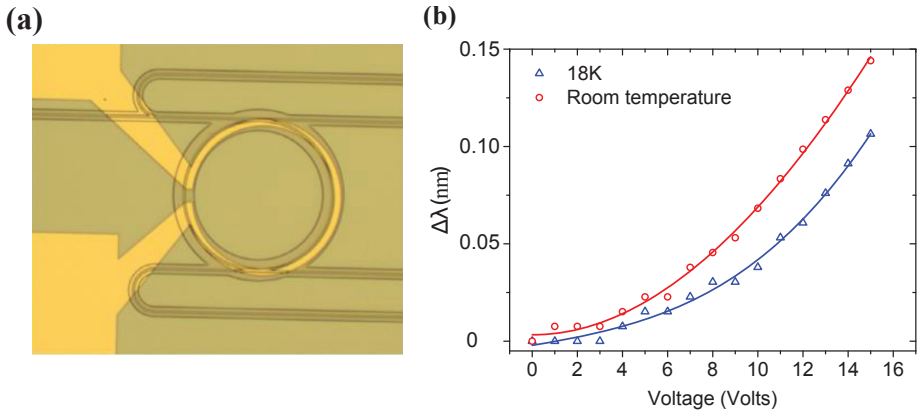

Figure 6.6 | Integrated tunable ring resonator. (a) Microscope image of a ring resonator integrated with a local heater. (b) Resonance shift of TE mode as a function of voltage for room temperature and 18 K.

6.4 conclusion

In summary, we have measured the thermo-optic coefficients of SiN and SiO_2 as a function of temperature between 18 K and 300 K. The thermo-optic coefficients change by more than one order of magnitude over the whole temperature range. The SiN resonators have considerably high thermal stability at low temperatures on the expense of tunability. As an example, we studied the performance of a fully integrated electro-optic filter at 18 K and at room temperature and showed that the filter has considerably smaller tuning range at lower temperatures. As higher temperatures generally degrade the performance of quantum emitters and single photon detectors, the less efficient tuning sets a limit on the available thermal budget for temperature tuning. The presented results can be used as a reference for future designs of complex integrated cryogenic circuits.

Bibliography

[1] D. J. Moss, R. Morandotti, a. L. Gaeta, and M. Lipson, "New cmos-compatible platforms based on silicon nitride and hydex for nonlinear optics," *Nat. Photonics*, vol. 7, pp. 597–607, 2013.

[2] J. Riemensberger, K. Hartinger, T. Herr, V. Brasch, R. Holzwarth, and T. J. Kippenberg, "Dispersion engineering of thick high-q silicon nitride ring-resonators via atomic layer deposition," *Opt. Express*, vol. 20, no. 25, pp. 27661–27669, 2012.

[3] M. a Popovíc, T. Barwicz, M. R. Watts, P. T. Rakich, L. Socci, E. P. Ippen, F. X. Kärtner, and H. I. Smith, "Multistage high-order microring-resonator add-drop filters," *Opt. Lett.*, vol. 31, no. 17, pp. 2571–2573, 2006.

[4] D. T. H. Tan, K. Ikeda, P. C. Sun, , and Y. Fainman, "Group velocity dispersion and self phase modulation in silicon nitride waveguides," *Appl. Phys. Lett.*, vol. 96, pp. 1–4, 2010.

[5] K. Ikeda, R. E. Saperstein, N. Alic, , and Y. Fainman, "Thermal and kerr nonlinear properties of plasma-deposited silicon nitride/ silicon dioxide waveguides," *Opt. Express*, vol. 16, no. 17, pp. 12987–12994, 2008.

[6] J. Bauters, M. Heck, D. D. John, M.-C. Tien, W. Li, J. S. Barton, D. J. Blumenthal, J. Bowers, A. Leinse, and R. G. Heideman, "Ultra-low-loss single-mode silicon nitride waveguides with 0.7 db/m propagation loss," in *37th European Conference and Exposition on Optical Communications*, p. Th.12.LeSaleve.3, Optical Society of America, 2011.

[7] A. Griffith, J. Cardenas, C. B. Poitras, and M. Lipson, "High quality factor and high confinement silicon resonators using etchless process," *Opt. Express*, vol. 20, no. 19, p. 21341, 2012.

[8] J. F. Bauters, M. J. R. Heck, D. John, D. Dai, M.-C. Tien, J. S. Barton, A. Leinse, R. G. Heideman, D. J. Blumenthal, and J. E. Bowers, "Ultra-low-loss high-aspect-ratio si3n4 waveguides," *Opt. Express*, vol. 19, no. 4, pp. 3163–3174, 2011.

[9] Q. Li, A. a Eftekhar, M. Sodagar, Z. Xia, A. H. Atabaki, and A. Adibi, "Vertical integration of high-q silicon nitride microresonators into silicon-on-insulator platform," *Opt. Express*, vol. 21, no. 15, pp. 18236–18248, 2013.

[10] A. Gondarenko, J. S. Levy, and M. Lipson, "High confinement micron-scale silicon nitride high q ring resonator," *Opt. Express*, vol. 17, no. 14, pp. 11366–11370, 2009.

[11] J. S. Levy, A. Gondarenko, M. a. Foster, A. C. Turner-Foster, A. L. Gaeta, and M. Lipson, "Cmos-compatible multiple-wavelength oscillator for on-chip optical interconnects," *Nat. Photonics*, vol. 4, pp. 37–40, 2010.

[12] Y. Okawachi, K. Saha, J. S. Levy, Y. H. Wen, M. Lipson, and A. L. Gaeta, "Octave-spanning frequency comb generation in a silicon nitride chip," *Opt. Lett.*, vol. 36, no. 17, pp. 3398–3400, 2011.

[13] A. Arbabi and L. L. Goddard, "Measurements of the refractive indices and thermo-optic coefficients of si3n4 and sio(x) using microring resonances," *Opt. Lett.*, vol. 38, no. 19, pp. 3878–81, 2013.

[14] A. C. Hryciw, R. D. Kekatpure, S. Yerci, L. D. Negro, and M. L. Brongersma, "Thermo-optic tuning of erbium-doped amorphous silicon nitride microdisk resonators," *Appl. Phys. Lett.*, vol. 98, no. 4, pp. 2011–2013, 2011.

[15] A. R. Zanatta and I. B. Gallo, "The thermo optic coefficient of amorphous sin films in the near-infrared and visible regions and its experimental determination," *Applied Physics Express*, vol. 6, no. 4, p. 042402, 2013.

[16] W. Pernice, C. Schuck, O.Minaeva, M. Li, G. Goltsman, A. Sergienko, and H. Tang, "High-speed and high-efficiency travelling wave single-photon detectors embedded in nanophotonic circuits," *Nat. Commun.*, vol. 3, p. 1325, 2012.

[17] C. Schuck, W. H. P. Pernice, and H. X. Tang, "Nbtin superconducting nanowire detectors for visible and telecom wavelengths single photon counting on si3n4 photonic circuits," *Appl. Phys. Lett.*, vol. 102, p. 051101, 2013.

[18] S. L. Mouradian, T. Schroeder, C. Poitras, L. Li, J. Cardenas, J. Goldstein, R. Patel, E. Chen, M. E. Trusheim, I. Bayn, M. Lipson, and D. Englund, "Efficient integration of high-purity diamond nanostructures into silicon nitride photonic circuits," in *CLEO: 2014*, p. FW1B.7, 2014.

[19] M. M. Y. Gong, S. Yerci, R. Li, M. J. Stevens, B. Baek, S. W. Nam, R. H. Hadfield, S. N. Dorenbos, V. Zwiller, J. Vuckovic, and L. D. Negro, "Linewidth narrowing and purcell enhancement in photonic crystal cavities on an er-doped silicon nitride platform," *Opt. Express*, vol. 18, no. 3, pp. 2601–2612, 2010.

[20] Y.-P. Huang, V. Velev, and P. Kumar, "Quantum frequency conversion in nonlinear microcavities," *Opt. Lett.*, vol. 38, no. 12, pp. 2119–2121, 2013.

[21] R. Wakabayashi, M. Fujiwara, K. Yoshino, Y. Nambu, M. Sasaki, and T. Aoki, "Time-bin entangled photon pair generation from si micro-ring resonator," *Opt. Express*, vol. 23, no. 2, p. 1103, 2015.

[22] T. J. Kippenberg, R. Holzwarth, and S. a Diddams, "Microresonator-based optical frequency combs," *Science*, vol. 332, no. 2, pp. 555–559, 2011.

[23] W. H. P. Pernice, C. Schuck, M. Li, and H. X. Tang, "Carrier and thermal dynamics of silicon photonic resonators at cryogenic temperatures," *Opt. Express*, vol. 19, no. 4, pp. 3290–3296, 2011.

[24] E. Schelew, M. K. Akhlaghi, and J. F. Young, "near-perfect absorbers of coherent radiation," *Nat. Commun.*, vol. 6, pp. 1–8, 2015.

[25] R. Amatya, C. W. Holzwarth, H. I. Smith, and R. J. Ram, "Precision tunable silicon compatible microring filters," *IEEE Photonics Technol. Lett.*, vol. 20, no. 20, pp. 1739–1741, 2008.

[26] S. Yokoyama, F. Qiu, Y. Feng, A. Spring, and K. Yamamoto, "0.018pm/ $^\circ c$ athermal silicon nitride ring resonator by polymer cladding," in *Lasers and Electro-Optics Pacific Rim (CLEO-PR), 2013 Conference on*, pp. 1–2, 2013.

[27] B. Guha, J. Cardenas, and M. Lipson, "Athermal silicon microring resonators with titanium oxide cladding," *Opt. Express*, vol. 21, no. 22, pp. 26557–26563, 2013.

[28] A. Gorin, A. Jaouad, E. Grondin, V. Aimez, and P. Charette, "Fabrication of silicon nitride waveguides for visible-light using pecvd: a study of the effect of plasma frequency on optical properties," *Opt. Express*, vol. 16, no. 18, pp. 13509–13516, 2008.

[29] Y. Xia, C. Qiu, X. Zhang, W. Gao, J. Shu, and Q. Xu, "Suspended si ring resonator for mid-ir application," *Opt. Lett.*, vol. 38, no. 7, pp. 1122–1124, 2013.

[30] A. C. Turner, C. Manolatou, B. S. Schmidt, M. Lipson, M. A. Foster, J. E. Sharping, and A. L. Gaeta, "Tailored anomalous group-velocity dispersion in silicon channel waveguides," *Opt. Express*, vol. 14, no. 10, pp. 4357–4362, 2006.

[31] N. Ter-Gabrielyan, V. Fromzel, and M. Dubinskii, "Linear thermal expansion and thermo-optic coefficients of yvo_4 crystals the 80-320 k temperature range," *Opt. Mater. Express*, vol. 2, no. 11, p. 1624, 2012.

[32] P. Rabiei, W. H. Steier, C. Zhang, and L. R. Dalton, "Polymer micro-ring filters and modulators," *J. Light. Technol.*, vol. 20, no. 11, pp. 1968–1975, 2002.

Chapter 7

Scalable integration and positioning of single photon sources in photonic waveguides

I. Esmaeil Zadeh *, A. W. Elshaari *, K. D. Jöns, A. Fognini, D. Dalacu, P. J. Poole, M. E. Reimer, and V. Zwiller [1]

A major step towards fully integrated quantum optics is the deterministic incorporation of high quality single-photon sources in on-chip optical circuits. We show a novel hybrid approach in which preselected III-V single quantum dots in nanowires are transferred and integrated in silicon based photonic circuits. The quantum emitters maintain their high optical quality after integration as verified by measuring a low multiphoton probability of 0.07 ± 0.07 and emission linewidth as narrow as 3.45 ± 0.48 GHz. Our approach allows for optimum alignment of the quantum dot light emission to the waveguide modes resulting in very high coupling efficiencies. We estimate a coupling efficiency of 24.3 ± 1.7 % from the studied single-photon source to the photonic channel and further show by finite-difference time-domain simulations that for an optimized choice of material and design the efficiency can exceed 90 %.

[1]The results in this chapter have been published in Nano Letters 2016 16 (4), 2289-2294

* These authors had equal contributions.

7.1 Introduction

Experiments on photons have played a key role in our understanding of quantum mechanics by probing the quantized nature of electromagnetic radiation. Since Linear Optical Quantum Computing (LOQC)[1] was proposed, there has been an ongoing effort to achieve a scalable platform for its realization. Few qubit operations have been shown[2,3] and up to eight photon entanglement has been achieved[4] using discrete optical components and parametric down conversion. Although many basic proof of principles have been demonstrated, a more scalable approach is needed for complex architectures. Recently, integrated photonics has gained significant interest as it offers scalability, robustness and ease of use for on-chip quantum computation[5–9].

A LOQC system comprises of three main components: single photon generation, manipulation, and detection. Single-photons used in integrated photonic circuits are often generated using parametric down conversion or quantum dots (QD). As opposed to parametric down conversion, QDs are suitable for on-demand single photon generation[10], narrow emission bandwidth, their emission wavelength can be tuned[11–15] and they offer the possibility of on-chip electrical excitation[16]. As for the logical quantum gates, every discrete unitary operator can be realized using only mirrors and beam splitters[17]. This makes the integrated photonic platform very attractive due to the already available components for passive and active light manipulation[18]. In addition, for single photon detection, > 90 % system efficiency has been achieved[19]. However, to realize an efficient LOQC system, it is required to interface all of these often incompatible technologies.

Significant efforts have been put into realizing LOQC on-chip. For on-chip detection, efficient coupling of superconducting nanowire single-photon detectors (SNSPD) with dielectric waveguides has been demonstrated[20,21]. As for the gate operations, complex photonic circuits for quantum operations have been realized[22,23]. In addition, QDs have been coupled to photonic cavities, nanowires, waveguides[24–26] and SNSPDs[27]. Fabricating low-loss III-V waveguides and selectively embedding single-quantum emitters is a challenge[28,29]. Moreover, growing superconducting films (for detectors) on these substrates often leads to low efficiency or high dark counts[30].

7.2 Device and experimental setup

In this work, we present a novel hybrid platform through integration of III-V preselected single QDs embedded in nanowires within robust SiN photonic circuits. Unlike the work with NV centers[31], we embed sources with directional emission that is perfectly suited for coupling to the waveguides. Figure 8.1a provides an artistic visualization of such an integrated quantum circuit element. The red spheres represent single photons that are coupled to the waveguide in the forward direction. The indium phosphide nanowires are 1.5-3 μm in length and 250-300 nm in diameter with a 3-4 nm section of indium arsenide

phosphide, forming the QD, located 200 nm from their base. During growth, once the length of the nanowire is longer than the diffusion length of indium, it tapers with an angle depending on the growth parameters[32]. For the photonic channel, the waveguide height is 200 nm with a width of 2 μm near the nanowire region to simplify alignment during fabrication. The waveguide is then tapered adiabatically to 800 nm for single mode operation. The SiN layer is formed using plasma enhanced chemical vapor deposition (PECVD) with a measured refractive index of ~ 2 near the QD emission.

Our design allows for strong overlap of the QD electric dipole moment and the fundamental modes of the waveguide since the z-quantization axis of the QD is aligned along the propagation direction of the waveguide. The QD electric dipole moment lies in the X-Y plane and can generally be represented as a linear combination of the orthogonal transverse modes (TE and TM) supported by the photonic channel. Figure 8.1b shows finite-difference time-domain (FDTD) simulations of coupling from the nanowire QD to TM and TE modes. The insets illustrate the electric field intensity in the X-direction (TE mode) and Y-direction (TM mode). For the given waveguide and nanowire geometry, the theoretical QD to waveguide coupling efficiency is 36 %. Since the tapering length for our nanowires is short, the coupling efficiency is similar for both forward and backward directions ($\sim$18 % for each direction).

We transfer preselected high quality nanowire QDs on silicon chips using a nanomanipulator. Our setup is a modified version of previous works[33,34]. It consists of a tungsten tip mounted on a x-y-z movable stage imaged by a high resolution optical microscope. The nanowire is detached at its base from the growth chip, then due to van der Waals forces it adheres to the tungsten tip. The nanowire is then transferred to a silicon chip with < 500 nm position and < 2 degrees rotation precision. Inset 1 of Figure 8.2a was captured while a nanowire was being transferred using a nanomanipulator. The chip was prepared with 2.4 μm of buried silicon oxide serving as a low index buffer between the SiN waveguide and Si substrate, as well as pre-fabricated markers to align the photonic circuit with respect to the nanowire. These markers allow for very precise alignment of the nanowires within the waveguide circuits (< 50 nm if required). After the nanowire transfer process we encapsulate the nanowire in SiN, which acts as the core of the photonic channel. The photonic circuits are patterned and etched with respect to the alignment features and finally cladded with PMMA for symmetric mode confinement. Figure 8.2a shows a color coded microscope image of a single nanowire positioned within a SiN waveguide.

An important milestone toward monolithic integration of quantum optical circuits is to operate and link multiple on-chip sources. Using our method, it is possible to: preselect many quantum emitters, transfer them to a silicon chip, embed them in waveguide material, select the desired ones (in terms of emission wavelength, intensity, linewidth, etc.), and then route their emission to different input ports of photonic circuits. Inset 2 of Figure 8.2a shows an optical microscope image of multiple quantum emitters integrated on the same photonic circuit. Together with electrical[35] and strain tuning[36] of nanowires, our approach allows for complex fully integrated quantum circuits.

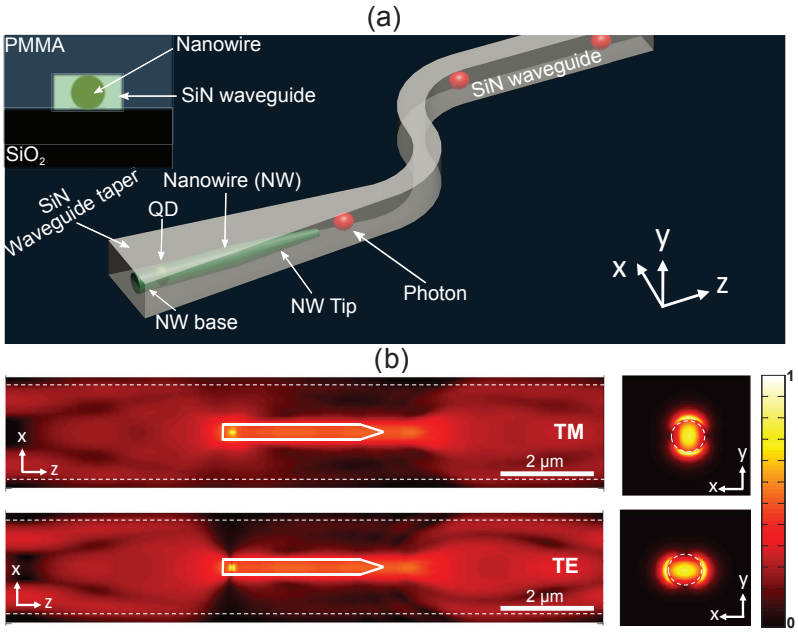

Figure 7.1 |(a) Schematic view of the device, where a III-V QD in a nanowire is embedded in a SiN photonic waveguide. The emitted photons are depicted with red spheres propagating along the waveguide (only the forward direction is shown). (b) 3D FDTD simulations for the embedded QD emission at 880 nm. Horizontal cuts of the electric field profile are shown for both of the orthogonal polarization directions. The SiN waveguide boundaries are shown by the dashed lines. The insets show vertical cuts of the electric field intensity profile at the QD for both TE and TM modes. The total simulated coupling efficiency for unpolarized emission from the dot to the guided modes in the SiN waveguide is 36 % (∼18 % for forward and backward directions).

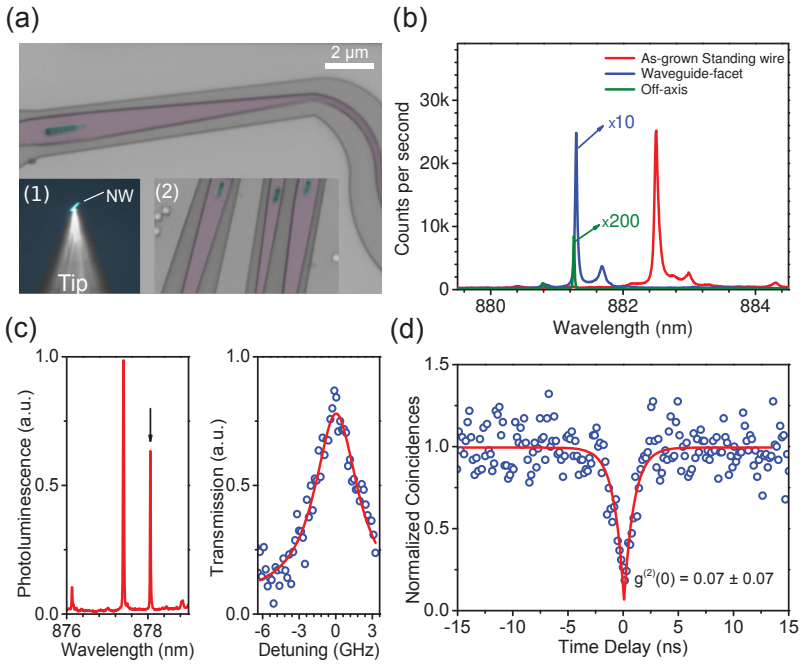

Figure 7.2 |(a) Color coded microscope image of a single nanowire (green) integrated in a photonic waveguide (purple). Inset 1 shows a single nanowire attached to the tip of the nanomanipulator used during the nanowire transfer process. Inset 2 shows multiple selected nanowires coupled to different photonic channels. (b) Emission spectrum of a standing as-grown nanowire sample (red), its spectrum after encapsulation captured perpendicular to its growth axis (green), and finally, its emission collected from the end-facet of the SiN waveguide (blue). The emission is blue shifted after nanowire transfer and encapsulation in SiN due to strain. (c) A scanning Fabry Pérot measurement (right) for an emission line from a nanowire QD indicated by an arrow (left). The Lorentzian fit shows a narrow linewidth with a FWHM of 3.45 ± 0.48 GHz ($\Delta\lambda = \sim 0.009$ nm). (d) Second-order correlation measurement showing multiphoton emission probability as low as 0.07 ± 0.07.

7.3 Results

Figure 8.2b compares the emission spectra of a nanowire QD before and after processing. The red spectrum originates from the as-grown nanowire QD sample collected from the nanowire tip, the green curve is the emission spectrum of the encapsulated nanowire QD captured perpendicular to its growth axis, and the blue curve is the spectrum collected from the waveguide-facet. As observed in Figure 8.2b, even without taking the facet-loss into account, the collected light intensity from the waveguide-facet is ~ 60 times higher than the off-axis

QD emission. This large difference is due to the high mode matching between the electric dipole moment of the QD and the fundamental modes of the waveguide. The peak intensity of the QD emission measured from the waveguide-facet is 10 % of its intensity as measured when the nanowire was still standing on the original growth chip (as-grown). We attribute this decrease to the coupling loss from the nanowire into the waveguide, the propagation loss in the waveguide and the waveguide-facet loss. After transfer and deposition of SiN, the QD emission is 1.5 nm (2.4 meV) blue shifted due to strain[37]. We note that the small difference in the emission wavelength between the blue and green spectra is attributed to the difference in temperature of the two different mounts used for on-axis and off-axis measurements.

Sources with long coherence time and high single-photon emission probability are required for LOQC. To verify the high optical quality of our integrated sources, we carried out a scanning Fabry Pérot measurement on an emission line of an encapsulated QD presented in the left panel of Figure 8.2c. The right panel of Figure 8.2c shows the measurement results. A Lorenztian fit on the transmission spectra yields a FWHM of 3.45 ± 0.48 GHz. This value is a factor of ~ 7 larger than the Fourier-transform limit. The linewidth can be improved by resonant excitation[38] and further cooling of the sample[39].In addition, we performed an autocorrelation measurement using continuous wave excitation at 632.8 nm to determine the single-photon purity of the photons guided along the photonic circuit. The results are presented in Figure 8.2d. A multiphoton emission probability of $g^2(0) = 0.07 \pm 0.07$ was measured. Furthermore, from the fitted data, we estimate an emission life time of $T_1 = 0.9 \pm 0.1$ ns. These results show the high emission quality of the integrated sources, despite several processing steps including electron beam lithography, deposition, and reactive ion etching.

Our hybrid approach enables selection from a variety of materials with low propagation losses for the waveguide. Shown in Figure 8.3a, we measured the propagation loss for both TE and TM modes of our waveguide using the cut-back method[40] to be 4.0 ± 0.3 dB/cm and 2.5 ± 0.4 dB/cm, respectively. This measurement was conducted using a tunable laser at 880 nm to match the quantum dot emission. The higher loss for TE is attributed to the larger overlap with the etched sidewalls as compared to TM. Additionally, we characterized the facet losses of TE and TM modes for different waveguide widths at the facet as shown in Figure 8.3b. For our device, highlighted in Figure 8.3b, the measured facet loss is 7.2 dB and 4.5 dB for TE and TM modes, respectively.

We studied the emission intensity as a function of polarization, shown in Figure 8.3c. Expected from the large difference in the facet loss for TE and TM modes, our source appears partially polarized. The facet losses can be improved by reducing the waveguide width adiabatically[41] to closely match the TM and TE modes to the collection objective. As shown in Figure 8.3b, for a 200 nm waveguide width at the facet, the difference in TE and TM facet losses falls below 0.7 dB and the total loss improves by ~ 2 dB as compared to our current device. This enhanced collection efficiency for smaller taper widths is similar to the case of as-grown nanowires[42], where the tapered section of the nanowire is used for mode conversion, and improving the extraction efficiency.

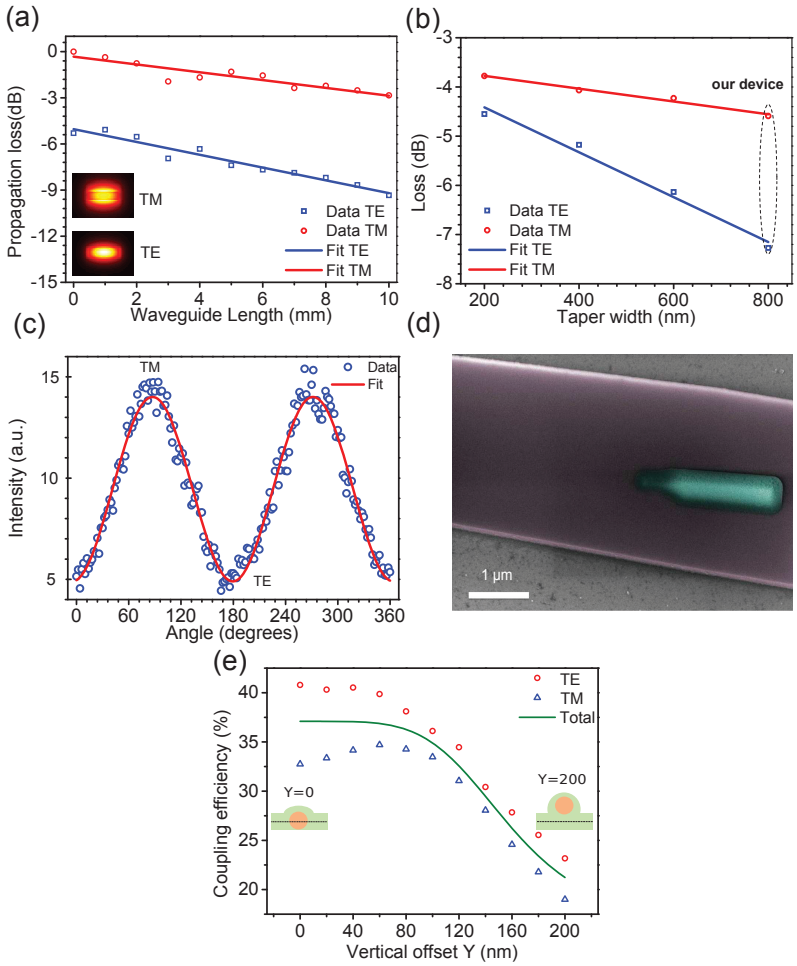

Figure 7.3 |(a) Measurement of propagation losses for TE and TM modes using the cut-back method. TM and TE modes propagation losses are 2.5 ± 0.4 dB/cm and 4.0 ± 0.3 dB/cm, respectively. (b) Waveguide-facet losses for TE and TM modes versus waveguide width at the end-facet. (c) Polarization measurement on the collected photons from the waveguide-facet. (d) Colored SEM image of the nanowire-waveguide device. Shown in purple is the SiN waveguide. The nanowire (white) in covered with a layer of SiN (green). The nanowire is shifted vertically from the center of the SiN waveguide due to the nature of the PECVD process. (e) Simulated coupling efficiency for TE and TM photons emitted from the QD as a function of the vertical offset Y of the nanowire from the center of the waveguide core. As shown in the two insets, a centered nanowire corresponds to Y=0, while for a nanowire lying on top of the waveguide Y=200 nm.

Taking into account the waveguide losses and by comparing the emission spectra from the encapsulated device and from the as-grown sample, we estimate a unidirectional nanowire QD to waveguide coupling efficiency of $\sim 12.2 \pm 1.7\%$ ($\sim$24.3% for both forward and backward directions. The unidirectional coupling efficiency is smaller than the theoretical value of 18 %. To better understand the remaining mechanisms for coupling loss, a scanning electron microscope image of one of the devices is presented in Figure 8.3d. As is observed, the nanowire is not embedded at the center of the photonic channel. During the deposition of PECVD SiN, due to the gaseous process, material builds up isotropically on all surfaces. This lifts-up the nanowire from the substrate and reduces the overlap between the electronic transition dipole moment of the QD and the electric field of the supported waveguide optical modes. We calculate the coupling efficiency as a function of vertical displacement of the nanowire with respect to the waveguide center. The results are shown in Figure 8.3e. The total simulated bidirectional coupling efficiency for unpolarized light varies from $\sim$36 % for a perfectly centered wire to $\sim$22 % for a wire which is lying on top of the waveguide (no geometrical overlap). The coupling is slightly stronger for the TE mode than the TM mode because of the asymmetric geometry of the waveguide. To avoid nanowire displacement, one can combine the PECVD process with a thin sputtered layer of SiN to anchor the nanowires on the substrate. Alternatively, other high quality sputtered waveguide technologies like aluminum nitride [43] can be used.

High system efficiency is vital for many applications in quantum optics [44]. Therefore, to address and improve the extraction efficiency from our sources, we theoretically optimize the waveguide geometry and material. The optimized design consists of a silicon carbide (SiC) waveguide suspended in air with dimensions of 500 nm $\times$ 500 nm. The refractive index of silicon carbide is 2.6 [45] at the wavelengths of interest which provides a contrast of 1.6 with air cladding. Waveguides with loss as low as 5 dB/cm can be made using SiC films deposited by PECVD at temperatures compatible with our devices [46]. We performed 3D FDTD modeling to estimate the coupling efficiency from a nanowire QD to the guided modes of a SiC waveguide. The symmetric design of the waveguide closely matches the coupling for both orthogonal electronic dipole transitions of the QD. The coupling efficiency to each side is $\sim$46% (92% in total) for unpolarized light.

To produce on-demand single photons on-chip [47], all photons must be steered in one direction. For this purpose we designed a broadband 1D mirror consisting of etched squares of dimensions 132 nm $\times$ 400 nm with a lattice constant of 232 nm along the waveguide. Figure 8.4a illustrates the design and Figure 8.4b shows the coupling efficiency as a function of wavelength. The device provides a unidirectional coupling efficiency greater than 86 % at 880 nm. As shown in the gray highlighted area of Figure 8.4b, the coupling efficiency has negligible sensitivity to polarization over the typical emission range of our QDs. The polarization-insensitive high coupling efficiency combined with symmetric waveguide geometry make our device ideal for experiments with polarization-entangled photons. Figure 8.4c represents the electric field intensity profile of guided TE and TM modes at 880 nm.

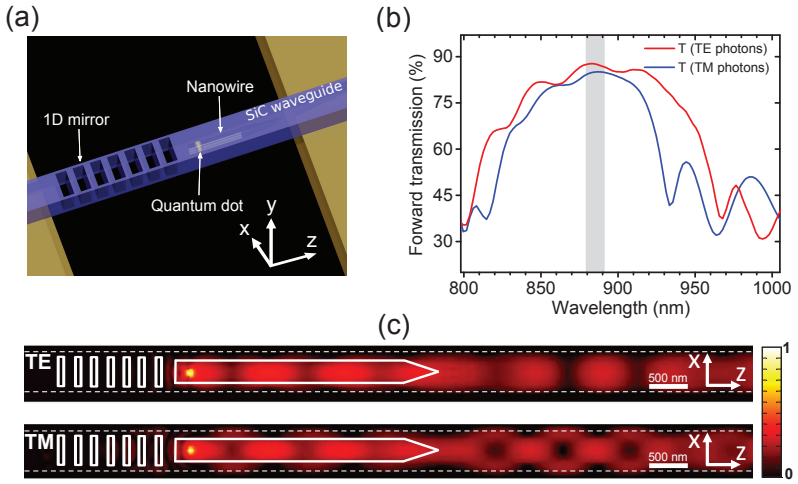

Figure 7.4 |(a) Proposed device for efficient unidirectional coupling to a single mode waveguide from a nanowire-based QD. The device consists of a SiC waveguide with size 500 nm × 500 nm suspended in air. A 1D mirror consisting of etched squares is used to direct the photons in the forward direction of the waveguide. The etched squares have dimensions of 132 nm × 400 nm and a lattice constant of 232 nm along the z-direction. (b) The unidirectional coupling efficiency of the QD to waveguide calculated with 3D FDTD simulations. The total coupling efficiency is ∼92 % with more than 86 % for the forward propagating modes. High coupling efficiency is achieved because of high reflectivity of the mirror at the desired wavelength. (c) Electric field intensity profile of guided TE and TM modes at 880 nm. The photons are reflected by the mirror toward the right side. Dashed lines show the SiC waveguide boundaries.

7.4 Conclusion

In summary, we have demonstrated controlled integration of preselected nanowire-based single quantum emitters into photonic waveguides. Our novel technique enables scalable integration of selected sources in complex photonic architectures on a single chip. The integrated sources maintain their high optical quality in terms of single photon purity, line width, and intensity with a coupling efficiency to waveguide ase high as 24%. Furthermore, we showed theoretically that for a suspended SiC waveguide, in conjunction with a 1-D Bragg reflector, a unidirectional coupling efficiency greater than 86 % can be realized. Coupling our quantum emitters to on-chip photonic cavities will allow to investigate the rich physics of cavity quantum electrodynamics, thus enhancing the spontaneous emission rate to accelerate the emission lifetime and approach Fourier-transform limited photons. Finally, by local tuning of the emission energy of single photon sources, indistinguishable photons can be generated as a necessary step towards on-chip optical quantum computation.

Bibliography

[1] E. Knill, R. Laflamme, and G. J. Milburn, "A scheme for efficient quantum computation with linear optics," *Nature*, vol. 409, pp. 46–52, 2001.

[2] J. L. O'Brien, G. J. Pryde, A. G. White, T. C. Ralph, and D. Branning, "Demonstration of an all-optical quantum controlled-not gate," *Nature*, vol. 426, no. 5, pp. 264–267, 2003.

[3] S. Gasparoni, J.-W. Pan, P. Walther, T. Rudolph, and A. Zeilinger, "Realization of a photonic controlled-not gate sufficient for quantum computation," *Phys. Rev. Lett.*, vol. 93, p. 020504, 2004.

[4] X.-C. Yao, T.-X. Wang, J. X. Ping, X.-H. B. He. Lu, Ge-Sheng. Pan, C.-Z. Peng, C.-Y. Chen, and J.-W. Pan, "Observation of eight-photon entanglement," *Nat. Photon*, vol. 6, pp. 225–228, 2012.

[5] A. Politi, M. J. Cryan, J. G. Rarity, S. Yu, and J. L. O'Brien, "Silica-on-silicon waveguide quantum circuits," *Science*, vol. 320, pp. 646–649, 2008.

[6] A. Politi, J. C. F. Matthews, and J. L. O'Brien, "Shor's quantum factoring algorithm on a photonic chip," *Science*, vol. 325, p. 1221, 2009.

[7] L. Sansoni, F. Sciarrino, G. Vallone, P. Mataloni, A. Crespi, R. Ramponi, and R. Osellame, "Polarization entangled state measurement on a chip," *Phys. Rev. Lett.*, vol. 105, p. 200503, 2010.

[8] A. Peruzzo, P. Shadbolt, N. Brunner, S. Popescu, and J. L. O'Brien, "A quantum delayed-choice experiment," *Science*, vol. 338, pp. 634–637, 2012.

[9] J. B. Spring, B. J. Metcalf, P. C. Humphreys, S. W. Kolthammer, X.-M. Jin, M. Barbieri, A. Datta, N. Thomas-Peter, N. K. Langford, D. Kundys, J. C. Gates, B. J. Smith, P. G. R. Smith, and I. A. Walmsley, "Boson sampling on a photonic chip," *Science*, vol. 339, pp. 798–801, 2013.

[10] M. Müller, S. Bounouar, K. D. Jöns, M. Glässl, and P. Michler, "On-demand generation of indistinguishable polarization-entangled photon pairs," *Nat. Photon*, vol. 8, pp. 224–228, 2013.

[11] B. D. Gerardot, S. Seidl, P. A. Dalgarno, R. J. Warburton, D. Granados, J. M. Garcia, K. Kowalik, O. Krebs, K. Karrai, A. Badolato, and P. M. Petroff, "Manipulating exciton fine structure in quantum dots with a lateral electric field," *Appl. Phys. Lett.*, vol. 90, p. 041101, 2007.

[12] A. J. Bennett, M. A. Pooley, R. M. Stevenson, R. B. P. M. B. Ward, A. B. de la Giroday, N. Sköld, I. Farrer, C. A. Nicoll, D. A. Ritchie, and A. J. Shields, "Electric-field-induced coherent coupling of the exciton states in a single quantum dot," *Nat. Phys*, vol. 6, pp. 947–950, 2010.

[13] S. Seidl, M. Kroner, A. Högele, K. Karrai, R. J. Warburton, A. Badolato, and P. M. Petroff, "Effect of uniaxial stress on excitons in a self-assembled quantum dot," *Appl. Phys. Lett.*, vol. 88, p. 203113, 2006.

[14] A. Rastelli, F. Ding, J. D. Plumhof, S. Kumar, R. Trotta, C. Deneke, A. Malachias, P. Atkinson, E. Zallo, T. Zander, and et al., "Controlling quantum dot emission by integration of semiconductor nanomembranes onto piezoelectric actuators," *Phys. Status Solidi B*, vol. 249, no. 4, pp. 687–696, 2012.

[15] R. Trotta, J. Martin-Sanchez, J. S. Wildmann, G. Piredda, M. Reindl, C. Schimpf, E. Zallo, S. Stroj, J. Edlinger, and A. Rastelli, "Wavelength-tunable sources of entangled photons interfaced with atomic vapours," *Nat. Commun.*, vol. 7, 2016.

[16] Z. Yuan, B. E. Kardynal, R. M. Stevenson, A. J. Shields, C. J. Lobo, K. Cooper, N. S. Beattie, D. A. Ritchie, and M. Pepper, "Electrically driven single-photon source," *Science*, vol. 295, pp. 102–105, 2002.

[17] M. Reck, A. Zeilinger, H. J. Bernstein, and P. Bertani, "Experimental realization of any discrete unitary operator," *Phys. Rev. Lett.*, vol. 73, pp. 58–61, 1994.

[18] M. Lipson, "Guiding, modulating, and emitting light on silicon-challenges and opportunities," *J. Lightwave Technol.*, vol. 23, pp. 4222–4238, 2005.

[19] F. Marsili, V. B. Verma, J. A. Stern, S. Harrington, A. E. Lita, T. Gerrits, Vayshenker, B. Baek, M. D. Shaw, R. P. Mirin, and S. W. Nam, "Detecting single infrared photons with 93% system efficiency," *Nat. Photon*, vol. 7, pp. 210–214, 2013.

[20] W. Pernice, C. Schuck, O.Minaeva, M. Li, G. Goltsman, A. Sergienko, and H. Tang, "High-speed and high-efficiency travelling wave single-photon detectors embedded in nanophotonic circuits," *Nat. Commun.*, vol. 3, 2012.

[21] C. Schuck, W. H. P. Pernice, and H. X. Tang, "Nbtin superconducting nanowire detectors for visible and telecom wavelengths single photon counting on si3n4 photonic circuits," *Appl. Phys. Lett.*, vol. 102, p. 051101, 2013.

[22] E. Martin-Lopez, A. Laing, T. Lawson, R. Alvarez, X.-Q. Zhou, and J. L. O'Brien, "Experimental realization of shor's quantum factoring algorithm using qubit recycling," *Nat. Photon.*, vol. 6, pp. 773–776, 2012.

[23] J. Carolan, C. Harrold, C. Sparrow, E. Martín-López, N. J. Russell, J. W. Silverstone, P. J. Shadbolt, N. Matsuda, M. Oguma, M. Itoh, and et al., "Universal linear optics," *Science*, vol. 349, pp. 711–716, 2015.

[24] A. Badolato, K. Hennessy, M. Atatüre, J. Dreiser, E. Hu, P. M. Petroff, and A. Imamoğlu, "Deterministic coupling of single quantum dots to single nanocavity modes," *Science*, vol. 308, no. 5725, pp. 1158–1161, 2005.

[25] J. Claudon, J. Bleuse, N. S. Malik, M. Bazin, P. Jaffrennou, N. Gregersen, C. Sauvan, P. Lalanne, and J.-M. Gerard, "A highly efficient single-photon source based on a quantum dot in a photonic nanowire," *Nat. Photon.*, vol. 4, no. 3, pp. 174–177, 2010.

[26] M. N. Makhonin, J. E. Dixon, R. J. Coles, B. Royall, I. J. Luxmoore, E. Clarke, M. Hugues, M. S. Skolnick, and A. M. Fox, "Waveguide coupled resonance fluorescence from on-chip quantum emitter," *Nano Letters*, vol. 14, no. 12, pp. 6997–7002, 2014. PMID: 25381734.

[27] G. Reithmaier, S. Lichtmannecker, T. Reichert, P. Hasch, K. Müller, M. Bichler, R. Gross, and J. J. Finley, "On-chip time resolved detection of quantum dot emission using integrated superconducting single photon detectors," *Sci. Rep.*, vol. 3, 2013.

[28] K. D. Jöns, U. Rengstl, M. Oster, F. Hargart, M. Heldmaier, S. Bounouar, S. M. Ulrich, M. Jetter, and P. Michler, "Monolithic on-chip integration of semiconductor waveguides, beamsplitters and single-photon sources," *J. Phys. D: Appl. Phys.*, vol. 48, p. 085101, 2015.

[29] N. Prtljaga, R. J. Coles, J. O'Hara, B. Royall, E. Clarke, A. M. Fox, and M. S. Skolnick, "Monolithic integration of a quantum emitter with a compact on-chip beam-splitter," *Appl. Phys. Lett.*, vol. 104, p. 231107, 2014.

[30] G. Reithmaier, J. Senf, S. Lichtmannecker, T. Reichert, F. Flassig, A. Voss, R. Gross, and J. J. Finley, "Optimisation of nbn thin films on gaas substrates for in-situ single photon detection in structured photonic devices," *J. Appl. Phys.*, vol. 113, p. 143507, 2013.

[31] S. L. Mouradian, T. Schröder, C. B. Poitras, L. Li, J. Goldstein, E. H. Chen, M. Walsh, J. Cardenas, M. L. Markham, D. J. Twitchen, M. Lipson, and D. Englund, "Scalable integration of long-lived quantum memories into a photonic circuit," *Phys. Rev. X*, vol. 5, p. 031009, 2015.

[32] D. Dalacu, K. Mnaymneh, J. Lapointe, X. Wu, P. J. Poole, G. Bulgarini, V. Zwiller, and M. E. Reimer, "Ultraclean emission from inasp quantum dots in defect-free wurtzite inp nanowires," *Nano Lett.*, vol. 12, pp. 5919–5923, 2012.

[33] J. Wolters, A. W. Schell, G. Kewes, N. Nüsse, M. Schoengen, H. Döscher, T. Hannappel, B. Löchel, M. Barth, and O. Benson, "Enhancement of the zero phonon line emission from a single nitrogen vacancy center in a nanodiamond via coupling to a photonic crystal cavity," *Appl. Phys. Lett.*, vol. 97, no. 14, 2010.

[34] M. Benyoucef, S. Kiravittaya, Y. F. Mei, A. Rastelli, and O. G. Schmidt, "Strongly coupled semiconductor microcavities: A route to couple artificial atoms over micrometric distances," *Phys. Rev. B*, vol. 77, 2008.

[35] M. E. Reimer, M. P. van Kouwen, A. W. Hidma, M. H. M. van Weert, E. P. A. M. Bakkers, L. P. Kouwenhoven, and V. Zwiller, "Electric field induced removal of the biexciton binding energy in a single quantum dot," *Nano Letters*, vol. 11, no. 2, pp. 645–650, 2011. PMID: 21226507.

[36] P. E. Kremer, A. C. Dada, P. Kumar, Y. Ma, S. Kumar, E. Clarke, and B. D. Gerardot, "Strain-tunable quantum dot embedded in a nanowire antenna," *Phys. Rev. B*, vol. 90, 2014.

[37] M. B. Bavinck, M. Zieliński, B. J. Witek, T. Zehender, E. P. A. M. Bakkers, and V. Zwiller, "Controlling a nanowire quantum dot band gap using a straining dielectric envelope," *Nano Lett.*, vol. 12, pp. 6206–6211, 2012.

[38] A. V. Kuhlmann, J. H. Prechtel, J. Houel, A. Ludwig, D. Reuter, A. D. Wieck, and R. J. Warburton, "Transform-limited single photons from a single quantum dot," *Nat. Commun.*, vol. 6, 2015.

[39] M. E. Reimer, G. Bulgarini, R. Heeres, B. J. Witek, M. A. M. Versteegh, D. Dalacu, J. Lapointe, P. J. Poole, and V. Zwiller, "Overcoming power broadening of the quantum dot emission in a pure wurtzite nanowire," *ArXiv e-prints*, vol. 1407.2833, 2014.

[40] Y. Vlasov and S. McNab, "Losses in single-mode silicon-on-insulator strip waveguides and bends," *Opt. Express*, vol. 12, no. 8, pp. 1622–1631, 2004.

[41] V. R. Almeida, R. R. Panepucci, and M. Lipson, "Nanotaper for compact mode conversion," *Opt. Lett.*, vol. 28, pp. 1302–1304, 2003.

[42] M. E. Reimer, G. Bulgarini, N. Akopian, M. Hocevar, M. B. Bavinck, M. A. Verheijen, E. P. Bakkers, L. P. Kouwenhoven, and V. Zwiller, "Bright single-photon sources in bottom-up tailored nanowires," *Nat. Commun.*, vol. 3, no. 737, 2012.

[43] C. Xiong, W. H. P. Pernice, X. Sun, C. Schuck, K. Y. Fong, and H. X. Tang, "Aluminum nitride as a new material for chip-scale optomechanics and nonlinear optics," *New Journal of Physics*, vol. 14, no. 9, 2012.

[44] P. Kok, W. J. Munro, K. Nemoto, T. C. Ralph, J. P. Dowling, and G. J. Milburn, "Linear optical quantum computing with photonic qubits," *Rev. Mod. Phys.*, vol. 79, pp. 135–174, 2007.

[45] S. Singh, J. R. Potopowicz, L. G. V. Uitert, and S. H. Wemple, "Nonlinear optical properties of hexagonal silicon carbide," *J. Appl. Phys.*, vol. 19, pp. 53–56, 1971.

[46] Y. Shoji, K. Nakanishi, Y. Sakakibara, K. Kintaka, H. Kawashima, M. Mori, and T. Kamei, "Hydrogenated amorphous silicon carbide optical waveguide for telecommunication wavelength applications," *Appl. Phys. Express*, vol. 3, p. 122201, 2010.

[47] I. Söllner, S. Mahmoodian, S. L. Hansen, L. Midolo, A. Javadi, G. Kiršanskė, T. Pregnolato, H. El-Ella, E. H. Lee, J. D. Song, S. Stobbe, and P. Lodahl, "Deterministic photon–emitter coupling in chiral photonic circuits," *Nat. Nano.*, vol. 10, pp. 775–778, 2015.

Chapter 8

Scalable and robust coupling of a single-photon emitter to an optical fiber

I. Esmaeil Zadeh, A. Fognini, K. D. Jöns, K. Zeuner, A. W. Elshaari, L. Schweickert and V. Zwiller [1]

Over the past two decades, many important proof-of-principle quantum optics experiments were carried out by utilizing one or few single-photon sources. To realize more sophisticated and demanding experiments, a robust and scalable approach is required. Achieving a platform for the coupling of many sources to single mode optical fibers is highly desired for ambitious applications. Here we demonstrate a reliable method to couple photons generated from a nano-scale single-photon source to an optical fiber. In addition, we implement a fully fiber-based platform from source to detector. Our technique is compatible with different emitters and is cost and time efficient.

8.1 Introduction

The applications of single-photon sources include quantum cryptography [1], quantum optical information processing [2], quantum sensing and imaging [3–5]. Among different types of single-photon emitters are the solid state nano-emitters, of particular interest because of their unique bright on-demand single-photon generation [6,7], generation of polarization entanglement [8], two photon interference [9,10], spin-photon entanglement [11,12], and quantum teleportation [13].

[1] A manuscript based on the results presented in this chapter is under preparation.

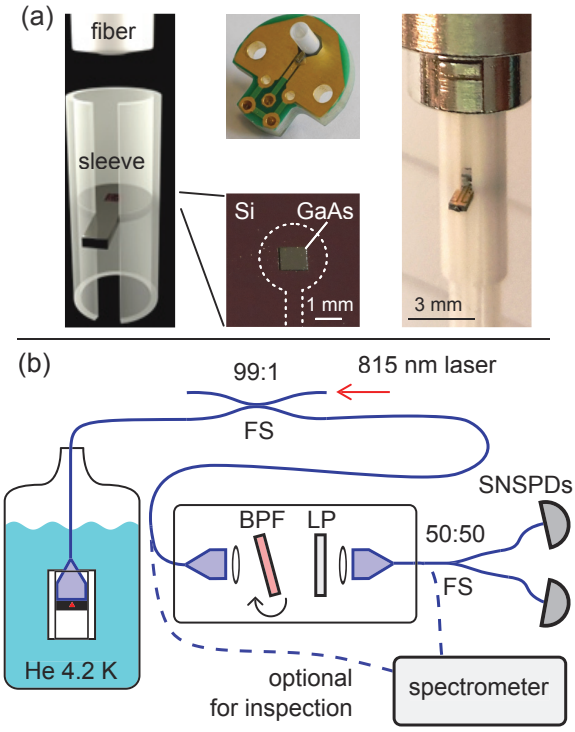

Figure 8.1 | (a) The QD samples are mounted on prefabricated silicon carriers etched in a key hole shape matching standard fiber sleeves. (b) The fiber based setup used to excite the QDs and collect the emitted photons. The sample is immersed in LHe and the excitation and collection is done through a 99:1 fiber beam splitter.

Until now the sources were mounted in bulky cryostats equipped with nanopositioning stages. Each cryostat could only be used to access a few emitters at a time. Precise and time consuming alignments was required for each cool-down. Although these processes have become standard, this approach was hardly scalable.

Prior works have addressed the coupling of quantum dots (QD) to fibers[14–16]. A robust and scalable platform for the coupling of many sources to single mode optical fibers is necessary. In addition, reproducible performances over many cool-down cycles are hard to achieve. This reproducibility is of prime concern when sources with matched physical properties, e.g. photon emission energy, are required. We report on a novel hybrid platform for fiber coupling of single-photon emitters. Our technique is robust, scalable and resource inexpensive, many fiber-coupled single-photon sources can be mounted in a single cryostat, reducing the cost and space needed for multi-photon experiments. Moreover, we integrate

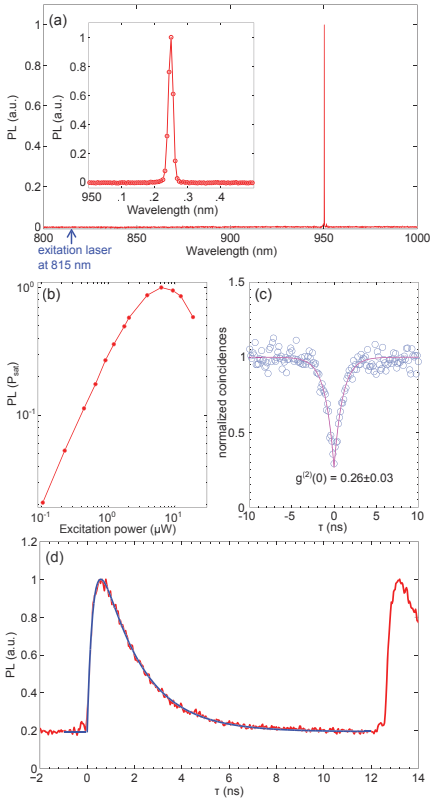

Figure 8.2 | (a) Photoluminescence from a fabricated device after passing through the fiber-based filter stage. No laser or other undesired emission can be observed. Inset shows a zoomed spectra of the filtered emission line. (b) Normalized power-dependent PL intensity for the studied emission line. (c) All in fiber photon-correlation measurement, demonstrating a clear antibunching with $g^2(0) = 0.26 \pm 0.03$ (d) Time correlated single photon counting measurement. The lifetime is ~ 1.7 ns. No reflection and re-excitation is visible in the spectra.

this approach in a fully fiber-based photon correlation measurement all the way from the source to the detectors.

8.2 Device, measurement and results

We mount 1 mm^2 pieces of QD samples, in this case InGaAs/GaAs QDs, on silicon pieces. The silicon carrier chips are etched in a keyhole shape[17] and serve as holder for QD chips which can be directly glued to these silicon pieces or be fixed in their prefabricated openings, shown in Figure 8.1(a). Mounting the samples in the silicon pockets makes it possible for further processing of the QD samples. This hybrid integration also suits well to the future deterministic positioning of fiber with respect to a selected QD. The sample is then inserted in a standard fiber mating sleeve and brought in contact with the fiber. A fiber ferule is then inserted and brought in contact with the sample from the back for mechanical stability. This sleeve assembly maintains the alignment of the QD sample to the core of the single mode fiber during operation and cool-down cycles.

To measure photon statistics, we use a fully fiber based network all the way from the source to the detector, shown in Fig 8.1(b). A fiber beam-splitter with splitting ratio 99:1 is used to both excite the QDs and route the generated single photons. We excite the QDs with a continuous laser tuned to 815 nm. To separate the emission line of interest from all other undesired signals such as laser and other nearby QDs, we use a fiber-coupled filter stage. This stage consists of a high-pass and a tunable bandpass filter. Here we use a bandpass filter with a 3 dB bandwidth of 1 nm. The transmission of the filter from fiber to fiber is better than 80%. Fig 8.2(a) shows an example of a photoluminescence (PL) measurement after transmission through the filter, only a single QD line exist over the operational range. Fig 8.2(b) shows the power dependence measurement for the same QD emission line.

Our filter is then connected to a fiber-based 50:50 beamsplitter and the outputs are terminated with two superconducting nanowire single-photon detectors. We perform photon correlation measurements, the result is shown in Fig 8.2(c). A multi-photon emission probability of $g^{(2)} = 0.26 \pm 0.03$ is measured. This value demonstrates that the emission is dominated by a single quantum emitter. Fig 8.2(d) represents a lifetime measurement with a repetition rate of 80 MHz.

To evaluate the stability of our devices, we measure the emission spectra of a fiber coupled QD over several cool-downs. Fig 8.3(a) represents the outcomes for five repetitive measurements, with the inset showing the intensities for each cool-down. The fluctuations in the signal intensity are $\sim 5\%$. To study the change in the emission spectrum over time, we performed two measurements separated by a week as shown in Fig 8.3(b). No noticeable difference was observed; demonstrating the robust performance of our device.

8.3 Discussion and conclusion

A practical platform for demanding quantum optics experiments requires high photon extraction, filtering and long-distance transmission efficiencies. For the devices shown in

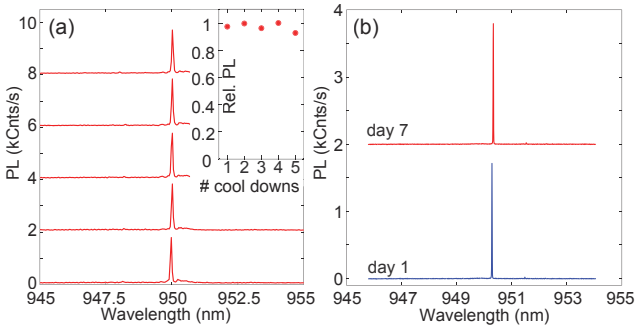

Figure 8.3 | (a) PL measurement on fiber coupled sample for five cool-downs cycles. The inset represents normalized QD emission intensity for each cool-down, demonstrating a stable performance with less than 10% fluctuations. (b) Two PL measurements separated by a week. The two spectra are nearly identical.

this work, all stages of the experiments are implemented in optical fibers and therefore it is possible to achieve higher filtering and guiding efficiencies. This is because the mode shape is not distorted by a grating. To estimate QD to fiber coupling efficiency, we performed finite-difference time-domain simulations, the results are shown in Fig 8.4(a-c). For a planar QD sample, emitting around 950 nm in contact with a regular single mode fiber, the maximum coupling efficiency is $\sim 1.2\,\%$. The influence of vertical and lateral displacement of the QD with respect to the fiber core is shown in Fig 8.4(a) and Fig 8.4(b), respectively. Fig 8.4(c) represents the electric field profile of a QD emission. Most of photons are reflected back toward the substrate at the semiconductor-air interface. To reduce the reflection, planar samples can be etched into the form of microposts [18] or needles [19]. Furthermore, the coupling efficiency can be improved by engineering the fiber end-facet [20].

Another important requirement for a scalable platform in quantum optics is the possibility to generate indistinguishable photons preferably from many sources. This requirement can be divided in two parts: sources capable of generating transform-limited photons and the possibility to tune different sources to degeneracy. As for the first prerequisite, optimizing the excitation techniques can lead to generation of indistinguishable photons [21]. Furthermore, the second requirement for our devices can be addressed by Stark [22,23] and/or strain [24,25] tuning techniques.

In conclusion, we have shown a plug and play scalable all fiber-based platform for integration of multiple single-photon sources in a single cryostat. Our approach is resource inexpensive, shows excellent robustness and stability and is compatible with various types of emitters. We demonstrate a proof of concept complete fiber-based $g^2(\tau)$ measurement. The main limitation in current devices were discussed and directions on how to improve them were suggested. The platform has minimum requirements and allows for mass production

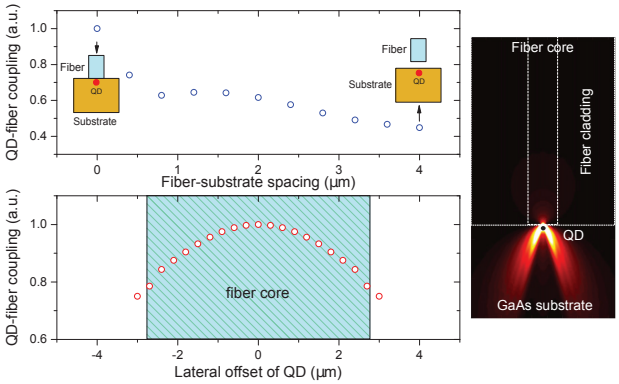

Figure 8.4 | (a) QD to fiber coupling efficiency as a function of the vertical spacing between the QD and the fiber. (b) Coupling efficiency as a function of lateral displacement of the QD with respect to the fiber core. (c) The electric field profile of the QD emission. Most of the light is reflected at the semiconductor-air interface.

of fiber-coupled quantum emitters.

Bibliography

[1] N. Gisin, G. Ribordy, W. Tittel, and H. Zbinden, "Quantum cryptography," *Rev. Mod. Phys.*, vol. 74, pp. 145–195, 2002.

[2] E. Knill, R. Laflamme, and G. J. Milburn, "A scheme for efficient quantum computation with linear optics," *Nature*, vol. 409, pp. 46–52, 2001.

[3] J. P. Dowling and K. P. Seshadreesan, "Quantum optical technologies for metrology, sensing, and imaging," *J. Lightwave Technology*, vol. 33, no. 12, pp. 2359–2370, 2015.

[4] M. Okano, H. H. Lim, R. Okamoto, N. Nishizawa, S. Kurimura, and S. Takeuchi, "0.54μm resolution two-photon interference with dispersion cancellation for quantum optical coherence tomography.," *Sci. Rep.*, vol. 5, p. 18042, 2015.

[5] L. A. Lugiato, A. Gatti, and E. Brambilla, "Quantum imaging," *Journal of Optics B: Quantum and Semiclassical Optics*, vol. 4, no. 3, p. S176, 2002.

[6] X. Ding, Y. He, Z.-C. Duan, N. Gregersen, M.-C. Chen, S. Unsleber, S. Maier, C. Schneider, M. Kamp, S. Höfling, C.-Y. Lu, and J.-W. Pan, "On-demand single photons with high extraction efficiency and near-unity indistinguishability from a resonantly driven quantum dot in a micropillar," *Phys. Rev. Lett.*, vol. 116, p. 020401, 2016.

[7] J.-H. Kim, T. Cai, C. J. K. Richardson, R. P. Leavitt, and E. Waks, "A bright on-demand source of indistinguishable single photons at telecom wavelengths," *ArXiv e-prints*, 2015.

[8] M. Müller, S. Bounouar, K. D. Jöns, M. Glässl, and P. Michler, "On-demand generation of indistinguishable polarization-entangled photon pairs," *Nat. Photon*, vol. 8, pp. 224–228, 2013.

[9] C. Santori, D. Fattal, J. Vuckovic, G. S. Solomon, and Y. Yamamoto, "Indistinguishable photons from a single-photon device," *Nature*, vol. 419, no. 6907, pp. 594–597, 2002.

[10] R. B. Patel, A. J. Bennett, I. Farrer, C. A. Nicoll, D. A. Ritchie, and A. J. Shields, "Two-photon interference of the emission from electrically tunable remote quantum dots," *Nat. Photon.*, vol. 4, pp. 632–635, Sep 2010.

[11] K. D. Greve, L. Yu, P. L. McMahon, J. S. Pelc, C. M. Natarajan, N. Y. Kim, E. Abe, S. Maier, C. Schneider, M. Kamp, S. Hofling, R. H. Hadfield, A. Forchel, M. M. Fejer, and Y. Yamamoto, "Quantum-dot spin-photon entanglement via frequency downconversion to telecom wavelength," *Nature*, vol. 491, no. 7424, pp. 421–425, 2012.

[12] W. B. Gao, P. Fallahi, E. Togan, J. Miguel-Sanchez, and A. Imamoglu, "Observation of entanglement between a quantum dot spin and a single photon," *Nature*, vol. 491, no. 7424, pp. 426–430, 2012.

[13] W. Pfaff, B. J. Hensen, H. Bernien, S. B. van Dam, M. S. Blok, T. H. Taminiau, M. J. Tiggelman, R. N. Schouten, M. Markham, D. J. Twitchen, and R. Hanson, "Unconditional quantum teleportation between distant solid-state quantum bits," *Science*, vol. 345, no. 6196, pp. 532–535, 2014.

[14] X. Xu, I. Toft, R. T. Phillips, J. Mar, K. Hammura, and D. A. Williams, ""plug and play" single-photon sources," *Appl. Phys. Lett.*, vol. 90, no. 6, 2007.

[15] H. Kumano, T. Harada, I. Suemune, H. Nakajima, T. Kuroda, T. Mano, K. Sakoda, S. Odashima, and H. Sasakura, "Stable and efficient collection of single photons emitted from a semiconductor quantum dot into a single-mode optical fiber," *Applied Physics Express*, vol. 9, no. 3, p. 032801, 2016.

[16] D. Cadeddu, J. Teissier, F. R. Braakman, N. Gregersen, P. Stepanov, J.-M. Gérard, J. Claudon, R. J. Warburton, M. Poggio, and M. Munsch, "A fiber-coupled quantum-dot on a photonic tip," *Applied Physics Letters*, vol. 108, no. 1, 2016.

[17] S. Dorenbos, R. Heeres, E. Driessen, and V. Zwiller, "Efficient and robust fiber coupling of superconducting single photon detectors," *arXiv:1109.5809*, 2011.

[18] M. Pelton, C. Santori, J. Vuckovic, B. Zhang, G. S. Solomon, J. Plant, and Y. Yamamoto, "Efficient source of single photons: A single quantum dot in a micropost microcavity," *Phys. Rev. Lett.*, vol. 89, p. 233602, Nov 2002.

[19] J. Claudon, J. Bleuse, N. S. Malik, M. Bazin, P. Jaffrennou, N. Gregersen, C. Sauvan, P. Lalanne, and J.-M. Gerard, "A highly efficient single-photon source based on a quantum dot in a photonic nanowire," *Nat. Photon.*, vol. 4, no. 3, pp. 174–177, 2010.

[20] S. Kato, S. Chonan, and T. Aoki, "High-numerical-aperture microlensed tip on an air-clad optical fiber," *Opt. Lett.*, vol. 39, no. 4, pp. 773–776, 2014.

[21] A. V. Kuhlmann, J. H. Prechtel, J. Houel, A. Ludwig, D. Reuter, A. D. Wieck, and R. J. Warburton, "Transform-limited single photons from a single quantum dot," *Nat. Commun.*, vol. 6, 2015.

[22] B. D. Gerardot, S. Seidl, P. A. Dalgarno, R. J. Warburton, D. Granados, J. M. Garcia, K. Kowalik, O. Krebs, K. Karrai, A. Badolato, and P. M. Petroff, "Manipulating exciton fine structure in quantum dots with a lateral electric field," *Appl. Phys. Lett.*, vol. 90, p. 041101, 2007.

[23] A. J. Bennett, M. A. Pooley, R. M. Stevenson, R. B. P. M. B. Ward, A. B. de la Giroday, N. Sköld, I. Farrer, C. A. Nicoll, D. A. Ritchie, and A. J. Shields, "Electric-field-induced coherent coupling of the exciton states in a single quantum dot," *Nat. Phys*, vol. 6, pp. 947–950, 2010.

[24] A. Rastelli, F. Ding, J. D. Plumhof, S. Kumar, R. Trotta, C. Deneke, A. Malachias, P. Atkinson, E. Zallo, T. Zander, and et al., "Controlling quantum dot emission by integration of semiconductor nanomembranes onto piezoelectric actuators," *Phys. Status Solidi B*, vol. 249, no. 4, pp. 687–696, 2012.

[25] R. Trotta, J. Martin-Sanchez, J. S. Wildmann, G. Piredda, M. Reindl, C. Schimpf, E. Zallo, S. Stroj, J. Edlinger, and A. Rastelli, "Wavelength-tunable sources of entangled photons interfaced with atomic vapours," *Nat. Commun.*, vol. 7, 2016.

Chapter 9

Conclusion And Future Work

Semiconductors revolutionized our life in the mid twenty century and they continue to serve as the forefront of innovations to date. Quantum mechanics played a pivotal role in understanding, designing, and developing semiconductor technologies. Lasers and MRI imaging are two other examples of systems that work based on quantum mechanical phenomena. In recent decades a new stream of quantum technologies has emerged which directly create, manipulate and measure the quantum states. Quantum information processing, quantum communication, and quantum sensing belong to this new wave of applications.

Developing a practical foundation for novel quantum technologies has been one of the main areas of focus for scientists in recent decades. Quantum optics is one of the promising infrastructures for these technologies. In previous chapters we discussed techniques to address scalable implementation of quantum optics.

In this chapter we conclude with a summary of the current status of our integrated platform and then provide an outlook for future directions towards scalable implementation of quantum optics experiments.

9.1 Conclusions and summary

In this thesis, we studied two methodologies for scalable quantum optics: on-chip integrated and modular fiber-based approach. We demonstrated proof of principle prototypes of both techniques. In addition, we provided our first results on improved p-n junction nanowires for future electrically pumped on-chip sources and SiN waveguides as a potential technology for realization of on-chip quantum optics circuits. In the following sections, we provide a brief overview of emerging experiments based on our on-chip technology and conclude with future milestones for improving and scaling up our platforms.

9.2 Current status

As discussed in Chapter 6 PECVD deposited SiN waveguides can be used for realization of tunable filters based on ring resonators in cryogenic temperatures. Furthermore, we showed in Chapter 7, single-photon emitters based on QDs embedded in nanowires can be incorporated into SiN waveguides without any significant degradation.

A natural step after integration of the nanowire QDs in waveguides is the demonstration of on-chip tuning and filtering. Fig. 9.1(a) presents a nanowire embedded in an optical waveguide with its forward direction (the direction of the nanowire tip) connected to a ring resonator with integrated heater for tuning. The off-resonance (not in resonance with ring) emission spectra of the nanowire QD collected from the end-facet of the forward and backward waveguides are shown in Fig. 9.1(b). The intensity of forward emission is $\sim$25% higher than the backward emission. As discussed in Chapter 7, similar coupling efficiencies for forward and backward directions are expected. We ascribe the difference in the intensities of the two spectra to the deviation of nanowire shape specially its taper length comparing to the simulated geometry in Chapter 7.

The TE and TM resonances of the ring resonator are shown in Fig. 9.1(c). The free spectral range for both resonance modes is $\sim$ 1 nm. The resonant modes of the ring and QD emission energy can both be modified by temperature. When in resonance, selected emission line of the QD is transferred into the drop port of the ring resonator.

We excite the QD using a continuous wave laser at 532 nm and collect the photons from the drop port of the ring. Fig. 9.1(d) represents the collected signal when ring and our selected emission line are in resonance. The only observable line over the whole collected spectrum is that of the selected emission line.

Tuning of the sources

We showed in Chapter6 that SiN has low thermooptic coefficient at cryogenic temperatures. Hence, the QD tunes more efficiently even though it is further away from the heater. Fig. 9.2(a)

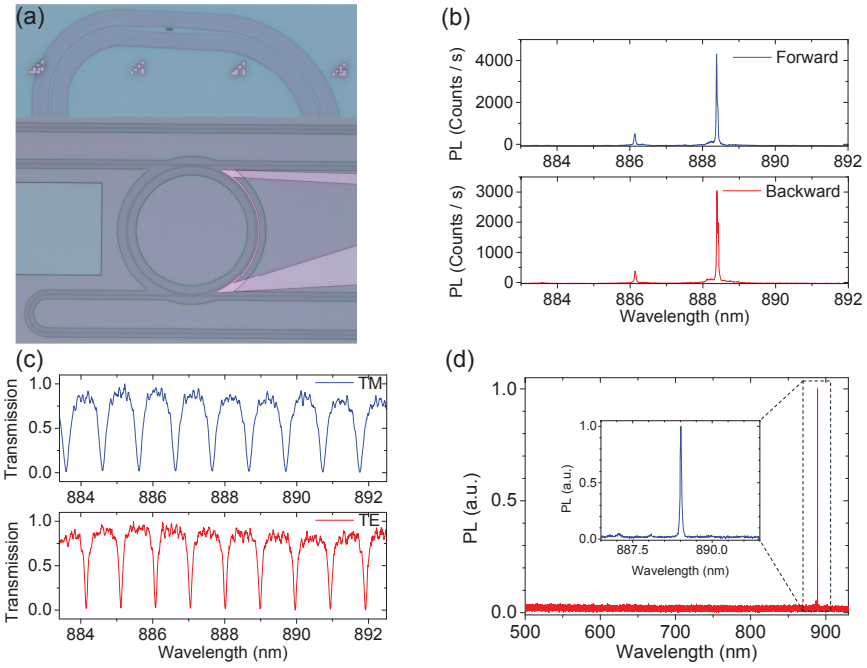

Figure 9.1 | A single-photon source integrated with photonic waveguides and a ring resonator. (a) Microscope images of the fabricated device. A nanowire QD is embedded in a waveguide with the forward side connected to a tunable ring resonator. For comparison, the backward emission is directly out-coupled. (b) Off-resonance spectra for forward and backward QD emissions. (c) TE and TM resonance modes of the tunable ring resonator. (d) A Photoluminescence spectrum collected from the drop port of the ring resonator. The only visible line is the selected emission line from QD which is in resonance with the ring.

shows how the emission from a nanowire QD is tunned by a distant heater. Applying 10 V (corresponding to $\sim 35\,mW$) to the heater brings the QD into resonance with its connected ring resonator.

Although the emissions from QD tune efficiently with the heat, but the properties of the photons are also affected with the temperature. We perform photon-correlation measurements for the applied voltages of 0 (on the through port of the ring) and 10 V (on the drop port of the ring) shown in Fig. 9.2(b) and Fig. 9.2(c), respectively. The value of $g^2(0)$ varies from 0.21 ± 0.08 at 0 V to 0.55 ± 0.08 for 10 V.

We also show for the first time, single-photon multiplexing and demultiplexing. Fig. 9.3(a) presents a microscope picture of our device which multiplexes two photonic channels each containing an embedded nanowire QD. The multiplexed photons are brought in resonance

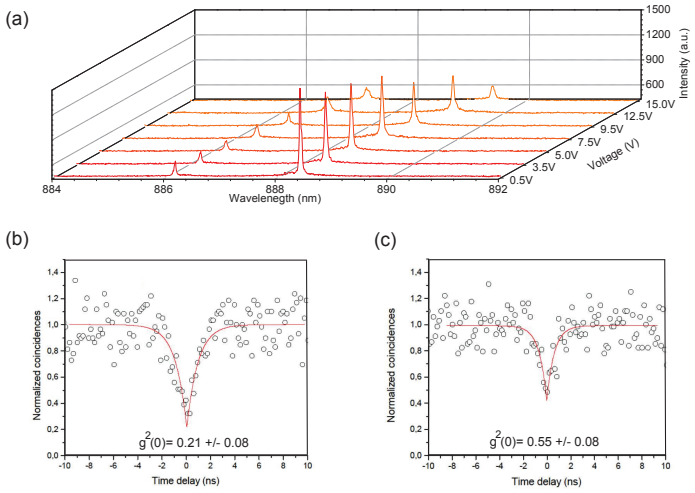

Figure 9.2 | Temperature tuning of a QD nanowire. (a) Collected spectra of a nanowire QD as a function of applied voltage to an integrated heater. (b) and (c), Photon-correlation measurements for applied voltages of 0 V and 10 V to the heater, respectively. The single-photon purity is degraded by heat.

with a connected ring resonator using a global distant heater. Fig. 9.3(b) demonstrates the spectra of multiplexed nanowire QDs as a function of applied heater voltage. Four prominent emission lines can be observed, one around 881.2 nm from the first QD and 3 close lines around 887 nm emitted by second nanowire QD. We tune the desired line to the resonance of the ring resonator as observed for an applied voltage of 27 V, also indicated by a red circle, and hence demultiplex the photons emitted by two separate QDs. It should be noted, that here as the heater is severals millimeters away from the source, higher tuning voltages are required, however, as the wavelength shift indicates, corresponding effective temperature change is much lower comparing to the presented measurements in Fig. 9.2.

9.2.1 Integration of single-photon sources, photonic circuits, and single-photon detectors

To perform fully on-chip quantum optics experiments, single-photon detectors must also be integrated with sources and photonic circuits. The results of our first attempt to integrate sources with the detectors is presented in Fig.9.4. An InP p-n junction nanowire with an InAsP section is placed and contacted on top of a superconducting nanowire single-photon detector with a dielectric separation layer. The schematic along with an SEM picture of a fabricated device are shown in Fig.9.4(a) and Fig.9.4(b), respectively. By biasing the nanowire

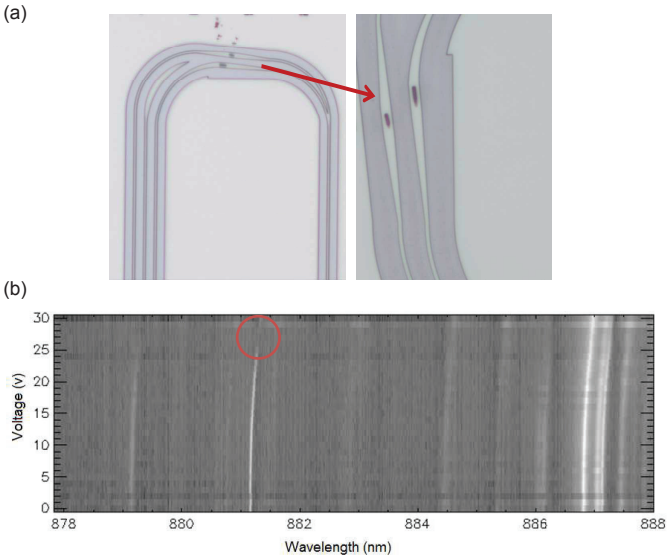

Figure 9.3 | Single-photon multiplexing and demultiplexing. (a) Two nanowire QDs are encapsulated in two separate photonic channels which are then merged together and hence, multiplex the emitted photons from the embedded QDs. The common waveguide is then fed into a ring resonator filter (b) The spectrum of multiplexed photons collected from the through port of the ring. For an applied voltage 27 V, the first QD emission indicated by red circle, is removed from the common waveguide.

detection events can be registered on the superconducting detectors as shown in Fig.9.4(c).

To separate single-photons from other undesired emissions, on chip filters are required. We fabricated a prototype device, Fig.9.5, which is designed to perform on-chip photon-correlation measurement. The photons from a QD are collected into a photonic channel and are filtered using a tunable ring resonator. The selected photons are then split in a Y-splitter and terminated in two superconducting single-photon detectors. To avoid heat transfer into the source and superconducting detectors, we mount the sample in a bath cryostat. Our preliminary characterizations indicates that by increasing the cooling power, the detectors can operate normally when applying voltages to the integrated heater for tune the filter.

9.3 Outlook and future work

We reviewed the current status of our approach towards fully integrated quantum optics and in chapter 8, we presented our initial results with modular fiber-based implementation.

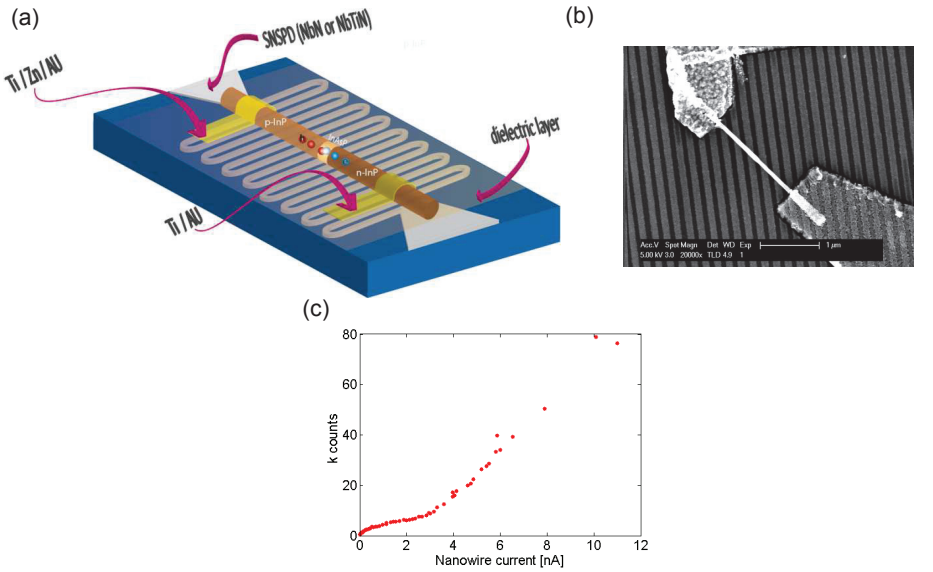

Figure 9.4 | A single-photon LED integrated with superconducting single-photon detector. (a) Schematic of the fabricated device. A p-n junction nanowire is placed on top a superconducting single-photon detector separated by a thing dielectric layer. The p and n sides of the nanowire are contacted in two separate e-beam and evaporation steps. (b) An SEM image of the device. (c) Detection events registered by detector as a function of applied current to the nanowire.

In this section, we discuss some future directions for scaling the proposed methods.

9.3.1 Monolithically integrated quantum optics

Thus far we have presented prototypes for integrated quantum optics. Several additional important challenges must be overcome for a scalable fully on-chip platform. In the following, we briefly study these milestones.

An optimal platform for integrated photonic circuit

An important step in realizing optical circuits for integrated quantum optics is finding a material with low optical losses, reliable fabrication (preferably CMOS compatible), and high electro-optic and nonlinearity coefficients for tuning and realizing photon-photon interactions. SiN has the first two requirements but it does not offer large electro-optic coefficient or nonlinearities.

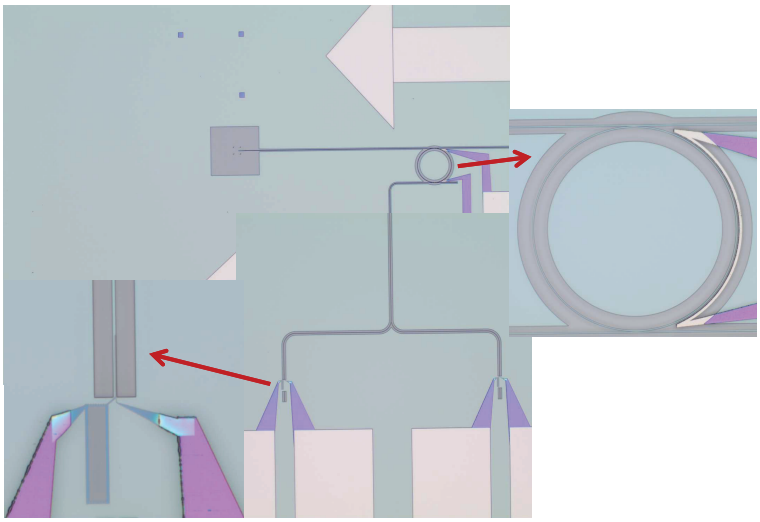

Figure 9.5 | A prototype chip for integrated single-photon correlation measurement. A nanowire QD is coupled to a waveguide which is connected to a tunable ring resonator. The filtered photons are then split in two separate waveguides each coupled evanescently to a detector. The measurement is performed in a bath cryostat where the cooling power is high enough to guarantee proper performance of the emitter and superconducting detectors.

An alternative material to SiN is aluminum nitride (AlN). AlN has low losses over a large window[1] and it is a promising material for nonlinear applications[2,3]. Another option is growing single-photon sources that emit around the telecommunication wavelengths, where established silicon photonics can be exploited.

On-chip control of emission energy, spin and charge states

For many ambitious applications, the quantum state of light has to be directly manipulated. This requirement puts stringent prerequisites on energy and polarization of the single-photons as well as their relation with each other. To deterministically prepare a state, the emission energy and charges in QDs must be carefully controlled. This can be achieved with on-chip electrical[4,5] and strain fields[6]. Controlling the spin of the carriers in quantum dots[7] is another important challenge that should be addressed.

Generation of Fourier-transform limited photons on-chip

Multi-photon states rely on the possibility of producing indistinguishable photons. Indistinguishably of generated photons is often linked to their deviation from Fourier-transform limit. In Chapter7 we demonstrated a source which was a factor of ∼7 from the transform limit. Resonant excitation[8] and cooling of the sample to milli-kelvin temperatures[9] are proven ways to improve the linewidth.

9.3.2 Fiber based multi-photon experiments

In Chapter8 we introduced our new method of fiber-based quantum optics. A proof of principle single-photon experiment measurement was also performed. To scale up this method many fiber-coupled sources with indistinguishable photons are necessary. Similar approach as the discussed techniques can be used for generation of transform limited photons. As for the energy tuning, our QD chips can be glued or gold bonded to piezo chips[10] prior to mounting them in the fiber sleeves. Furthermore, electrical contacts for Stark tuning can be defined on QD chips.

As a first step, a two-photon interference experiment could be performed on two fiber-coupled tunable QDs. For the next stages, to scale this into a multi-photon experiment, high photon extraction efficiencies are needed. Mode matching of the QD emission profile and the mode of a single fiber by on-chip beam shaping or miniature lens assembly (inside fiber sleeve) can be exploited.

Bibliography

[1] C. Xiong, W. H. P. Pernice, and H. X. Tang, "Low-loss, silicon integrated, aluminum nitride photonic circuits and their use for electro-optic signal processing," *Nano Letters*, vol. 12, no. 7, pp. 3562–3568, 2012.

[2] C. Xiong, W. H. P. Pernice, X. Sun, C. Schuck, K. Y. Fong, and H. X. Tang, "Aluminum nitride as a new material for chip-scale optomechanics and nonlinear optics," *New Journal of Physics*, vol. 14, no. 9, p. 095014, 2012.

[3] W. H. P. Pernice, C. Xiong, C. Schuck, and H. X. Tang, "Second harmonic generation in phase matched aluminum nitride waveguides and micro-ring resonators," *Applied Physics Letters*, vol. 100, no. 22, 2012.

[4] M. P. van Kouwen, M. E. Reimer, A. W. Hidma, M. H. M. van Weert, R. E. Algra, E. P. A. M. Bakkers, L. P. Kouwenhoven, and V. Zwiller, "Single electron charging in optically active nanowire quantum dots," *Nano Letters*, vol. 10, no. 5, pp. 1817–1822, 2010.

[5] M. E. Reimer, M. P. van Kouwen, A. W. Hidma, M. H. M. van Weert, E. P. A. M. Bakkers, L. P. Kouwenhoven, and V. Zwiller, "Electric field induced removal of the biexciton binding energy in a single quantum dot," *Nano Letters*, vol. 11, no. 2, pp. 645–650, 2011.

[6] R. Trotta, J. Martin-Sanchez, J. S. Wildmann, G. Piredda, M. Reindl, C. Schimpf, E. Zallo, S. Stroj, J. Edlinger, and A. Rastelli, "Wavelength-tunable sources of entangled photons interfaced with atomic vapours," *Nature Communications*, vol. 7, 2016.

[7] D. Press, T. D. Ladd, B. Zhang, and Y. Yamamoto, "Complete quantum control of a single quantum dot spin using ultrafast optical pulses," *Nature*, vol. 456, pp. 218–221, Nov 2008.

[8] A. V. Kuhlmann, J. H. Prechtel, J. Houel, A. Ludwig, D. Reuter, A. D. Wieck, and R. J. Warburton, "Transform-limited single photons from a single quantum dot," *Nat. Commun.*, vol. 6, 2015.

[9] M. E. Reimer, G. Bulgarini, R. Heeres, B. J. Witek, M. A. M. Versteegh, D. Dalacu, J. Lapointe, P. J. Poole, and V. Zwiller, "Overcoming power broadening of the quantum dot emission in a pure wurtzite nanowire," *ArXiv e-prints*, vol. 1407.2833, 2014.

[10] A. Rastelli, F. Ding, J. D. Plumhof, S. Kumar, R. Trotta, C. Deneke, A. Malachias, P. Atkinson, E. Zallo, T. Zander, and et al., "Controlling quantum dot emission by integration of semiconductor nanomembranes onto piezoelectric actuators," *Phys. Status Solidi B*, vol. 249, no. 4, pp. 687–696, 2012.

Summary

In the past decades quantum optics has been at the forefront of quantum innovative technologies. For practical applications, scalable platforms for implementation of quantum optical circuits are vital. This thesis presents two new platforms for scalable implementation of quantum optical circuits, namely, modular approach and monolithic integration. Here, we take the first steps towards the integration of three main elements of every quantum optics circuits: Single-photon emitters, single-photon detectors, and quantum logics.

Until now, most quantum optical circuits used separate platforms for single-photon generation and detection. The main challenge in the integration of these technologies, which have different requirements, has slowed down the research in the field. Here, we integrate sources and detectors by first fabricating the devices on their own platform and then transferring and combining them together. Plasma enhanced chemical vapor deposition of silicon nitride followed by etching optical waveguides connect these elements.

Removing the Poissonian optical excitation field from the quantum circuit is necessary for integration. Classical optical excitation can be avoided if the sources are electrically pumped. However, fabrication of high-quality electrically pumped sources, suitable for integration, has been limited. The experiments described in **chapter 4** are our first step towards addressing the mentioned problem. Defect-free nanowires are grown on <100> direction and their optoelectronic performance are characterized.

Nanowire quantum dots, thanks to their waveguiding, purity, coherence and their potentials for deterministic integration with other optical circuits, are promising single-photon sources for on-chip quantum optics. However, precise control of the emission energy of the quantum dots by growth has not become possible yet. **Chapter 5** describes a method for on-chip tuning of emission energy of nanowire quantum dots using strain fields. We show the emission energy of independent nanowire quantum dots can be brought into degeneracy without affecting their single-photon emission properties.

The quantum optical components have to be routed and connected together to form functional circuits. On a chip, this is usually carried out using optical waveguides. Moreover, manipulation of single photons has to be done in a scalable fashion. Again optical waveguides and ring resonators are very good candidates for this task. Therefore, understanding the behavior of these circuits such as their losses, polarization dependence, and temperature behavior is important. The experiment described in **chapter 6** studies the behavior of plasma enhanced silicon nitride waveguides in cryogenic temperatures. We concluded in this chapter that due to weak thermo-optic sensitivity of silicon nitride at cryogenic temperatures, the available thermal budget on the system should be carefully considered.

An important step in achieving a scalable platform for quantum optical circuits is deterministic and efficient integration of single-photon sources. In **chapter 7**, we demonstrate successful integration of III-V nanowire quantum dots with silicon nitride waveguides. The nanowires are deterministically selected and transferred from the original growth chip

to the new substrate where they are integrated with low-loss silicon nitride waveguides. Our measurements show that the integrated sources preserve their high quality emission properties.

In **chapter 8**, we describe an alternative approach: a modular method for scalable quantum optics. The proposed technique is based on coupling the single-photon from sources into optical fibers where the photons can be processed and then fed into the single-photon detectors. This approach has high flexibility and is easier to implement but as described in the chapter, at the moment, losses in the interfaces between optical fibers and single-photon sources are a major limiting factor.

We conclude the thesis with some possible future directions and exciting new results on integration of single-photon detectors with sources and waveguides. Finally, primary results on on-chip single-photon filtering and removal of the optical excitation field are demonstrated.

Samenvatting

Gedurende de afgelopen decennia heeft de kwantum-optica aan de voorhoede van innovatieve kwantumtechnologieën gestaan. Voor praktische toepassingen is het cruciaal dat de kwantum-optische circuits gebaseerd zijn op schaalbare platforms. Dit proefschrift presenteert twee nieuwe platvormen voor schaalbare implementatie van kwantum-optische circuits, namelijk; een modulaire benadering en monolithische integratie. Hier zetten we de eerste stappen naar integratie van de drie belangrijkste elementen van elk kwantum-optisch circuit: Enkele-foton bronnen, enkele-foton detectoren en kwantumlogica.

Tot nu toe gebruikten de meeste kwantum-optische circuits aparte platvormen voor enkele–foton generatie en detectie. Dit vormt de grootste uitdaging bij het integreren van deze technologieën, waarbij elk zijn eigen specifieke eisen heeft, en heeft een rem gezet op de snelheid van het onderzoek. Hier fabriceren we de bronnen en detectoren op hun eigen platform en verplaatsen en combineren we ze vervolgens. Plasma enhanced chemical vapour deposition van siliciumnitride gevolgd door het etsen van optische golfgeleiders verbindt de verschillende elementen.

Om het kwantumcircuit te kunnen integreren is het nodig het Poisson optische excitatieveld te verwijderen. Klassieke optische excitatie kan voorkomen worden als de bronnen elektrisch gepompt worden. Echter de fabricage van hoge-kwaliteit elektrisch gepompte bronnen, geschikt voor integratie, is beperkt geweest. De experimenten beschreven in **hoofdstuk 4** zijn onze eerste stap om het genoemde probleem te addresseren. Defectvrije nanodraden gegroeid in <100> richting en hun optoelektronische prestaties zijn gekarakteriseerd.

Nanodraad kwantumdots, zijn dankzij hun golfgeleidende eigenschap, spectrale puurheid, coherentie en mogelijkheid tot deterministische integratie met andere optische circuits veelbelovende enkele-foton bronnen voor on-chip kwantum-optica. Echter, het is tot op heden nog niet mogelijk om de emissie energie van kwantumdots tijdens de groei te controleren. **Hoofdstuk 5** beschrijft een methode voor het on-chip regelen van de emissie energie van kwantumdots door middel van spanningsvelden. We laten zien dat de emissie energie van onafhankelijke nanodraad kwantumdots degeneratief gemaakt kan worden zonder dat de enkele-foton emissie eigenschap wordt aangetast.

De kwantum-optische componenten moeten gerouteerd en verbonden worden om functionele circuits te vormen. Het is gebruikelijk om dit op een chip met optische golfgeleiders te doen. Bovendien moet de manipulatie van de enkele fotonen gedaan worden op een schaalbare manier. Ook voor deze taak zijn optische golfgeleiders en ring resonatoren goede kandidaten. Daarom is het van belang te weten hoe de verliezen, polarisatieafhankelijkheden en temperatuurafhankelijkheden van deze circuits is zijn. Het experiment beschreven in **hoofdstuk 6** bestudeert het gedrag van plasma enhanced siliciumnitride golfgeleiders bij cryogene temperaturen. We concluderen in het hoofstuk dat er goed naar het thermische budget gekeken moet worden vanwege de zwakke thermisch-optische sensitiviteit van

siliciumnitride bij cryogene temperaturen.

Een belangrijke stap op weg naar het bereiken van een schaalbaar platform voor kwantum-optische circuits is deterministische en efficiënte integratie van enkele-foton bronnen. In **hoofdstuk 7** demonstreren we sucesvolle integratie van III-V nanodraad kwantumdots met siliciumnitride golfgeleiders. De nanodraden zijn deterministisch geselecteerd en overgeplaatst van de groei chip naar het nieuwe substraat, waar ze geïntregreerd zijn met siliciumnitride golfgeleiders met lage verliezen. Onze metingen laten zien dat de integratie de hoge kwaliteit emissie eigenschap niet aantast.

In **hoofdstuk 8** beschrijven we een alternatieve aanpak: een modulaire methode voor het realiseren van schaalbare kwantum-optica. De techniek is gebaseerd op het koppelen van de enkele-foton bronnen in optische glasvezels, waar de fotonen gemanipuleerd kunnen worden en naar enkele-foton detectoren geleid kunnen worden. Deze aanpak heeft het voordeel dat hij zeer flexibel en makkelijk is te implementeren maar, zoals beschreven in het hoofdstuk, vormen de verliezen bij de koppelingen een beperkende factor.

We concluderen het proefschrift met een vooruitblik voor toekomstige mogelijkheden en veelbelovende nieuwe resultaten waarbij enkele-foton detectoren geïntegreerd zijn met bronnen en golfgeleiders. Ten slotte worden de eerste resultaten van on-chip foton filteren en het verwijderen van het optische excitatie veld gedemonstreerd.

Acknowledgements

The Story of my stay in the Netherlands, all started with a google search about quantum information processing and emailing the first three groups which popped up, it didn't take a long time to get a reply. After the next following 11 emails from Val in just 2.5 days, I was sure I am going to join his group in QT. Val, thank you for giving me this possibility and also for your support all these years. I would also like to thank Prof. kouwenhoven for giving me the opportunity to work in QT and Prof. van der Zant for promoting my thesis.

Despite the fact that I already had a master's degree and I could have directly started a PhD, fortunately, I first started as an exchange master student to do my thesis for a second master's program. This was a unique chance for me because I got the most awesome supervisor! Working with Sander was/is great. Sander, nothing has changed, five years in and still I'm happily working for you.

Meeting Niels was another great thing that happened to me during my PhD years. Niels, sorry that I couldn't keep my promises and make a quantum computer in the period of your master thesis! It has been amazing to work with you every day and go for dinner together almost every evening.

I feel so lucky to have experienced QT/QuTech atmosphere for five years. So many great friends, so many nice events and parties. QT/QuTech has been always great scientifically but it never stopped there, it has been like a happy family. It's difficult to remember all names as there were many of good friends around, I have had many great moments in QT and for that I would like to thank you all.

Our group changed a lot since I joined it in 2011 but all the time, the group was full of amazing people. Among them, I would like to express my special thanks to (in a chronological order): Michael (or better said Prof. Reimer), thank you for always supporting me, I was in doubt in many moments but you always gave me optimism, working with you was a really great experience. Gabriele, everything is easier when you are around, I'm happy we are again colleagues in SQ. Maaike, it's hard not to like you immediately, I am very happy to be your friend, we meet less often now, but I'm happy whenever there is a opportunity. Klaus, it was a great chance for me to work with you and learn how to do things the German way (I'm sure you're telling to yourself, well you didn't learn it anyway!), in the last years of my PhD, we always planned the projects together and I'm happy that finally things worked out!. Ali, the true turning point of my PhD was when you joined the group, I don't know what I would have done with my PhD without you! We did great projects together and I'm sure we will continue to rock. Andreas, it's so refreshing to talk to you, both scientifically and about everyday life. Your great visions of fundamental facts in physics together with your practical solutions, makes you a great scientist but I also want to specially thank you for the positive atmosphere around you. Lucas, Katha and Julien, best of luck and success on your PhDs, I hope we can meet more often. Finally, I want to thank Martin, Reinier, Basia, Maria and Nika, it was great to work with you guys.

I feel lucky to be part of SQ family now. Sergiy, Jessie, Victor, Ronan, and Sander, Niels and Gabriele again, it's great to be with you guys.

I spent lot of my time in QT but life outside of QT was also amazing thanks to my great friends Farrokh, Nader and Mohammad: Nader and Mohammad, we shared many joyful moments and I wish this continues for many more years to come. Nader, if not every weekend we spend the next weekend together, BTW what are your plans for next weekend?. Farrokh, I could always count on you for everything which came along. It has been amazing friendship and I am looking forward for more to come.

Anna, meeting you was a great thing which happened to me. We have had unique moments and exciting years are still ahead of us and I cannot wait for them!

At last I would like to dedicate a very special thanks to my parents and my brother for all the love and support that they gave me. My amazing journey in life became possible only thanks to your unconditional support.

This thesis is part of the research programme of the Foundation for Fundamental Research on Matter (FOM), which is part of the Netherlands Organisation for Scientific Research (NWO).

Curriculum vitae

Iman Esmaeil Zadeh

18-09-1983 Born in Neyshaboor, Iran.

1998-2001 Beheshti High school, Neyshaboor, Iran.

2002-2007 BSc. Electrical Engineering, Sadjad University of Technology, Mashhad, Iran.
Thesis project: "A controlled system based on speech recognition."

2008-2011 MSc. Electrical Engineering, Linköping University, Linköping, Sweden.
Thesis title: “A study and implementation of on-chip EMC techniques”.

2009-present MSc. Applied Physics, Linköping University, Linköping, Sweden.

Feb.-Aug. 2011 Exchange student, Thesis project in Delft University of Technology
Thesis title: “Multi-pixel superconducting single-photon detectors: towards imaging sensors”.

2011-2016 Ph.D researcher, Delft University of Technology.
Subject: Integrated quantum optics, from modular to monolithic integration.
PhD advisor: Prof. V. Zwiller

List of publications

1- “A near ideal single photon detector”, Iman Esmaeil Zadeh, Johannes W.N . Los, Sergiy M. Dobrovolsk, Violette Steinmetz, Val Zwiller, Sander. N. Dorenbos, in preparation.

2- “Scalable and robust coupling of a single-photon emitter to an optical fiber”, Iman Esmaeil Zadeh, Andreas Fognini, Klaus D. Jöns, Katharina Zeuner, Ali W. Elshaari, Lucas Schweickert and Val Zwiller, in preparation.

3- “Quantum wavelength division multiplexing”, Ali W. Elshaari*, Iman Esmaeil Zadeh*, Andreas Fognini, Michael E. Reimer, Dan Dalacu, Philip J. Poole, Val Zwiller, and Klaus D. Jöns, Submitted. * equal contribution.

4- “On-Chip position controlled and electrically pumped photon sources integrated with superconducting nanowire single-photon detectors”, Johannes W.N. Los, Iman Esmaeil Zadeh, Michael M. Reimer, Sander N. Dorenbos, Val Zwiller, in preparation.

5- “Deterministic Integration of Single Photon Sources in Silicon Based Photonic Circuits”, Iman Esmaeil Zadeh*, Ali W. Elshaari*, Klaus D. Jöns, Andreas Fognini, Dan Dalacu, Philip J. Poole, Michael E. Reimer, and Val Zwiller, Nano Letters 2016 16 (4), 2289-2294 DOI: 10.1021/acs.nanolett.5b04709. * equal contribution.

6- “ High-Yield Growth and Characterization of <100> InP p–n Diode Nanowires”, Alessandro Cavalli, Jia Wang, Iman Esmaeil Zadeh, Michael E. Reimer, Marcel A. Verheijen, Martin Soini, Sebastien R. Plissard, Val Zwiller, Jos E. M. Haverkort, and Erik P. A. M. Bakkers. Nano Letters 2016 16 (5), 3071-3077.

7- “Controlling the exciton energy of a nanowire quantum dot by strain fields”, Yan. Chen, Iman Esmaeil Zadeh, Klaus D. Jöns, Andreas Fognini, Michael E. Reimer, Jiaxiang. Zhang , Dan Dalacu, Philip J. Poole, Fei Ding, Val Zwiller, Oliver G. Schmidt, Applied Physics Letters, 108, 182103 (2016), DOI:http://dx.doi.org/10.1063/1.4948762.

8- "Thermo-Optic Characterization of Silicon Nitride Resonators for Cryogenic Photonic Circuits", Ali W. Elshaari, Iman Esmaeil Zadeh, Klaus D. Jöns and Val Zwiller, in IEEE Photonics Journal, vol. 8, no. 3, pp. 1-9, June 2016.

9- “Measuring the quantum nature of light with a single source and a single detector”, Gesine A. Steudle, Stefan Schietinger, David Höckel, Sander N. Dorenbos, Iman Esmaeil Zadeh, Val Zwiller, and Oliver Benson, Phys. Rev. A 86, 053814.

Patent:

“Method and substrate carrier for coupling a photon or light source to an optical fiber”, Gabriele Bulgarini, Iman Esmaeil Zadeh and Val Zwiller, PCT/NL2016/050354.